Hydrogen generation using novel hydrocarbon anion, cation, and bipolar membrane materials

by
Amelia Hohenadel Hinshaw

B.Sc. (Chemistry), University of Pittsburgh, 2013
B.A. (History of Art and Architecture), University of Pittsburgh, 2013

Thesis Submitted in Partial Fulfillment of the
Requirements for the Degree of
Doctor of Philosophy

in the
Department of Chemistry
Faculty of Science

SIMON FRASER UNIVERSITY
Spring 2023

Declaration of Committee

Name:	**Amelia Hinshaw**
Degree:	**Doctor of Philosophy (Chemistry)**
Title:	**Hydrogen generation using novel hydrocarbon anion, cation, and bipolar membrane materials**
Committee:	**Chair:** **Neil Branda** Professor, Chemistry
	Steven Holdcroft Supervisor Professor, Chemistry
	George R. Agnes Committee Member Professor, Chemistry
	Corina Andreoiu Committee Member Professor, Chemistry
	Sami Khan Examiner Assistant Professor, Sustainable Energy Engineering
	Shannon Boettcher External Examiner Professor, Chemistry and Biochemistry University of Oregon

Abstract

The development of chemically stable and mechanically robust hydrocarbon ion exchange membranes is critical for the advancement of water electrolyzers. The acidic perfluorinated cation exchange membranes currently in use are expensive to manufacture, and pose significant environmental issues. Anion exchange membranes, which operate under basic conditions, are typically non-fluorinated, but lack stability in base and do not offer high ionic conductivities. In this thesis, novel hydrocarbon anion and cation exchange membranes were characterized electrochemically to better understand their properties and in-situ performance.

In chapter 2, mono-pH systems are explored using a catalyst coated membrane placed in a water electrolysis cell. It was found that the hydrocarbon membranes used in this research can be successfully operated in water electrolysis cells, in particular hydrocarbon anion exchange membranes with enhanced stability in base.

Hydrocarbon bipolar membranes, which consist of anion and cation exchange membrane layers, were explored in chapters 3 and 4 using a 4-electrode system. Using bipolar membranes allows for the anode and cathode reactions to occur at different pHs. In chapter 3, we showed the effects of utilizing a 3D junction at the bipolar membrane interface with and without a water dissociation catalyst. Chapter 4 illustrates how varying anion and cation exchange membrane thickness within a bipolar membrane effects performance, as measured by current-voltage curves and a novel spectroelectrochemical method. This data was then correlated with permselectivity measurements to show the relationship between permselectivity of a single bulk layer and co-ion leakage currents through the bipolar membrane. Through this work it was confirmed that bipolar membranes with high surface area junctions and water dissociation catalysts exhibit better performance. Additionally, it was shown that the thickness of individual CEM and AEM layer should be tailored to each polymer's permselectivity to maximize water dissociation efficiency. However, the bipolar membranes used in this research suffered from a lack of adhesion when using a water dissociation catalyst. Alternative methods for bipolar membrane fabrication should continue to be explored.

Keywords: ion exchange membrane; hydrocarbon membrane; bipolar membrane; water electrolysis; water dissociation; spectroelectrochemistry

To Sam, for never being surprised by my accomplishments.

Acknowledgements

I would like to thank Dr. Steven Holdcroft for giving me the opportunity to be part of his research group. I am immensely grateful to have had such an excellent mentor throughout graduate school.

I would like to thank my committee members, Prof. Corina Andreoiu and Prof. George Agnes, as well as the other faculty members of the SFU chemistry department. I appreciate the insightful comments and constructive feedback I have received at committee meetings, poster presentations, and oral presentations.

There are many members of the Holdcroft lab I would like to thank including, but not limited to, Dr. Benjamin Britton, Dr. Thomas Skalski, Dr. Patrick Fortin, Dr. Mike Adamski, Dr. Peter Mardle, Dr. Jiantao Fan, Dr. Hsu-Feng Lee, Sydney Cao and Binyu Chen. You have all provided materials, shared your expertise, and helped me immensely through this journey.

I am grateful for the SFU glass shop, machine shop, electronics shop and 4D labs. The work presented in this thesis was possible because of the instruments and hardware I had access to. I would like to thank the NiElectroCan project, SINTEF, and Vanderbilt University for the wonderful collaborations that enriched my Ph.D.

I would like to thank Diana Holton-Hinshaw and Prof. Gary Hinshaw for their continued support, encouragement and help over the past seven years. Finally, I would like to thank my parents for their encouragement, not just through graduate school, but through the many years of schooling that got me here.

Table of Contents

List of Tables

List of Figures

List of Acronyms

AC	Alternating current
AEM	Anion exchange membrane
BPM	Bipolar membrane
CE	Counter electrode
CEM	Cation exchange membrane (interchangeable with PEM)
CPE	Constant phase element, Q
DABCO	Diazabicyclo[2,2,2]octane
DC	Direct current
DFT	Density functional theory
DI	Deionized
DMAc	Dimethylacetamide
DMF	Dimethyl formamide
DMSO	Dimethyl sulfoxide
EDX	Energy dispersive X-ray spectroscopy
EIS	Electrochemical impedance spectroscopy
GDL	Gas diffusion layer
HER	Hydrogen evolution reaction
HFR	High frequency resistance
HMT-PMBI	Hexamethyl-p-terphenyl poly(benzimidazolium)
HMT-PMPI	hexamethyl p-terphenyl poly(arylene-imidazolium)
ICP-MS	Inductively coupled plasma – mass spectrometry
IEC	Ion exchange capacity
IEM	Ion exchange membrane
MEA	Membrane-electrode assembly
MW	Molecular weight
OER	Oxygen evolution reaction
PAA	Poly(acrylic acid)

PAImXY	Poly(bis-arylimidazolium), X and Y represent the alkyl chains at the N1 and N2 positions
PBI	Polybenzimidazole
PEM	Proton exchange membrane (interchangeable with CEM)
PFSA	Perfluorosulfonic acid
PTL	Porous transport layer
PVP	Poly(4-vinylpyrrolidone)
QPPO	Quaternary poly(2,6-dimethyl-1,4-phenylene oxide)
RE	Reference electrode
RH	Relative humidity
SEM	Scanning electron microscope
SPAE	Sulfonated poly(arylene) ether
SPEEK	Sulfonated poly(ether ether ketone)
SPPB	Sulfonated phenylated polyphenylene(biphenyl)
TMA	Trimethylamine
UV/Vis	Ultraviolet/Visible
WE	Water electrolysis OR Working electrode
WU	Water uptake

Chapter 1.

Introduction

1.1. The Hydrogen Economy

Through the combustion of fossil fuels, humans have had access to a relatively inexpensive and seemingly endless supply of energy for more than a century. However, as fossil fuel reserves dwindle and the environmental impacts of atmospheric carbon dioxide become increasingly threatening, alternative means of energy production and storage are vital. Models predict that by 2045 global energy consumption will have increased between 20% to 75 % from 2015. Electricity consumption is expected to grow between 150% and 300% during that time.[1] Alternative sources of energy must be utilized to meet these growing demands. Even more conservative estimates of global energy usage require a significant increase in energy from renewable sources.[2]

One notable drawback to using renewable energy sources such as wind, solar, and tidal power is that these energy sources are intermittent and often unpredictable. This leads to discrepancies between energy generation and demand creating two problems: the potential for energy deficits, and the question of what to do with excess electricity.[3] Increasing global reliance on renewables will require a suitable energy storage medium to solve these problems.

Hydrogen gas is an excellent energy storage medium as it is non-toxic, sustainable, and energy dense.[4,5] In the targets set out by the International Energy Agency, the path to net-zero CO_2 emissions by 2050 includes an astounding 30% contribution from hydrogen-based energy sources, primarily in the transportation sector.[2]

The energy density by weight of hydrogen gas is almost three times that of gasoline which makes it particularity useful for transportation. The complementary roles of battery powered electric vehicles and hydrogen fuel cell vehicles are discussed in detail by Andrews et. al.[6] The energy stored by batteries scales nearly linearly with weight; as more energy is needed the weight of the batteries increase proportionally. By

contrast, increasing energy for a hydrogen fuel cell only requires increasing the mass of hydrogen gas. This makes hydrogen fuel cells attractive for long-range and heavy duty transportation.[7,8] However, its low volumetric energy density requires storage in compressed or liquefied form, or through chemical means by using hydrides or sorbents.[9]

1.2. Hydrogen Production Methods

1.2.1. Fossil Fuel Based Methods

Although hydrogen is the most abundant element in universe, hydrogen gas is not naturally available and must be produced from raw materials such as hydrocarbons or water. In 2019 it was reported that approximately three-quarters of hydrogen was produced from natural gas with the remaining produced mainly from coal. Hydrogen may be extracted from fossil fuels using a variety of methods. Steam reformation is the process most commonly used with natural gas while partial oxidation is used for hydrogen produced from oil and coal. The majority of this hydrogen is used for petroleum refining and ammonia synthesis.[10]

For hydrogen gas to act as a clean energy storage medium, its production must be renewable. For every one tonne of hydrogen produced through the aforementioned fossil fuel based methods, between 10 and 19 tonnes of carbon dioxide are produced.[10] These emissions may be reduced through implementation of carbon capture utilization and storage but this can be costly and does not reduce emissions by 100%. Additionally, the hydrogen produced from sources like coal contain impurities which may not be suitable for applications such as fuel cells.[11]

1.2.2. Water Electrolysis

Water electrolysis (WE) describes the process in which electricity drives the splitting of water into hydrogen and oxygen gases shown in equation 1. Hydrogen and oxygen evolve at the cathode and anode, respectively, while ionic current is carried by H^+, OH^-, or a combination of both ions depending on the system used.

$$(1)\quad H_2O_{(l)} \rightarrow H_{2\,(g)} + \frac{1}{2}O_{2\,(g)}$$

This process is non-spontaneous ($\Delta G > 0$), and endothermic ($\Delta H > 0$) thus requiring electrical and/or thermal energy. The Gibbs free energy of the reaction, ΔG_R, can be calculated from the enthalpy of the reaction, ΔH_R, temperature, T, and entropy of the reaction, ΔS_R, as shown in equation 2. At standard state conditions, a pressure of 1 atm and temperature of 298.15 K, the Gibbs free energy is calculated to be 236.48 kJ mol^{-1}. In the context of an electrochemical cell the Gibbs free energy can be used to determine the voltage the cell will require or produce, as shown in equation 4, where n is the number of moles of electrons, F is Faraday's constant, and V_{cell}° is the cell voltage at standard state. Using equation 4, two voltages can be derived. One is the reversible voltage, V_{rev}°, which assumes the required thermal energy is supplied in the form of heat. The theoretical voltage, V_{th}°, is higher as it assumes that all energy is provided in the form of electrical energy. In low temperature water electrolysis the thermal heat provided to the system is small and the voltage required is closer to the theoretical voltage.[12] In practice, the operating potential of a system will always be higher than the calculated thermodynamic potential, a difference known as the overpotential.

$$\Delta G_R = \Delta H_R - T \cdot \Delta S_R \tag{2}$$

$$\Delta G_R^{\circ} = 236.483 \text{ kJ mol}^{-1} (p = 1 \text{ atm}, T = 298.15 \text{ K}) \tag{3}$$

$$\Delta G_{cell}^{\circ} = nFV_{cell}^{\circ} \tag{4}$$

$$V_{rev}^{\circ} = \frac{\Delta G_R^{\circ}}{n \cdot F} = 1.229 \text{ V} \tag{5}$$

$$V_{th}^{\circ} = \frac{\Delta H_R^{\circ}}{n \cdot F} = 1.481 \text{ V} \tag{6}$$

Though this process requires energy, hydrogen produced electrolytically is considered renewable if coupled with electricity from sources like wind and solar. Currently, electrolysis accounts for approximately 2% of global hydrogen production, although the majority of this hydrogen is collected as a biproduct of chlor-alkali electrolysis. Hydrogen produced via water electrolysis accounts for less than 0.1% of global production.[10] Different types of electrolyzers exist and are classified by the electrolyte pH, medium for ion transport, and temperature. In the context of this thesis, only low-temperature systems will be discussed.

Traditional Alkaline Water Electrolysis

Alkaline electrolyzers have been used in industry for over 100 years. The systems traditionally used consist of two electrodes immersed in a basic solution of 30 wt% KOH separated by a porous diaphragm. However, the use of a liquid electrolyte is not ideal for several reasons. These systems cannot operate at high current densities due to the resistance of the liquid electrolyte and diaphragm.[13] The presence of gas bubbles within the solution and on the electrode surfaces also contribute significantly to this resistance.[14] To separate the anode and cathode a porous diaphragm is used. However, this diaphragm does not adequately separate product gasses leading to reduced efficiency and explosive mixtures of hydrogen and oxygen gases.[15] Thus, operation under partial loads and differential pressures is also problematic due to product gas mixing.[13] These systems have historically been described in literature as requiring relatively high potentials of 1.8 – 2.4 V at low current densities of 200 – 400 mA cm^{-2}.[16–18] Some companies are now advertising higher performing systems which operate at 1.9 - 2.1 V at upwards of 1.2 A cm^{-2}.[19]

Proton Exchange Membrane Water Electrolysis

Solid polymer electrolyte membranes have been introduced as replacement to the aforementioned porous diaphragms and caustic solution, as shown in figure 1.1. These thin polymer membranes provide better physical separation of the electrodes, preventing mixing of the product gasses, while conducting ions. The shorter distance between the electrodes leads to a lower ionic resistance, thus lower cell potential.[12] Additionally, these systems may be operated under a differential pressure producing compressed hydrogen at the cathode without pressurization of gases at the anode. This leads to a more energetically favorable method of compression at certain pressures.[12,20]

Unlike traditional alkaline systems, the first solid polymer electrolytes used were acidic in nature. These are known as proton exchange membranes (PEM) or cation exchange membranes (CEM) and consist of polymers functionalized with acidic groups, such as sulfonic acid ($-SO_3^-H^+$). Perfluorosulfonic acid (PFSA) membranes such as Nafion™ are commonly used.[16] In a PEM water electrolyzer (WE), deionized (DI) water is fed into the positively polarized anode where the oxygen evolution reaction (OER)

takes place. The H^+ ions formed at the anode migrate through the membrane to the cathode where the hydrogen evolution reaction (HER) takes place. A notable drawback to using PEMs over alkaline systems is the need for rare platinum group metal catalysts such as platinum, palladium, and iridium which significantly increase the cost of the electrolyzer stack. Figure 1.1 shows a simplified diagram of a proton exchange membrane sandwiched between two electrodes. At each electrode is the half-reaction, potential, and commonly used catalysts. PEM-WE typically shows lower potentials, 1.8 – 2.2 V at higher current densities, 0.6 – 2.0 A cm^{-2}, than traditional alkaline systems.[16,17]

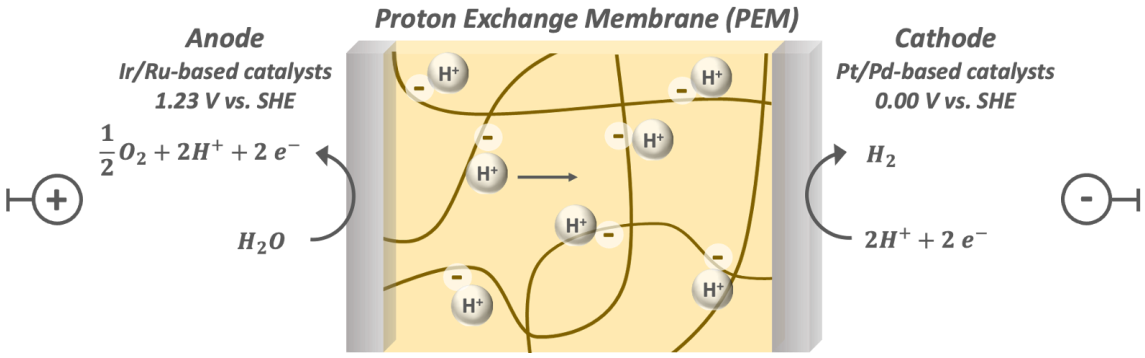

Figure 1.1 **Diagram of a proton exchange membrane water electrolyzer. Protons migrate from anode to cathode through a polymer with fixed negative charges. Reactions at the anode and cathode electrodes and commonly used catalysts are shown.**

The engineering and fabrication of PEM-WE cells are similar to that of PEM fuel cells. A diagram of typical cell construction is shown in figure 1.2. The catalysts layers at the anode and cathode act as the two electrodes. These are typically formed by evaporation of a catalyst ink comprised of the catalyst, ionomer, water, and a low boiling point solvent such as methanol. In the case of Pt, these particles are usually on a conductive carbon support. The ionomer is a proton conducting polymer, often similar or identical to the PEM, which may be added to the ink in the form of a solution or dispersion. Once hydrated, the ionomer serves as a channel to conduct protons through the catalyst layer at the anode, into the membrane, and then to active sites in the cathode. Catalyst inks are formulated and applied such that an interconnected web of both proton-conductive ionomer and electron-conductive catalyst/support particles are formed, thus

maximizing reaction sites. Gas diffusion layers (GDL), also referred to as porous transport layers (PTL), provide electrical contact between the catalyst layers and gas flow channels as well as providing efficient mass transport of liquid and gas.[12] At the anode the GDL is often made of platinized titanium. Titanium corrodes very little under high anodic potentials and acidic conditions and is platinized to prevent the formation of TiO_2 which increases the resistance of the GDL. Carbon cloth paper can also be used as the cathode GDL. Gasketing surrounds the gas diffusion layer to ensures that all components make good electrical contact and prevents leakage of solution.

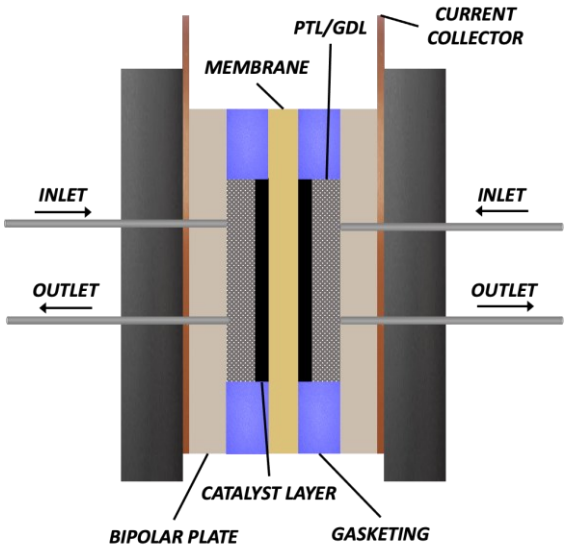

Figure 1.2 **Diagram of single water electrolysis cell utilizing an ion exchange membrane. At the center is the membrane which conducts either protons or hydroxide ions. Chemical reactions occur in the catalyst layers on either side. The porous transport layers (PTL), also referred to as the gas diffusion layers (GDL), sits between the bipolar plate and catalyst layer.**

Anion Exchange Membrane Water Electrolysis

Recently anion exchange membranes (AEM) have been explored as solid polymer electrolytes for water electrolysis. A simplified diagram of an AEM-WE cell is shown in figure 1.3. Switching from PEM to AEM systems provides all the advantages of a solid polymer electrolyte, i.e. low ohmic losses and lower gas crossover and allows lower-cost components and catalysts to be used.[21] Another advantage to using AEMs in water

electrolysis is that these systems are less affected by impurities in the feed water.[22] High purity deionized water is necessary for PEM systems as the presence of cations in the water feed has been shown to create fouling of the membrane in similar systems.[23]

AEM-WE cells are constructed in a similar fashion to PEM-WE cells, except for that carbon GDL and carbon supported catalyst are replaced by titanium and unsupported catalysts to prevent oxidation of carbon at the anode. Despite recent progress, limitations to AEM-WE have prevented large scale adoption. These include the lower performance of non-noble metal catalysts, the continued need for high pH electrolyte feeds, and most importantly poor durability of the AEM and ionomer which will be discussed in detail in section 1.3.3. [21]

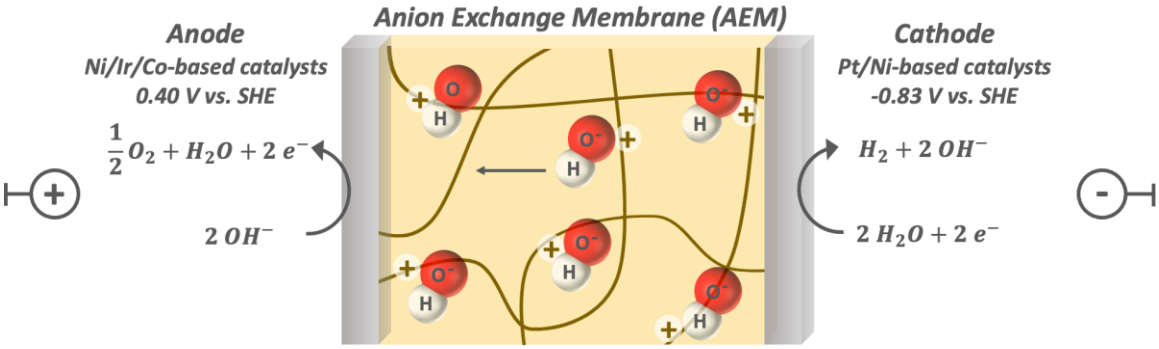

Figure 1.3 Diagram of an anion exchange membrane water electrolyzer. Hydroxide ions migrate from cathode to anode through a polymer with fixed positive charges. Reactions at the anode and cathode electrodes and commonly used catalysts are shown.

1.3. Ion Exchange Membranes

1.3.1. Overview

Ion exchange membranes (IEM) are widely used for separation processes. They are non-porous membranes with fixed ionic groups and are, thus, conductive to ions and hydrophilic.[24] IEMs can be classified based on the membranes materials, microstructure, fixed ionic groups.[25] In the context of water electrolysis, this thesis will discuss polymers which fall under two material classifications: hydrocarbon membranes and perfluorocarbon membranes, and three fixed ionic group classifications: cation/proton

exchange membranes (CEM/PEM), anion exchange membranes (AEM), and bipolar membranes (BPM).

Several properties are necessary for an IEM to properly function within a water electrolysis cell. The membrane must be electrically insulating but have a low resistance to ionic current. It should have a high permselectivity, meaning that it is highly selective toward the desired mobile ion, as well as high chemical and mechanical stability, and low gas permeability.[12]

1.3.2. Proton Exchange Membranes

Proton exchange membranes (PEM), sometimes referred to as cation exchange membranes (CEM), have been widely studied for applications in fuel cells. More recently, there has been a significant shift toward studying PEMs for water electrolysis.[12] These membranes contain immobile anionic groups, most commonly sulfonic acids, which allow for the conduction of cations. In most applications discussed in this thesis, the mobile cation with be a proton, H^+. For decades, perfluorinated sulfonic acid membranes (PFSA), namely DuPont's Nafion membrane, have been most commonly used in fuel cell and electrolyzer devices due to their high conductivity and robust mechanical and chemical stability.[26] These membranes consist of a fluorinated Teflon™ backbone with pendant sulfonic acid groups with allow for the transport of cations through the polymer matrix. The structure of Nafion is shown in figure 1.4.

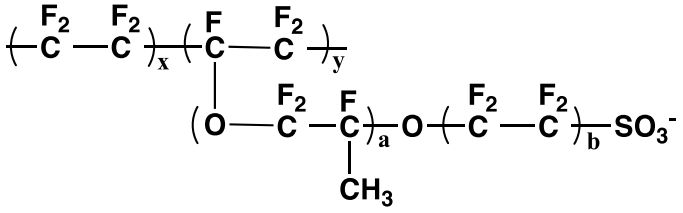

Figure 1.4 Chemical structure of DuPont's Nafion™ membrane. Typically, a≥1, b=2, x=5-13.5, y=1000. Similar fluorinated PEMs exist with varying values for these repeating units.[27]

The perfluorinated structure of Nafion allows for a separation of hydrophobic and hydrophilic domains. At sufficient hydration, cations can be transported through water-rich channels due to the pendant sulfonic acid groups, while the hydrophobic backbone

provides mechanical stability.[28] However, Nafion undergoes morphological changes around its glass transition temperature, T_g, of approximately 100° which negatively impacts its functionality at high temperatures. Additionally, these membranes are difficult to synthesize and dispose of and show high fuel permeability. [12,29,30] For these reasons, hydrocarbon PEMs have been widely studied as a replacement for PFSAs.

Many hydrocarbon PEMs consist of aromatic polymer backbones which provide high glass transition temperatures.[26] Common hydrocarbon PEMs for fuel cell and water electrolysis applications are sulfonated polystyrene[31], poly (ether sulfone),[32] sulfonated poly (ether ether ketone) (SPEEK)[33,34], and sulfonated polybenzimidazole (PBI) derivatives[35]. Structures are shown in figure 1.5.

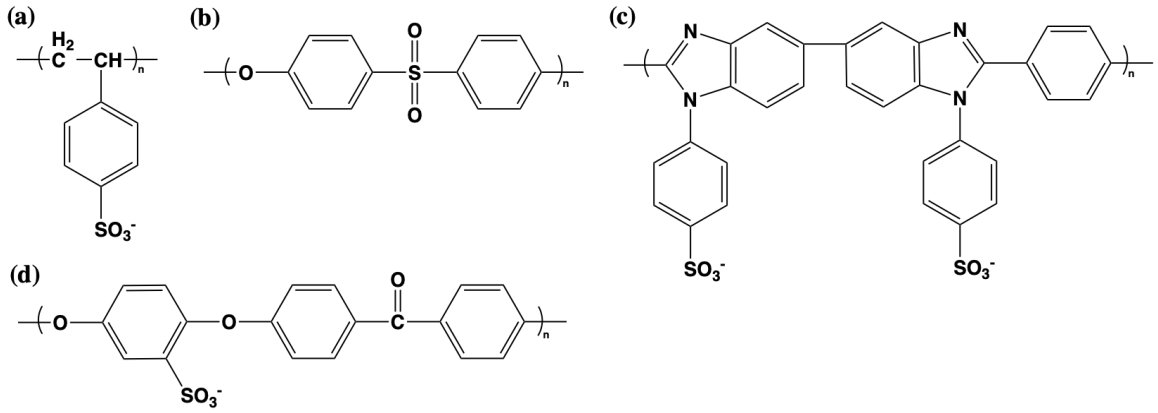

Figure 1.5 Structures of common hydrocarbon PEMs. (a) sulfonated polystyrene, (b) poly (ether sulfone), (c) sulfoarylated polybenzimidazole, (d)Sulfonated poly (ether ether ketone)

1.3.3. Anion Exchange Membranes

Anion exchange membranes (AEM) conduct anions due the presence of cationic groups on either the backbone or side chains of the polymer. Typical cationic groups include quaternary ammoniums[36–38], bicyclic ammonium systems like 1,4-diazabicyclo[2.2.2]octane (DABCO)[39,40], imidazolium[41–43], benzimidazolium[44–46], guanidinium systems[47,48], and P-based systems[49,50]. Structures of these groups are shown in figure 1.6.

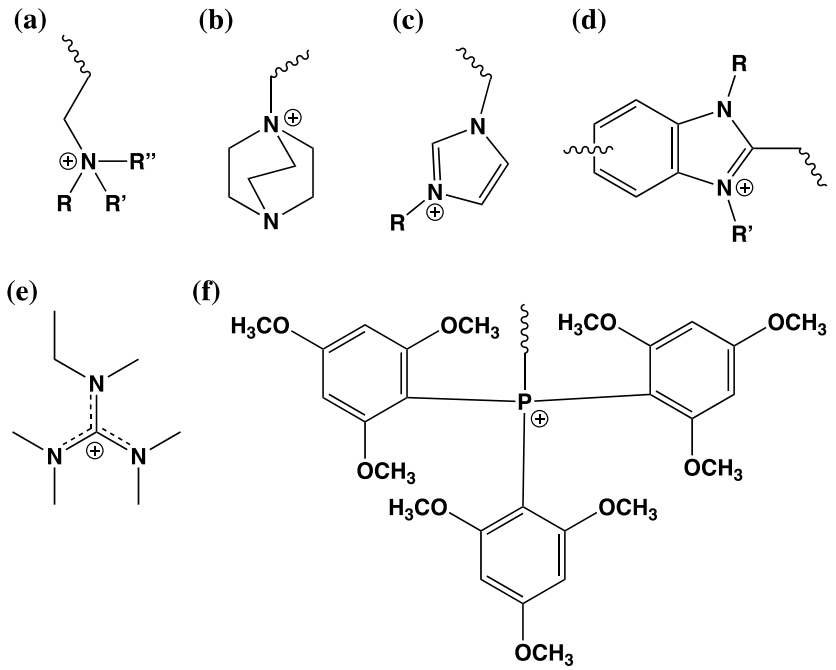

Figure 1.6 Common cationic groups in AEMs. (a) quaternary ammonium, (b) DABCO, (c) imidazolium, (d) benzimidazolium, (e) guanidinium, (f) quaternary phosphonium.

Currently there are two main drawbacks to using AEMs. One is that they are generally less conductive than PEMs. This partially results from the lower mobility of OH^- compared to H^+.[51] Additionally, an AEM in OH^- form will quickly convert to the CO_3^{2-} and HCO_3^- forms upon exposure to CO_2-containing air which only further decreases the average anion mobility.[52] Secondly, AEMs have historically lacked robust chemical stability in highly alkaline solutions.[22] There are many degradation mechanisms possible resulting from OH^- attack shown in figure 1.7. A significant pathway for AEM degradation is through the nucleophilic substitution reaction of the OH^- with an α-H. β-Hs are also at risk of hydroxide attack, a process known as Hofmann elimination. Significant progress in AEM chemical stability has been made by sterically hindering the C2 position of imidazolium and benzimidazolium functional groups.[43,46]

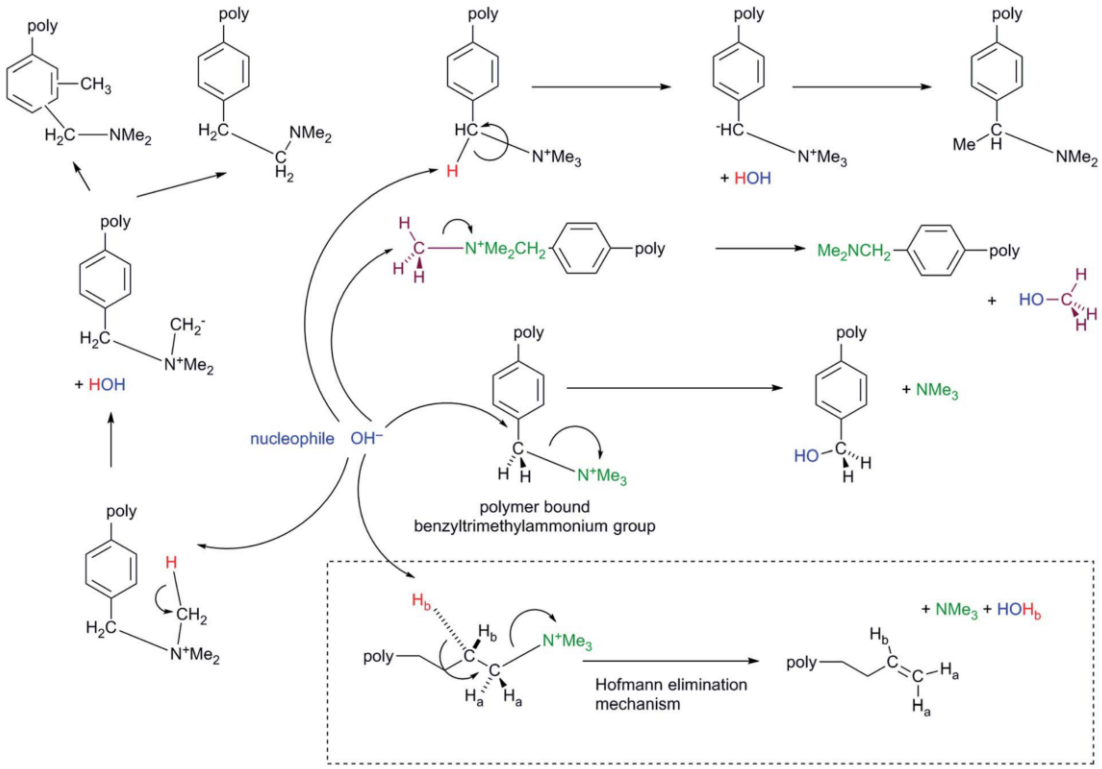

Figure 1.7 Common degradation pathways for anion exchange membranes in the presence of strong base. Reproduced from Ref 21 under the terms of CC by 3.0 license https://creativecommons.org/licenses/by/3.0/legalcode.

1.3.4. Characterization of Ion Exchange Membranes

Characterization of an ion exchange membrane for use in energy conversion devices typically reports the number of fixed charges present in the membrane, conductivity, solubility in water and common solvents, water uptake, dimensional swelling, mechanical strength, and chemical stability among other characteristics. The ion-exchange capacity (IEC) of an IEM describes the number of function groups per unit mass of polymer (molar equivalent/g). It is important to note that the mobile ion is included in the unit mass of polymer and thus the IECs for OH^- and Cl^- forms of an AEM are slightly different. Both a theoretical IEC, based on the chemical structure, and experimental IEC can be calculated. Experimentally, the IEC can be measured by converting a known mass of membrane to the H^+ or OH^- form, for PEMs and AEMs, respectively, and then exchanging it in a concentrated salt solution. The concentration of acid or base in solution is determined through titration and thus the number of ion

exchange sites per unit mass is found. This back titration method is commonly used for PEMs but used less frequently for AEMs as strong base often causes degradation of the polymer and will quickly convert to CO_3^{2-}/HCO_3^-.[53] To combat these issues the IEC of an AEM is often measured when the membrane is in Cl^- form using the Mohr method. In this method the membrane, in Cl^- form, in exchanged in a solution of Na_2SO_4 and then titrated with $AgNO_3$ and a K_2CrO_4 indicator until the Cl^- have been fully consumed and Ag_2CrO_4 forms.[54] As IEC increases, the conductivity of the IEM usually increases as well. However, with increasing water content the concentration of protons decreases causing which can cause a significant decrease in conductivity.[55] Additionally, membranes with very high IECs are highly hydrophilic and may dissolve in water at elevated temperatures, thus limiting their usefulness in energy conversion devices.[22]

One of the most important properties of ion exchange membranes is their conductivity. This is typically measured using electrochemical impedance spectroscopy (EIS) in an a two or four-electrode cell. The use of an environmental chamber allows membrane conductivity to be measured as a function of temperature and relative humidity, RH%. Conductivity typically increases as temperature and RH% increase. As previously noted, the conductivity of AEMs in the OH^- form can be compromised by carbonation from atmospheric CO_2. Ziv et al. introduced a method for measuring the correct AEM conductivity utilizing a constant current applied across working and counter electrodes in direct contact the hydrated membrane with humidified N_2 passed through the cell.[56] The constant production OH^- at the cathode allowed CO_3^{-2} and HCO_3^- to be fully flushed from the system. The true hydroxide conductivity was measured through reference and sense electrodes in the middle of the membrane sample. This method was confirmed visually using an AEM prepared with inclusion of the pH indicator thymolphthalein by Cao et al.[57]

Dimensional swelling, water uptake, and water content are important for understanding how ion exchange membranes will conduct ions and function in an electrochemical device. Dimensional swelling measures the percentage expansion of a fully hydrated membrane compared to a dry membrane. This can be done by comparing the length of the dry and hydrated membrane, l_d and l_w, respectively, in the x, y, or z-plane using equation 7.[54] Dimensional swelling can be affected by IEC, ionic species,

cross-linking of the polymer, and the use of reinforcements in the membrane.[24] Membranes with high degrees of dimensional swelling can wrinkle and show poor mechanical integrity.[58] Water uptake refers to the change in mass between wet and dry membranes, m_w and m_d, respectively, and is given in equation 8.[54] The water content (λ), sometimes referred to as the hydration number, is a measure of the number of water molecules per ion exchange site and is given in equation 9.[54,59]

$$(7) \qquad Dimensional\ Swelling = \frac{l_w - l_d}{l_d} \times 100\%$$

$$(8) \qquad Water\ Uptake\ (WU) = \frac{m_w - m_d}{m_d} \times 100\%$$

$$(9) \qquad Hydration\ Number\ (\lambda) = \frac{WU(\%) \times 10}{18 \times IEC}$$

The mechanical strength of an IEM is typically characterized using a tensile test in which a piece of the polymer is stretched until it fractures. Results are shown in a stress-strain curve from which the Young's modulus, tensile strength, and elongation at break of the polymer can be determined. Brittle polymers break at low elongation, while more flexible polymers show a greater elongation at break.[60]

The chemical stability of an IEM is extremely important for its longevity in electrochemical devices. As previously mentioned, AEMs have historically exhibited poor chemical and mechanical stability under high pH conditions. To test the chemical stability of AEMs, membranes are usually immersed in high pH solutions, often at elevated temperatures. Signs of degradation can be observed by dissolution, i.e., measuring the weight change of the membrane, or through NMR studies which may elucidate the degradation mechanism.[43,61,62] The chemical stability of PEMs is often investigated using Fenton's test in which the PEM is heated in a solution containing approximately 3% H_2O_2 and 3 ppm $FeSO_4$.[63] The purpose of this solution is to facilitate the formation of hydroxyl (HO·), hydroperoxyl (HOO·), and hydrogen (H·) radicals.[64] These radicals are formed during PEM fuel cell operation as O_2 reactant gas permeates from the cathode to anode where it reacts on platinum to form H_2O_2. H_2O_2 can then react with impurities to form radicals which attack the PEM.[63] Besides ex-situ studies, extensive work has been done to understand how the operating conditions of PEM water electrolyzers and fuel cells impact free radical formation and the degradation of all components, including the membrane.[65–67]

1.4. Bipolar Membranes

1.4.1. Overview

Single membrane systems are limited to operation at a single pH. To circumvent this limitation, both AEM and CEM materials can be combined to allow half-cell reactions to take place in acidic and basic conditions, respectively. This is called a bipolar membrane (BPM). Note that the term cation exchange membrane (CEM) is often used in place of proton exchange membrane (PEM) in BPM literature. Both terms will be used throughout this thesis. Using a BPM allows for operation across a pH differential. In the case of water electrolysis this yields a cell that combines the favorable kinetics of the hydrogen evolution reaction at low pH with the favorable kinetics of the oxygen evolution reaction at high pH. Furthermore, BPMs enable the use of non-noble catalysts at the anode, decreasing cost.[21,68,69]

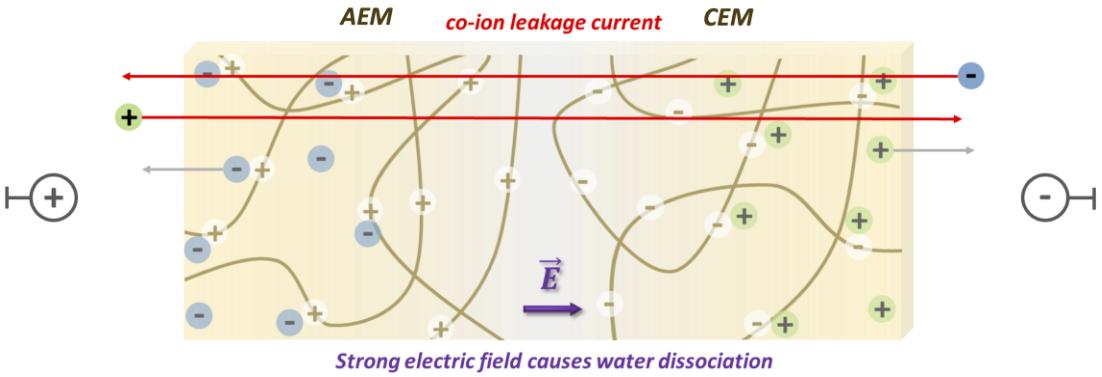

Figure 1.8 **The bipolar membrane (BPM) interface under reverse-bias polarization. Co-ion leakage currents, the movement of anions from catholyte to anolyte and cations from anolyte to catholyte are shown with red arrows. A breakdown of electroneutrality and creation of an electric field occurs at (BPM) interface due to the absence of mobile ions.**

Bipolar membranes consist of a conjoined AEM and CEM. The area in which the two membranes are in direct contact is called the BPM junction or interfacial layer. Water splitting occurs when the membrane is operated under reverse-bias: a cathodic potential is applied to the electrode on the acidic side, and an anodic potential is applied to the electrode on the alkaline.[70] Ionic current may be carried by co-ion leakage, as

shown in figure 1.8, or through water dissociation. Co-ion leakage occurs because the membranes are not perfectly permselective meaning that anions may travel through the CEM and cations through the AEM. A space charge region exists at the interface under equilibrium.[71–73] Upon polarization this region increases in width creating a strong electric field shown in figure 1.8. To maintain electroneutrality throughout this process, water dissociates at the PEM|AEM interface in the space charge region, a thin region on the order of tens of nanometers, where the AEM and PEM are in contact, at increased rates due the second Wein effect.[74] The second Wein effect describes the increased dissociation of weak electrolyte solutions under the influence of an electric field which occurs as the molecular dipoles stretch and align with the field.[70,75] For water, proton transfer occurs nearly instantaneously with the rate-limiting step being reorientation of water molecules. Thus, within the electric field, the alignment of water molecules is presumed to result in enhanced dissociation as shown in figure 1.9.[76,77] Protons diffuse through the PEM to the cathode, and hydroxide ions diffuse through the AEM to the anode maintaining a pH difference.

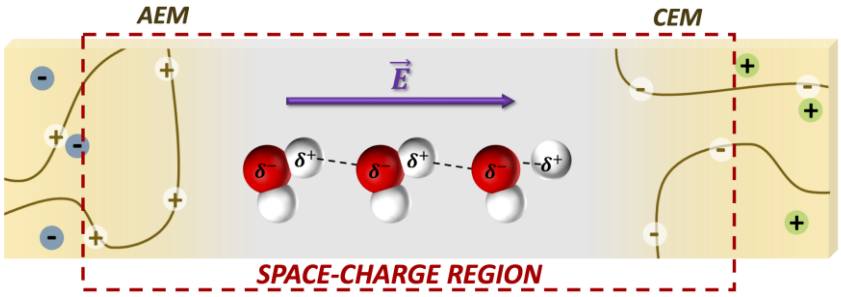

Figure 1.9 **A closer look at the bipolar membrane interface under reverse-bias polarization. A strong electric field forms in a region referred to as the space-charge region. Here, water molcules align such that rapid proton transfer is possible.**

Frilette first demonstrated that the current-voltage relationship of bipolar membranes was anisotropic in nature, meaning that polarization curves run under forward bias and reverse bias yield different current-voltage characteristics. The bipolar membrane exhibited a much greater resistance when run under reverse-bias conditions.[78] This work showed that the ionic current under reverse-bias is carried not only by ions in the electrolyte, but also by protons and hydroxide ions resulting from water dissociation within the BPM.

To better under the relationship between water dissociation and co-ion leakage currents, Simons et. al. measured the rate of water dissociation by measuring the pH change in solutions adjacent to the membrane after holding the cell at various potentials for an extended time.[70] It was found that no discernible water dissociation occurred under low potentials (<300 mV); whereas under higher potential (>3 V) water dissociation accounted for 60% of the current passed. This demonstrated that below a threshold voltage, ionic current must be due to co-ion leakage. Ramírez et. al. was the first to relate water dissociation to the current-voltage characteristics in reverse-bias polarization curves and postulated that the point on the current-voltage curve which exhibited the highest resistance was the point at which water dissociation became the dominant form of ion transport.[73]

The interface of the BPM is viewed as a critical feature of this technology, as it is responsible for splitting water into protons and hydroxide ions. Current research suggests that the interface must be as thin as possible to maximize dissociation, but possess a certain degree of interpenetration of the polymers that comprise the PEM and AEM to create sufficient adhesion between the two membranes.[79] Early studies report that when a single membrane was subjected to an electric field, water dissociation only occurred in the presence of groups typically found in anion exchange membranes, such as quaternary and tertiary amino groups.[77,80] Simons explored this further by observing water dissociation in the presence of different salts and amino acids.[81] This led to Simons' hypothesis that water dissociation occurs through proton transfer between water molecules and neutral acids and bases with pKa values between 4 and 10. The presence of materials such as $Al(OH)_3$ and graphene oxide have also been shown to increase the efficiency of water dissociation.[82,83] This is explained by the ability of these catalysts to participate in protonation and deprotonation reactions, and their hydrophilicity, which increases ion conductivity within the membrane.[84,85] Recent work by Oener et al. has also shown that catalyst activity toward the water dissociation reaction is directly correlated with their activity toward the hydrogen evolution reaction in alkaline conditions.[86]

The fabrication method also plays a critical role in BPM performance as it determines the structure of the interfacial layer. Some methods, such as spray coating or solution casting a polymer onto a preformed membrane, introduce additional complexity.

This is because they affect not just the interfacial layer, but the properties of one or both bulk regions, the large membrane regions on either side of the thin interfacial region. In contrast, lamination of pre-cast membranes by hot-pressing is a straightforward technique that allows both the bulk AEM and PEM to be cast from solution at optimal conditions before formation of the BPM. However, this method results in a low surface area interface and weak membrane adhesion, as the adhesion comes only from electrostatic interactions between the two polymers.

1.4.2. Applications of Bipolar Membranes

Electrodialysis

Bipolar membranes were first used commercially for electrodialysis systems. Unlike conventional electrodialysis, which separates fresh and salt water using cation and anion exchange membranes, these systems utilize bipolar membranes to convert salt water into acid and base.[87] BPM electrodialysis is also used for separation of organic acids during fermentation processes and recovery of hydrofluoric and nitric acid during steel processing.[88] A simplified diagram of a single electrodialysis cell is shown below in figure 1.10.

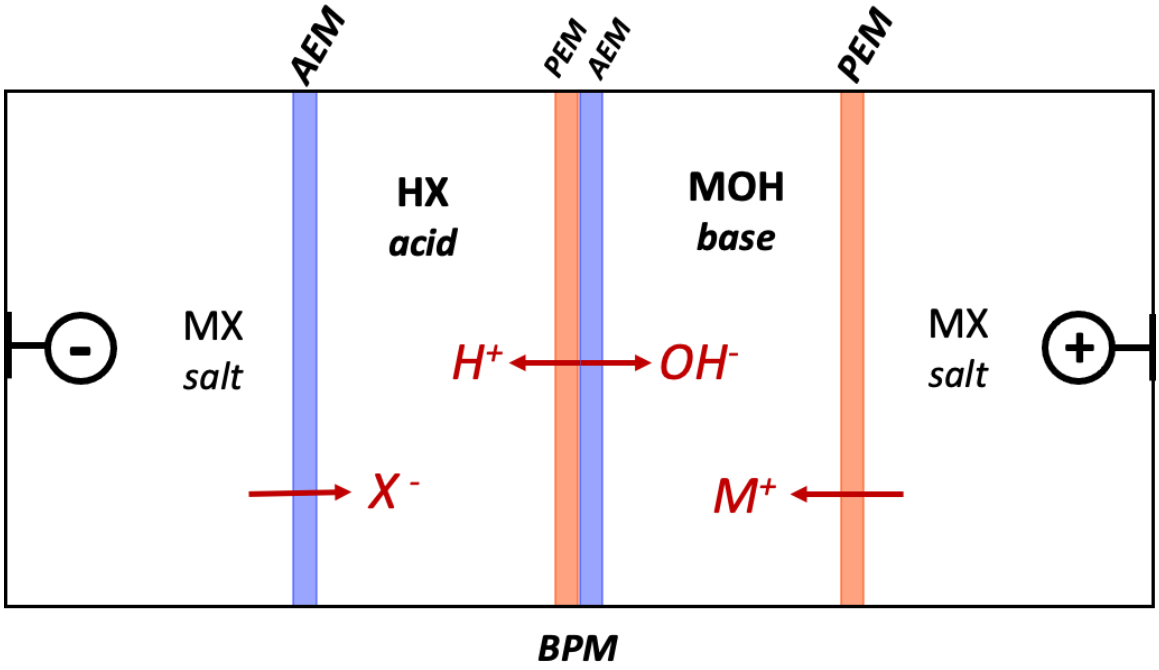

Figure 1.10 **Schematic of an electrodialysis cell. A bipolar membrane (BPM) under reverse-bias polarization produces protons and hydroxide ions. Cations (M^+) from an adjacent salt stream migrate through a proton exchange membrane (PEM) while anions (X^-) similarily migrate though an anion exchange membrane (AEM). This ions combine with the protons and hydroxide ions produced by the BPM such that acid and base streams are produced from salt solution and water.**

Water Electrolysis

Recently bipolar membranes have been explored for hydrogen generation in water electrolyzer systems with much of the initial work focused on solar water splitting.[89–98] Few works have implemented BPMs in more traditional electrolyzer systems, i.e. a zero-gap, single-cell stack design, as shown in figure 1.2.

Giesbrecht et al. reported on a vapor-fed bipolar membrane using Nafion and poly(benzimidazolium) membranes.[99] In that work membrane-electrode assemblies (MEA) were formed by hot-pressing catalyst loaded gas diffusion layers (GDL) to Nafion membranes. To form a bipolar junction, the AEM, hexamethyl-p-terphenyl poly(benzimidazolium), HMT-PMBI, was incorporated into the anodic ink at different weight percentages allowing for the use of [NiFe]-layered double hydroxide catalyst. The BPMs (NiFe anode catalyst) showed comparable performance to a fully acidic Nafion

MEA (IrO_x anode catalyst) during polarization curves. However, long-term durability studies showed that although the BPM was stable 16 hours of continuous operation at 10 mA cm^{-2}, the overpotential of the BPM was between 100 – 200 mV higher than that of the acidic MEA. This overpotential was attributed to the water dissociation reaction occurring within the BPM.

Mayerhöfer et al. reported the first liquid-fed, zero-gap bipolar membrane water electrolyzer.[100] Using Nafion 211 and Aemion™ (Product Numbers: AF1-HNN8-35-X and AF1-HNN8-50-X) from Ionomr Innovations Inc., water electrolysis data was collected using bipolar membranes with and without interfacial catalysts. It was found that the cell performance was greatly improved with the addition of a thin IrO_2 catalyst layer between the AEM and PEM layer with voltages reaching 2.3V at 600 mA cm^{-2}. Even better performance was observed when the bipolar interface was shifted very close to the anode such that IrO_2 catalyst at the anode was in direct contact with the AEM|PEM interface. This configuration exhibited cell voltages of 2.2 V at 8 A cm^{-2} and was stable at 100 hours at 2000 mA cm^{-2}. The authors note that this performance occurred only when using a low ion exchange capacity (IEC), a surprising finding given that the higher IEC polymer would conduct ions and transport water more easily. This result may be due to the difference in permselectivity between the high and low IEC polymers, a topic further explored in chapter 4 of this thesis.

Oener et al. reported on BPMs utilizing Sustainion® AEM and Nafion CEM layers.[101] This work characterized BPMs with different CEM layer thicknesses both including and excluding water dissociation catalysts. BPMs with a thinner CEM layer, 2 μm compared to 50 μm, exhibited much lower cell potentials. Though the smaller ohmic contributions of a thin membrane undoubtably played a role in the better performance, the authors attribute much of this increased performance to improved water transport through the thin CEM layer. This is validated by showing the irreversible damage that occurs in a water starved Nafion electrolyzer at high current densities but which occurs to a much lower extent in the water starved Sustainion electrolyzer.

Lee et al. prepared bipolar membranes by hot-pressing a dual-sulfonated poly(arylene ether ketone) and butyl-N_3-substitiuted imidazolium-functionalized

poly(arylene ether ketone) without inclusion of an interfacial layer catalyst.[102] A single cell water electrolyzer was prepared by hot-pressing the BPM and catalyst coated gas diffusion layers. Unlike the previous works discussed in this section which used liquid for vapour water feeds, the authors fed 1 M H_2SO_4 and 2 M KOH to the cathode and anode, respectively. The BPM performed well, exhibiting a cell voltage of 1.59 V at 20 mA cm^{-2} when operated at room temperature.

Though BPMs have been well studied, few papers have utilized them for two-electrode, zero-gap configurations. Thin CEM and AEM layers have been studied but with mixed results, as the properties of the BPM depend heavily on the properties of the interfacial layer and individual properties of the CEM and AEM polymers.

Table 1-1 Comparison of materials and operating conditions for traditional alkaline, PEM, AEM, and BPM water electrolysis methods.

	Traditional Alkaline Electrolysis	PEM Water Electrolysis	AEM Water Electrolysis	BPM Water Electrolysis
Electrolyte/ Separator	~30% KOH electrolyte/ white porous asbestos diaphragm ($Mg_3Si_2O_5(OH)_4$)[17] or ceramic titanates $CaTiO_3/BaTiO_3$ [103]	PEM; typically, PFSA/ DI water feed to anode	AEM/ Dilute electrolyte, HCO_3^-/CO_3^- or KOH[16]	PEM and AEM/water vapor[99]; DI water[100,101], 1M H_2SO_4\2M KOH[102]
Cathode Catalyst	Ni/ Ni-Mo alloys[16,17]	Pt/ Pt-Pd[16]	Ni/Ni alloys[16] (Pt/C still used extensively at research scale)	Pt/C[99–102]
Anode Catalyst	Ni/ Ni-Co alloys[16,17]	IrO_2/ RuO_2[16]	Ni/ Co/ Fe oxides[16]	NiFe[99], IrO_2[99–101], Pt/C[102]
Operating Current Density (mA cm-2)	Historically: 200-400 [17,18] Recent commercial: 1,200[19]	600-2,000[16]	200-1,000[16]	2,000[100]
Voltage (V)	Historically:1.8 – 2.4[16,18] Recent commercial: 1.9-2.1[19]	1.8-2.2[16]	1.8-2.2[16]	1.68-1.72[100]

Table 1-2 Advantages and disadvantages of alkaline, PEM, AEM, and BPM water electrolysis methods.

	Traditional Alkaline Electrolysis[15]	PEM Water Electrolysis[15,16]	AEM Water Electrolysis[16]	BPM Water Electrolysis[99–101]
Advantages	• Technologically mature • Low-cost catalysts • Long-term stability	• High current densities • Compact design • Improved gas crossover compared to diaphragm • Rapid system response • Ability to operate under pressure • Fast HER kinetics	• Low-cost catalysts • Compact design •	• Low-cost anode catalyst (OER) • Fast HER kinetics
Disadvantages	• Low current densities • Large amounts of caustic electrolyte • High gas crossover • Sluggish HER kinetics	• High-cost noble metal catalysts • Commercially available on small scale	• Laboratory scale • Poor membrane stability • Sluggish HER kinetics	• Poorly studied; Laboratory scale (in context of water electrolysis)

1.5. Experimental Methods

1.5.1. Current-Voltage Characteristics of Electrolyzer Systems

Two-electrode Measurements with Proton and Anion Exchange Membrane Water Electrolyzers

Current voltage curves, also called I-V curves, or polarization curves are a common method for characterizing and comparing the performance of water electrolyzers. Current voltage curves may be performed by slowly scanning the voltage while measuring current density or vice versa. Alternately, a particular voltage or current density may be held for an adequate amount of time to ensure the cell has reached a steady state before recording the corresponding current density or voltage.

Measurement of current voltage curves allows the overpotential at a specific current density to be measured. The overpotential is defined as the additional potential, above the theoretical water dissociation potential, required for the cell to operate. The total overpotential of the cell can be classified into three distinct regions depending on the individual overpotentials which the dominate the curve.[12] At low current densities there is a rapid increase in voltage consistent with the overpotentials of the OER and HER occurring at the anode and cathode, respectively. This is called the kinetic region, and is shown in figure 1.8. The individual over potentials and their contribution to the total cell overpotential is shown is figure 1.9. It is clear that this region is dominated by the anode and cathode activation. Though the exact overpotentials are estimated, it is clear that the overpotential associated with the OER is much larger than that of the HER. This is true is acidic and basic conditions, although the difference is more pronounced in acid, and arises from the more complex, multi-electron mechanism of the OER.[16,104]

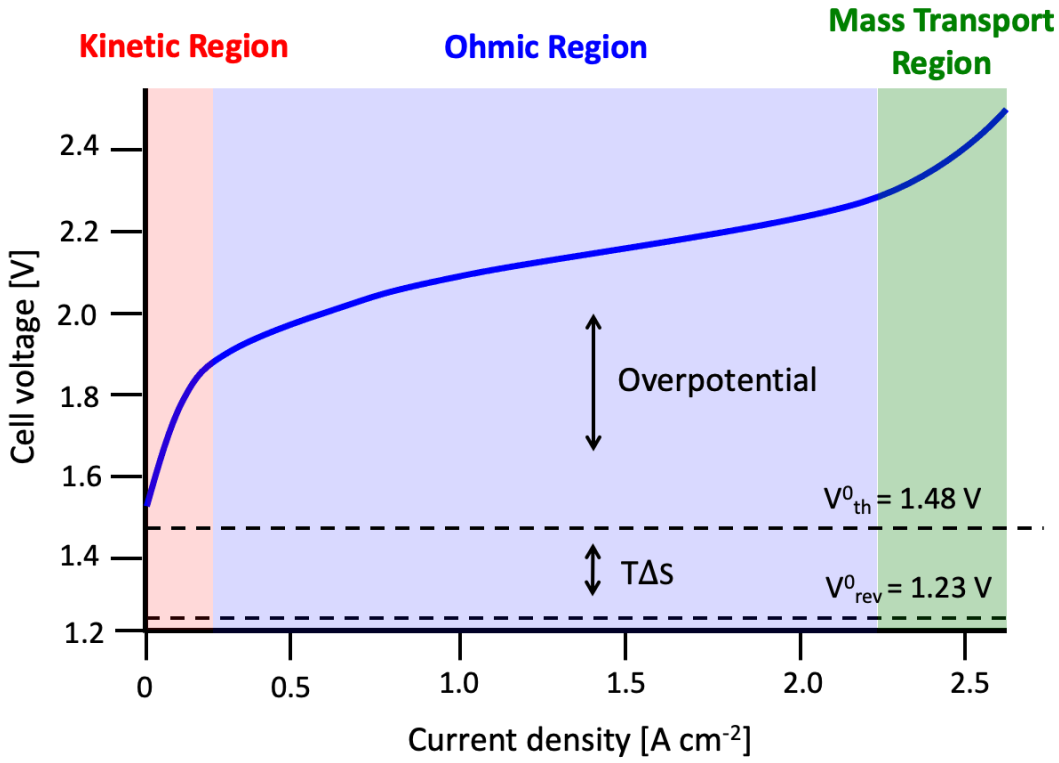

Figure 1.11 **Typical current-voltage curve for a water electrolysis cell divided into kinetic, ohmic, and mass transport regions. Both the reversible, V^0_{rev}, and thermoneutral, V^0_{th}, voltages are shown. The difference between these voltages is the thermal contribution, TΔS. This may be supplied through an external heating source, leaving a required voltage of 1.23 V, or through the applied voltage thus requiring 1.48 V. The difference between the calculated theoretical voltage and the measured voltage is called the overpotential.**

The second region of the current-voltage curve is the ohmic region. This region arises from the ohmic losses largely associated with ion transport through the membrane. Because it is dependent on the resistance of the cell, it is usually linear following Ohm's law, V=IR. The third region of the curve is called the mass transport region and is caused by mass transport limitations at the electrodes. At high current densities a larger volume of oxygen and hydrogen are produced at the electrodes. These gases can form bubbles which block active catalyst sites from reactants and cause a large increase in the voltage needed to maintain the current density.

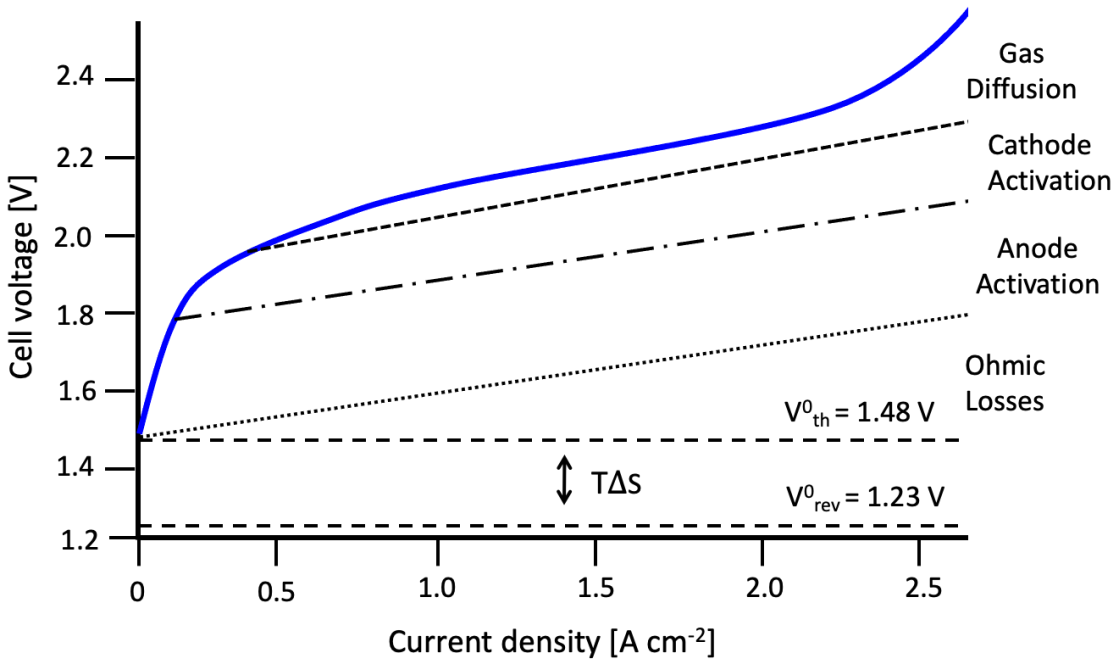

Figure 1.12 Estimated individual overpotential contributions to typical current-voltage curve for a water electrolysis cell assuming all required energy is supplied in the form of electricity.

Four-electrode measurements with Bipolar Membrane Water Electrolyzers

Current-voltage curves may also be taken using a four-electrode system, as is commonly done with bipolar membranes. In such a system current is passed through the working and counter electrodes with reference electrodes placed on either side of the BPM. This allows for the potential across the membrane to be measured without contributions from the OER or HER at the electrodes.

A typical current-voltage curve for a bipolar membrane is shown in figure 1.10. Under forward bias the membrane shows a somewhat linear response as cations and anions migrate through the CEM and AEM, respectively, and accumulate in the BPM interface. Under reverse bias, two distinct limiting current density regions are observed. The first is believed to be largely due to co-ion leakage. It's clear, however, that water dissociation also occurs in this region.[105,106] After this limiting current density water

dissociation is the primary driver of ionic current. If the cell is run to very high current densities a second limiting current region can be observed. This limiting current density results from insufficient water transport to the interface.

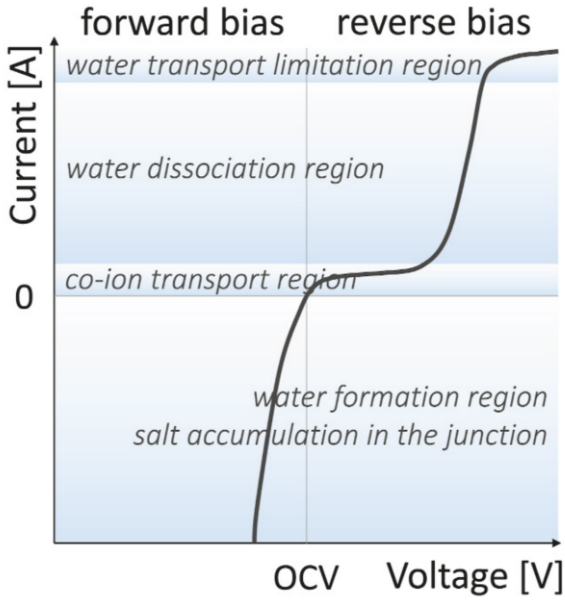

Figure 1.13 Typical current-voltage curve for a bipolar membrane run under forward and reverse bias.[69] Reprinted with permission from Pärnamäe, R.; Mareev, S.; Nikonenko, V.; Melnikov, S.; Sheldeshov, N.; Zabolotskii, V.; Hamelers, H. V. M.; Tedesco, M. *J. Memb. Sci.* 2021, *617*. https://doi.org/10.1016/j.memsci.2020.118538. Copyright 2021 Elsevier.

1.5.2. Electrochemical Impedance Spectroscopy

Electrochemical impedance spectroscopy (EIS) is useful for understanding the properties of bulk materials and interfaces. A DC current or potential is applied in combination with an AC component. An AC response is measured which has varied from the input signal in amplitude and phase shift. The frequency of the AC component ranges from approximately mHz to MHz. As frequency changes, processes which occur at varying timescales are able to be characterized. EIS data can be visualized in terms of real and imaginary impedance, the phase angle and frequency. Data is most often shown in the form of a Nyquist plot which plots real impedance, Re(Z'), on the x-axis, and negative imaginary impedance, -Im(Z"), on the y-axis. Data can also be visualized using Bode plots which plot phase angle and real impedance vs. frequency.

Data is frequently analyzed by fitting these plots to equivalent electrical circuits. A common circuit is a Randles circuit, shown in figure 1.14, which consists of a resistor in series with a capacitor and second resistor in parallel. Individual components in an equivalent circuit refer to specific bulk materials or interfaces within a cell allowing individual processes and interfaces to be differentiated. Randles circuits may be used to describe the ohmic resistance of a cell and a single charge transfer process. However, often features of the anode and cathode of a cell may overlap into a single semicircle. A constant phase element may be used in a place of a capacitor in equivalent EIS circuits. The constant phase element (Q or CPE) is used to describe a non-ideal capacitor which presents as a depressed semi-circle in the Nyquist plot.[107] A common cause of non-ideal behaviour is roughness of the electrode.

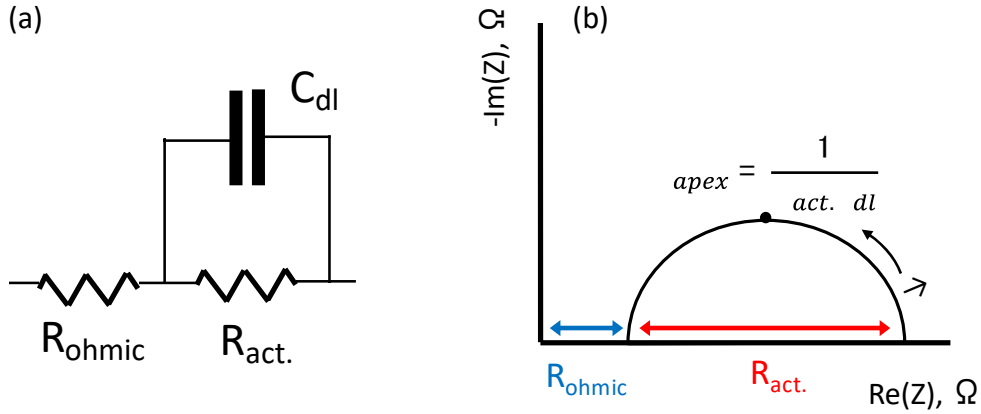

Figure 1.14 **(a) Common equivalent circuit used in electrochemical impedance spectroscopy, Randles circuit. Ohmic resistance, R_{ohmic}, is in series with activation resistance, $R_{act.}$, and double layer capacitance, C_{dl}. (b) Nyquist plot showing Randles circuit shown with corresponding resistances and double-layer capacitance as it related to the apex frequency, ω_{apex}, and activation resistance. The x-axis real impedance, the y-axis is negative imaginary imedance.**

For water electrolyzers EIS is used primarily to characterize the ohmic losses of the cell, electrode kinetics, and mass transport processes.[108] Ohmic losses are found by determining the high frequency resistance (HFR) or high frequency intercept. This is the point at which the data crosses the x-axis at high frequency and is a measure of ohmic resistance across the cell. As such, changes to the high frequency intercept can be

interpreted as changes to the membrane or ionomer ion conductivity, the electrical conductivity of the porous transport layers, or contact resistance between any two components. The activation resistance or charge transfer resistance is measured from the diameter of the semicircle of the Nyquist plot. This resistance describes the performance of the catalyst layer. At low DC voltages the charge transfer resistances are infinite and the Nyquist plot resembles that of a capacitor. As DC voltage is increased the charge transfer resistances decrease with ohmic losses dominating the measured impedance.[109]

Impedance spectra of BPMs are more complicated as an extra interface exists at the BPM junction. Besides the electron transfer reactions at electrodes, water dissociation is also occurring at this interface. Initial modeling of the AC impedance response of BPMs was limited to salt ions and did not properly take the water splitting reaction into account.[110] Alcaraz et al. showed that EIS could be used to determine characteristics of the BPM junction such as the dielectric constant and the structure of the interfacial layer.[111] Subsequent work by Alcaraz, Holdik, and others have been able to estimate the width of the space charge region in the BPM under reverse-bias polarization. [112,113]

Yan et al. used EIS to explore the relationship between the electric field and catalysts in the interfacial layer in enhancing the water dissociation reaction in BPMs. In this work, a resistor and capacitor in parallel were used to model the high frequency feature which represented the water dissociation reaction. The low frequency feature was ascribed to the diffusion of protons from the water dissociation reaction. This was modeled using a Gerischer element from which the water dissociation rate constant was measured.[114]

Blommaert et al. compared EIS spectra of BPMs in different salt solutions, specifically in the absence and presence of co-ions. In their work, a high frequency feature was also attributed to the water dissociation reaction. However, the low frequency feature was fit to a resistor and capacitor in parallel and attributed to the diffusional boundary layer at the membrane|solution interface. This was shown by the absence and presence of this feature in the absence and presence of co-ions in the anodic solution.[115]

1.5.3. UV/Vis Reflectance Spectroscopy

UV/Vis reflectance spectroscopy was used to detect a color change in an indicating anion exchange membrane in chapter 4 of this thesis. This technique uses a beam of light generated by halogen and deuterium lamps emitted from a probe which interacts with the sample. The light reflected is adsorbed by detectors on the probe and the absorbance or reflectance of the sample as function of wavelength is plotted.

1.5.4. Membrane Permselectivity

Membrane permselectivity describes the ability of an ion exchange membrane to transport certain ions while blocking those of a different charge or valence.[116] This thesis focuses on permselectivity as the capacity of an ion exchange membrane to block the transport of co-ions, i.e. cations in the case of PEM/CEMs, and anions in the case of AEMs. The permselectivity of an IEM results from an electric potential at the membrane|solution interfaces known as the Donnan potential, φ_{Don}, as shown in equation 10.[117] This potential is the difference between the membrane, φ^m, and solution, φ^s, potentials. In equation 10, R is the ideal gas constant, T the temperature, z_i, the valence of ion, i, and a^s and a^m are the activities of the species in the solution and membrane, respectively. The apparent membrane permselectivity data for monopolar membranes is presented in this thesis. The apparent membrane permselectivity differs from the true membrane permselectivity as it does not account for water transport through the membrane.[118]

$$(10) \quad \varphi_{Don} = \varphi^m - \varphi^s = \frac{RT}{z_i F} \ln \frac{a_i^s}{a_i^m}$$

1.6. Thesis Scope

The following chapters of this thesis explore the performance of novel hydrocarbon ion exchange membranes in electrochemical devices, the primary focus

being hydrogen generation from liquid water. The polymers used in this thesis are compared to current state-of-the-art commercial polymers. Device performance is related to the membranes physical and chemical properties which in turn relate to the chemical structure. Electrochemical characterization is the primary tool for assessing device performance and gaining insight into the various processes occurring in each device. The most common two methods in thesis being polarization, or current-voltage, curves and electrochemical impedance spectroscopy (EIS). A recurring theme through this work is cell fabrication, spanning from assembling zero-gap water electrolysis cell systems, to membrane-electrode assemblies (MEA), and creation of bipolar membranes from two monopolar polymer materials.

In chapter two, two monopolar ion exchange membranes, one proton exchange membrane (PEM), one anion exchange membrane (AEM), are used in water electrolysis cells and compared to commercially available membranes. Cell components such as bipolar plates and porous transport layers, as well as general cell construction, is found to have a large impact on performance. First, sulfonated poly(arylene) ether (SPAE) is compared to the widely used perfluorinated PEM, Nafion, using polarization curves and EIS. SPAE performs poorly due to a combination of incompatible ionomer in the catalyst layer and highly resistive hardware. Second, a class of poly(arylimidazolium)s is used in an AEM-WE cell fed with highly caustic electrolyte. The poly(arylimidazolium)s are found to survive five times longer than a commercially available AEM in a durability test. This work highlights the stability of sterically hindered imidazoliums in basic solution.

In chapter three, the fabrication of novel bipolar membranes (BPM) is explored with specific emphasis on the BPM junction. Water dissociates into H^+ and OH^- ions at junction, where the AEM and PEM (also referred to as cation exchange membrane (CEM) in this context) are in contact. The performance of BPMs using different junction materials and morphologies is determined using polarization curves. A high surface area junction which includes a water dissociation catalyst is found to outperform a commercially available BPM.

Chapter four continues to explore BPMs but in terms of bulk AEM and CEM layers. The thicknesses of bulk layers are varied in a series of BPMs. The trends seen in polarization curves are attributed to differences in co-ion leakage currents which can be explained by the polymers permselectivity. Additionally, a novel spectroelectrochemical approach is utilized to confirm water dissociation at low cross-membrane potentials. EIS is used to confirm the onset of co-ion leakage.

Conclusions and future directions are given in Chapter 5. As a whole, this work highlights promising novel hydrocarbon PEMs, which rival perfluoronated materials, and novel AEMs, which possess excellent stability in base. Catalyst layer development for AEM-WE and PEM-WE is necessary for improved MEA fabrication as is continued polymer development. For BPMs, further development of interfacial layer fabrication is needed for improved performance.

Chapter 2.

Water Electrolysis Using Hydrocarbon Ion Exchange Materials in Mono-pH Systems

2.1. Proton Exchange Membrane Water Electrolysis With Sulfonated poly(arylene ether), SPAE

2.1.1. Introduction

Generation of hydrogen through electrochemical means is a necessary component for adoption of the hydrogen economy. Proton exchange membranes (PEM) have been well studied as a replacement to traditional alkaline technology which consists of two electrodes separated by a liquid electrolyte and porous diaphragm. Though it is technologically mature and widely employed, traditional alkaline water electrolysis has many shortcomings. The use of a liquid electrolyte leads to high ohmic losses and limits operation to low current densities (<0.5 A cm^{-2}). Additionally, liquid electrolyte hampers the system's ability to rapidly cycle current density, thus making it difficult to pair with intermittent electricity from renewable sources.[12] PEM water electrolysis offers solutions to these problems by using a thin, solid polymer electrolyte which conducts H^+ ions.

The current state-of-the-art PEM water electrolysis systems employ heavily fluorinated materials, namely Nafion^{TM} (DuPont). These materials show high chemical and oxidative stability, excellent mechanical properties, and high proton conductivities. Some disadvantages of using perfluorosulfonic acids like Nafion are that these polymers are expensive and pose environmental issues .[12,26] To remedy this, there has been significant interest in developing hydrocarbon-based PEM materials. Many sulfonated derivatives of poly(arylene ether sulfone)s have been reported in literature but often sacrifice mechanical and chemical stability for proton conductivity.[119–121]

The membrane studied in this research is a sulfonated poly(arylene ether), SPAE, shown in Figure 2.1.[122] SPAE was synthesized in three molecular weights (MW) of 376500 Da, 280,000 Da, and 110,500 Da, referred to as SPAE-H, SPAE-M, and SPAE-L,

respectively, with SPAE-H showing exhibiting the most promising physical characteristics.

Table 2-1 shows the ion exchange capacity (IEC), water uptake, hydration number (λ), and dimensional stability of SPAE and Nafion 211. SPAE-H shows similar dimensional stability to Nafion even though it has a higher water uptake. As Mw increases so does the degree of polymer entanglement, explaining why higher molecular weights correspond to less swelling. Besides chain entanglement, swelling is also decreased by utilizing a multiphenylated backbone which has been shown to increase free volume in the polymer thus creating space for increased water sorption.[123] All SPAE membranes exhibited higher proton conductivities (207-242 mS cm^{-1}) than N211 (115 mS cm^{-1}) at 95% RH as shown in figure 2.2. This is likely a result of the high IEC and water uptake of the SPAE membranes compared to Nafion. The oxidative stability of SPAE was determined using Fenton's reagent (3% H_2O_2 containing 2ppm $FeSO_4$) at 80 °C with results shown in table 2-2. The addition of a trifuoromethyl group in the aromatic ring ortho to each ether linkage is thought to minimize oxidative attack of the polymer chain compared to fully hydrocarbon backbone.[120,124] The oxidative stability of SPAE is lower than that of Nafion, especially for lower MW SPAE. This is likely due to the higher water uptake which leads to higher diffusion of radical species into the polymer matrix.

Given the high dimensional stability of hydrated SPAE-H and its impressive conductivity of 95% RH compared to that of Nafion 211, SPAE-H was chosen for study in a water electrolysis cell.

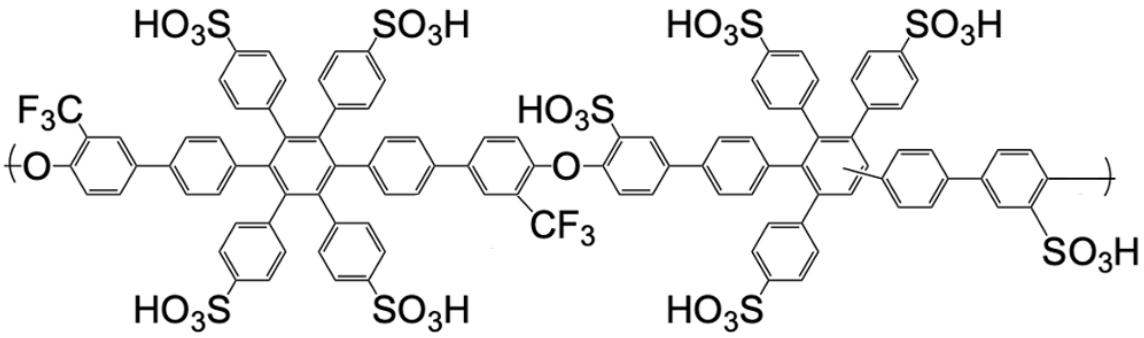

Figure 2.1 Structure of sulfonated poly(arylene ether) (SPAE) in its acid form.

Table 2-1 Ion exchange capacity (IEC), water sorption, and dimensional stability of sulfonated poly(arylene ether) (SPAE)

Sample	IEC[a] (titr.)	Thickness (um)[b]	Water uptake[c]	λ[c]	△l (%)[d]	△T (%)[d]	VU (%)[e]
SPAE-H	3.27	41	84	16	15	17	56
SPAE-M	3.48	20	114	21	20	35	94
SPAE-L	3.30	29	146	27	41	53	216
Nafion 211	0.91	25	30	19	15	20	62

[a] IEC determined by acid-base titration.

[b] Initial dry membrane thickness.

[c] 80 °C in water.

[d] Change in film length (△l) and thickness (△T) at 80 °C in water.

[e] Volume swelling at 80 °C in water.

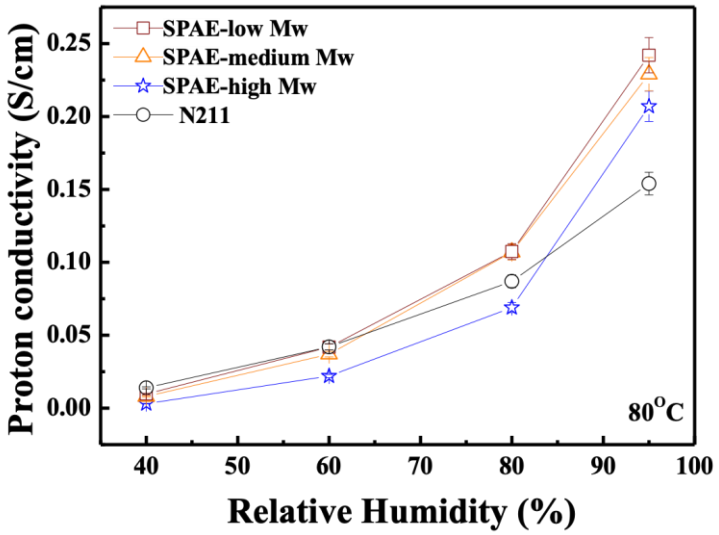

Figure 2.2 **Proton conductivity of sulfonated poly(arylene ether) (SPAE) of various molecular weights and Nafion™ 211 as a function of relative humidity at 80°C. Figure prepared by Dr. Hsu-Feng Lee.**

Table 2-2 **Oxidative stability of sulfonated poly(arylene ether) (SPAE) of various molecular weights and Nafion™ 211.**

Sample	τ_1[a]		τ_2[b]
	Residual weight (%)	Residual Mw (%)	(hr)
SPAE-H	99%	90	33
SPAE-M	95%	86	24
SPAE-L	93%	82	5.5
Nafion 211	99%	-	>50

[a] After heating in Fenton reagent (FeSO4 (2 ppm) in 3% H2O2 solution) at 80 OC for 1 h.

[b] τ_2 refers to the time when the membrane dissolved completely at 80 °C (replaced the fresh Fenton reagent every 12hrs).

2.1.2. Experimental

MEA Preparation and Cell Construction

Membrane-electrode assemblies (MEA) were prepared by hand spraying catalyst inks onto an SPAE membrane, 27 μm thick, and a Nafion™ 115 membrane, 125 μm thick. Catalyst inks contained 2.3% solids, 25% of which was Nafion™ ionomer, suspended in a 1:1 water: isopropyl alcohol mixture. These MEAs were compared to a

commercially available MEA (Greenerity® GmbH, E400) utilizing a Nafion™ 115 membrane. The catalyst loadings for SPAE were 0.80 mg cm^{-2} of Pt and 2.54 mg cm^{-2} of Ir black for the cathode and anode respectively. The loadings for the Nafion™ 115 reference were similar, 0.83 mg cm^{-2} of Pt and 2.78 mg cm^{-2} of Ir black for the cathode and anode respectively.

Nafion™ 115 and Greenerity® MEAs were tested on the same cell hardware consisting of titanium endplates and bipolar plates. The SPAE MEA was tested in a cell consisting of titanium endplates, and titanium bipolar plates which had been sanded and coated with gold using sputtering deposition. Porous transport layers (PTLs) (Bekaert) were used to facilitate gas removal from the catalyst layer. The PTL used for Nafion™ 115 and the Greenerity® reference was pre-coated with platinum, while the PTLs used in the SPAE cell were coated with gold using sputtering deposition.

Ink preparation was a joint effort by Amelia Hohenadel and Thulile Khoza. Hand spraying was done by Dr. Thulile Khoza. Gold sputtering was performed by Dr. Alejandro Oyarce. Sulfonated poly(arylene ether) (SPAE) was provided by Dr. Hsu-Feng Lee. Ion exchange capacity (IEC), water sorption, dimensional stability, and conductivity of SPAE was determined by Dr. Hsu-Feng Lee.

Electrochemical Characterization

Both cells were conditioned overnight at 40 °C running DI water to the anode and cathode at a rate of 0.2 liters per minute. Steady state polarization curves were taken at 60 °C, 70 °C, and 80 °C. A current of 1 A cm^{-2} was held for 10 minutes before increasing the temperature. Polarization curves presented in this work have been iR corrected using the high frequency intercept (HFR) as determined by electrochemical impedance spectroscopy (EIS) to account for differences in cell thickness and hardware. EIS was taken by scanning 50 kHz to 100 mHz at various current densities. Pre-heated DI water was continuously run through the anode and cathode of the cell at rate of 0.2 liters per minute for all characterization.

2.1.3. Results and Discussion

Polarization curves, shown in Figure 2.3 (A), demonstrate that although SPAE functions in the water electrolysis system, voltages are significantly higher than the Nafion and Greenerity references. SPAE-H has a voltage of 1.725 V at 1 A cm^{-2} compared to 1.623 V for Nafion 115 and 1.568 V at 70 °C. These high voltages are particularly unusual given the thickness of SPAE which is approximately 100 μm less than the Nafion and Greenerity MEAs. These very high voltages likely originate from differences in cell hardware. The bipolar plates used for characterizing the SPAE were made of titanium which had formed of a resistive passivated TiO_x layer on the surface. This is a well-known occurrence in PEM water electrolysis for titanium bipolar plates and PTLs, particularly on the anode side.[125] The gold coating applied to the sanded plate does not appear to have adequately increased conductivity. A photograph of the cell after disassembly, Figure 2.4, shows that this gold coating was beginning to peel away from the plate after a single use.

Also evident from the polarization curves are losses occurring in the mass transport region for SPAE at current densities above approximately 1.5 A cm^{-2}. Mass transport losses in a water electrolyzer typically occur when reactant water is blocked from reaching active sites due to increased reaction rate and from large bubbles which may reduce catalyst utilization.[12] These losses are reversible and only occur at high voltages. Comparison of forward and backward polarization curves for SPAE, shown in figure 2.3 (B) suggest irreversible losses occur at high voltages. Although mass transport losses may account for some of the overpotential at high current densities, it seems that another irreversible process is occurring. This could be continued passivation of the titanium hardware or delamination of the catalyst layers, which was observed when dismantling the cell, shown in figure 2.4. SPAE showed in-plane dimensional stability similar to that of Nafion, as shown in Table 2-1. This suggests that the poor adhesion between the catalyst layer and membrane resulted from incompatibility between the Nafion ionomer and hydrocarbon membrane rather than a difference in swelling between bulk membrane and ionomer in the catalyst layer.

Characterization of the cells by EIS confirms that the hardware used for the SPAE membrane is significantly more resistive than the hardware used for the Greenerity and Nafion membranes. This is clear from comparison of the high frequency resistance (HFR)

represented by circuit element R1. Nyquist plots comparing SPAE, Nafion and Greenerity membranes at 60 °C, 70 °C, and 80 °C are shown in figures 2.6 to 2.8. Data was fit to equivalent circuits shown in figure 2.5 with values for each circuit element shown in tables 2-3 to 2-5. Nyquist plots for Nafion exhibit two overlapping semi-circles and is best fit with an equivalent circuit which contains two constant phase elements and three resistors. Rozain et al. showed that at intermediate DC voltages, two semicircles may be visible in the Nyquist plot of a PEM water electrolyzer.[109] Although it seems intuitive to assign one semicircle to each the cathodic and anodic reaction, a comparison of the OER and HER time constants in this work indicated otherwise. The HER charge transfer process contributes negligibly to the plot while the two overlapping semicircles observed represents two single-electron processes associated with the OER. This may be the reason two semicircles are observed in the Nyquist plot of the Nafion cell. The difference in Ir-loading at the anode could explain why this is not seen for the SPAE cell even though both MEAs used the same ink formulation and spray coating technique. The ohmic resistance of the cells, measured as circuit element R1, decreases with increasing temperature. The Greenerity MEA exhibits the lowest activation resistance, measured as R2 for Greenerity and SPAE and R2+R3 for Nafion.

Further investigation with EIS shows SPAE deviates from the ideal semi-circle Nyqust plot at larger voltages, shown in figure 2.9. Unlike the plot of Nafion which shows a small second semi-circle at high frequencies, this deviation occurs in the low frequency region. This suggests slow processes, such as mass transport limitations, are responsible. However, from the polarization curve shown in figure 2.3 (B) it is assumed that these are irreversible processes such as the delamination of the catalyst layer and resulting interfacial resistance, and continued passivation of the Ti bipolar plates and PTLs.

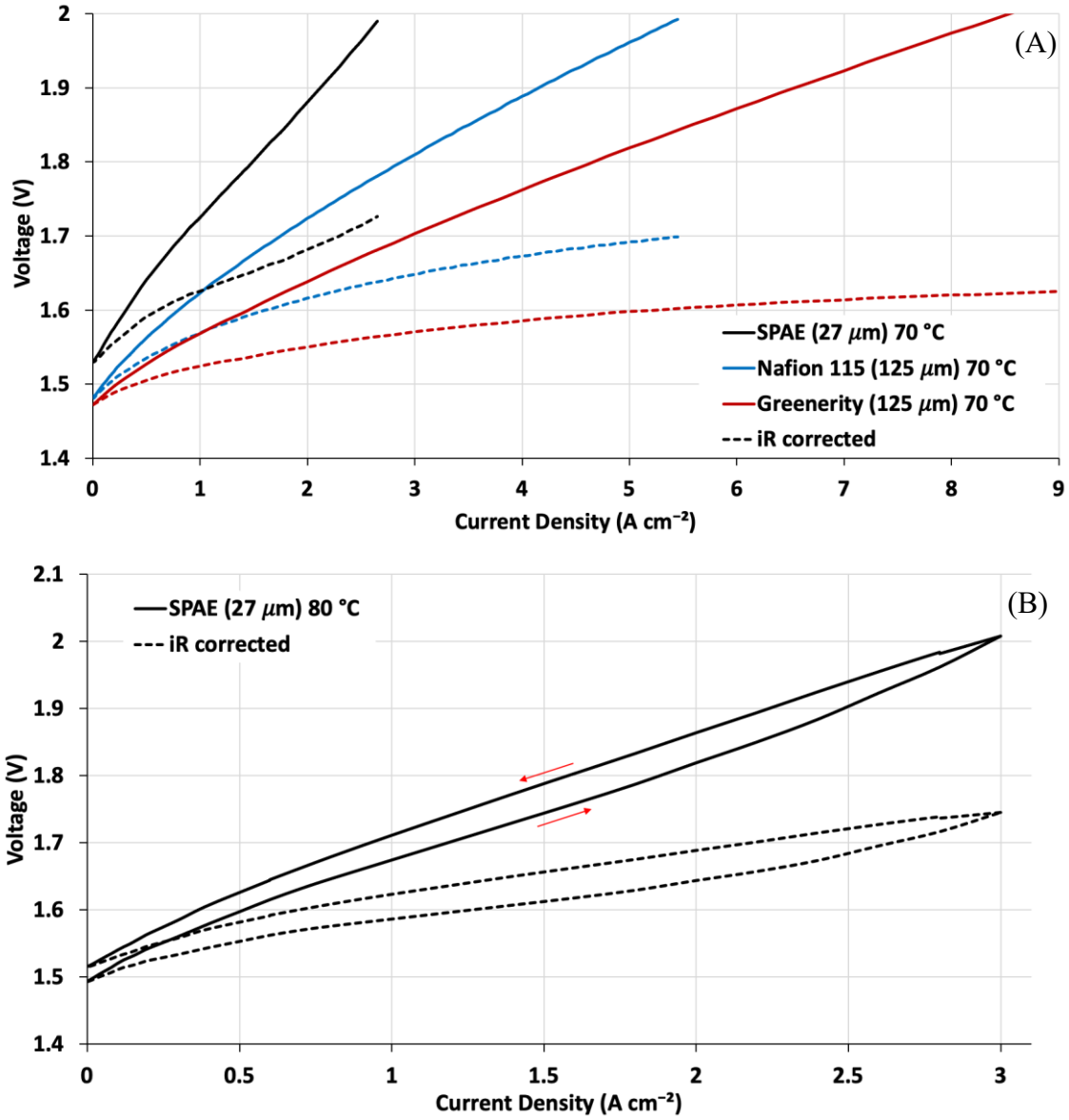

Figure 2.3 **(A) Polarization curves (forward scans) comparing sulfonated poly(arylene ether) (SPAE), Nafion™ 115, and Greenerity® MEAs at 70 °C. (B) Polarization curve of SPAE at 80 °C showing the forward and backward scans. Dashed lines represent curves which have been iR-corrected using the high-frequency resistance obtained with EIS.**

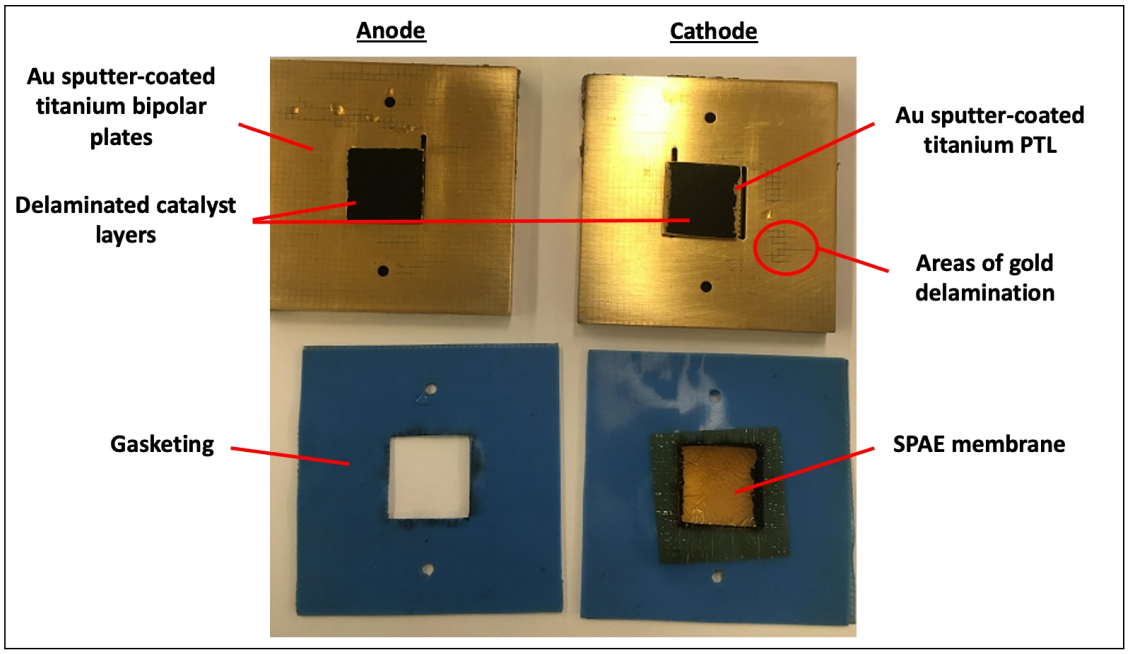

Figure 2.4 **Photograph of disassembled water electrolyzer cell using sulphonated poly(arylene ether) (SPAE). Catalyst layers are completely delaminated from the membrane and adhered to the porous transport layers (PTL). The gold coating on the bipolar plates has begun to delaminate after a single use.**

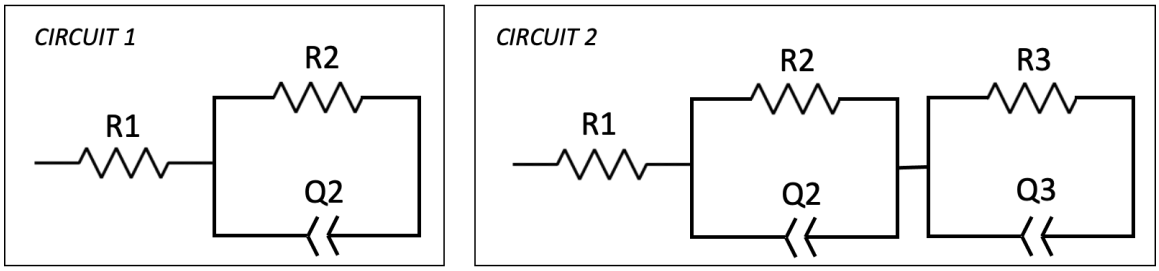

Figure 2.5 **Equivalent circuits used for fitting electrochemical impedance spectroscopy (EIS) data with R representing resistors and Q representing constant phase elements. Circuit 1 is used to fit sulphonated poly(arylene ether) (SPAE) and Greenerity® cells. Circuit 2 was chosen for fitting Nafion™ as it provides a better fit the data.**

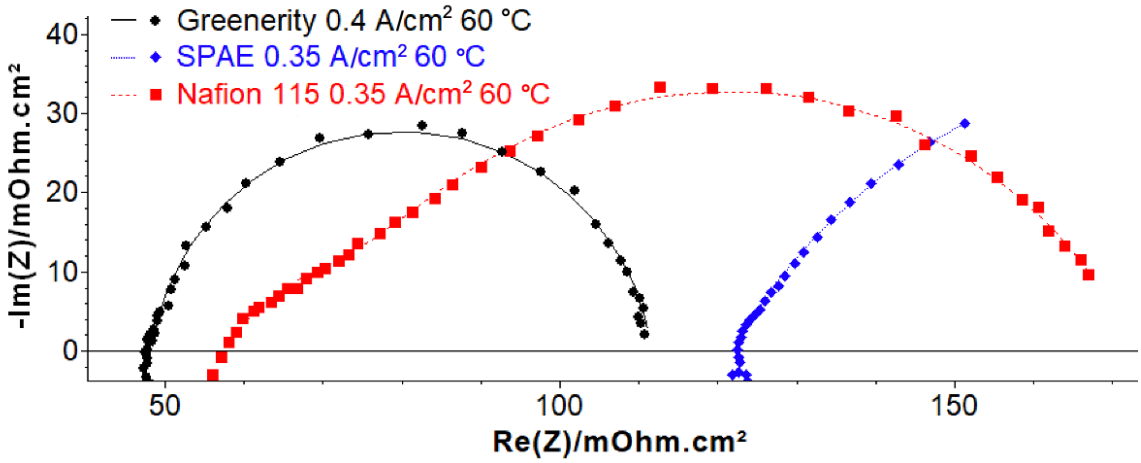

Figure 2.6 **Nyquist plot comparing Greenerity®, sulfonated poly(arylene ether) (SPAE) and Nafion™ 115 at 60 °C. Greenerity® was held at a current density of 0.4 A/cm² while both SPAE and Nafion™ were held at 0.35 A/cm². Dots represent data points and dashed lines represent fitting to an equivilant circuit by EC-Lab Z-fit software.**

Table 2-3 **Circuit element values for the Greenerity®, sulfonated poly(arylene ether) (SPAE), and Nafion™ 115 membranes at 60 °C after fitting EIS data using EC-Lab Z-fit software.**

@ 60 °C	Greenerity @ 0.40 A/cm²	SPAE @ 0.35 A/cm²	Nafion 115 @ 0.35 A/cm²
R1 (mOhm cm²)	48.36	121.85	58.20
Q2 (F s$^{(a-1)}$)	2.931	1.55	0.609
$\alpha 2$	0.918	0.681	0.774
R2 (mOhm cm²)	63.20	124.85	14.415
Q3 (F s$^{(a-1)}$)	-	-	2.526
$\alpha 3$	-	-	0.728
R3 (mOhm cm²)	-	-	100.15
χ^2	2.82 x 10^{-3}	1.97 x 10^{-3}	2.62 x 10^{-3}

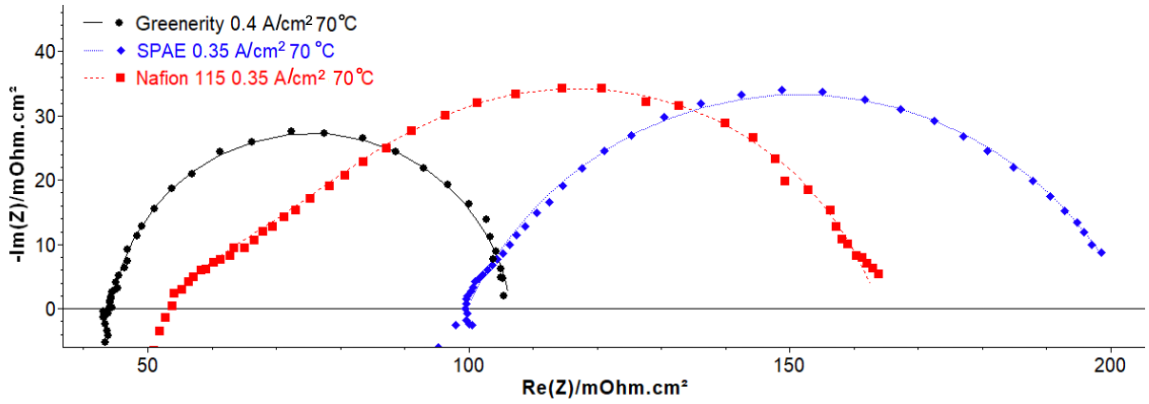

Figure 2.7 **Nyquist plot comparing Greenerity®, sulfonated poly(arylene ether) (SPAE) and Nafion™ 115 at 70 °C. Greenerity® was held at a current density of 0.4 A/cm² while both sulfonated poly(arylene ether) (SPAE) and Nafion™ were held at 0.35 A/cm². Dots represent data points and dashed lines represent fitting to an equivilant circuit by EC-Lab Z-fit software.**

Table 2-4 **Circuit element values for the Greenerity®, sulfonated poly(arylene ether) (SPAE), and Nafion™ 115 membranes at 70 °C after fitting EIS data using EC-Lab Z-fit software.**

@ 70 °C	Greenerity @ 0.40 A/cm²	SPAE @ 0.35 A/cm²	Nafion 115 @ 0.35 A/cm²
R1 (mOhm cm²)	44.23	99.60	54.05
Q2 (F s$^{(a-1)}$)	2.914	1.233	0.444
$\alpha 2$	0.917	0.727	0.828
R2 (mOhm cm²)	62.35	103.7	13.94
Q3 (F s$^{(a-1)}$)	-	-	2.106
$\alpha 3$	-	-	0.728
R3 (mOhm cm²)	-	-	100.15
χ^2	2.24 x 10^{-3}	1.49 x 10^{-3}	6.07 x 10^{-3}

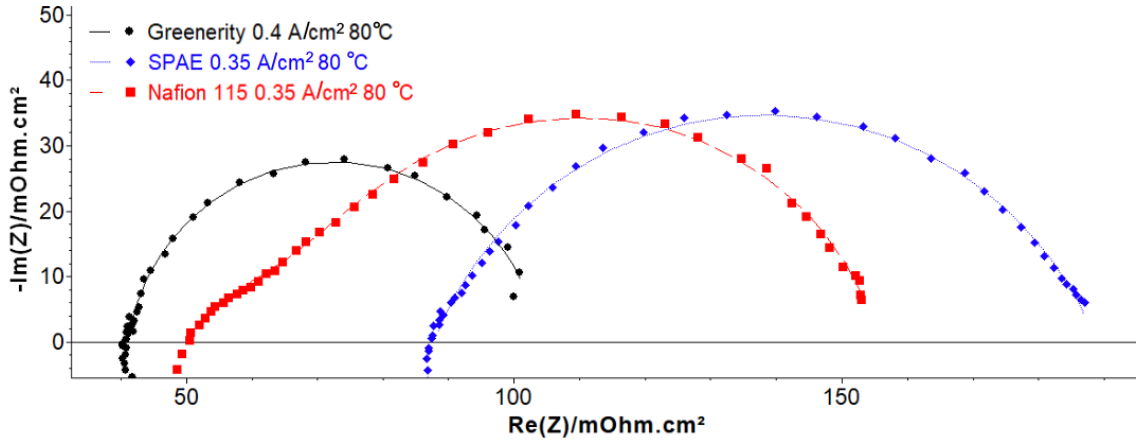

Figure 2.8 **Nyquist plot comparing Greenerity®, sulfonated poly(arylene ether) (SPAE) and Nafion™ 115 at 80 °C. Greenerity® was held at a current density of 0.4 A/cm² while both sulfonated poly(arylene ether) (SPAE) and Nafion™ were held at 0.35 A/cm². Dots represent data points and dashed lines represent fitting to an equivilant circuit by EC-Lab Z-fit software.**

Table 2-5 **Circuit element values for the Greenerity®, sulfonated poly(arylene ether) (SPAE), and Nafion™ 115 membranes at 80 °C after fitting EIS data using EC-Lab Z-fit software.**

@ 80 °C	Greenerity	SPAE	Nafion 115
R1 (mOhm cm²)	41.09	87.60	50.45
Q2 (F s$^{(a-1)}$)	2.904	1.107	1.339
$\alpha 2$	0.919	0.766	0.694
R2 (mOhm cm²)	62.7	101.3	18.66
Q3 (F s$^{(a-1)}$)	-	-	1.872
$\alpha 3$	-	-	0.828
R3 (mOhm cm²)	-	-	86.75
χ^2	4.15 x 10^{-3}	2.00 x 10^{-3}	2.20 x 10^{-3}

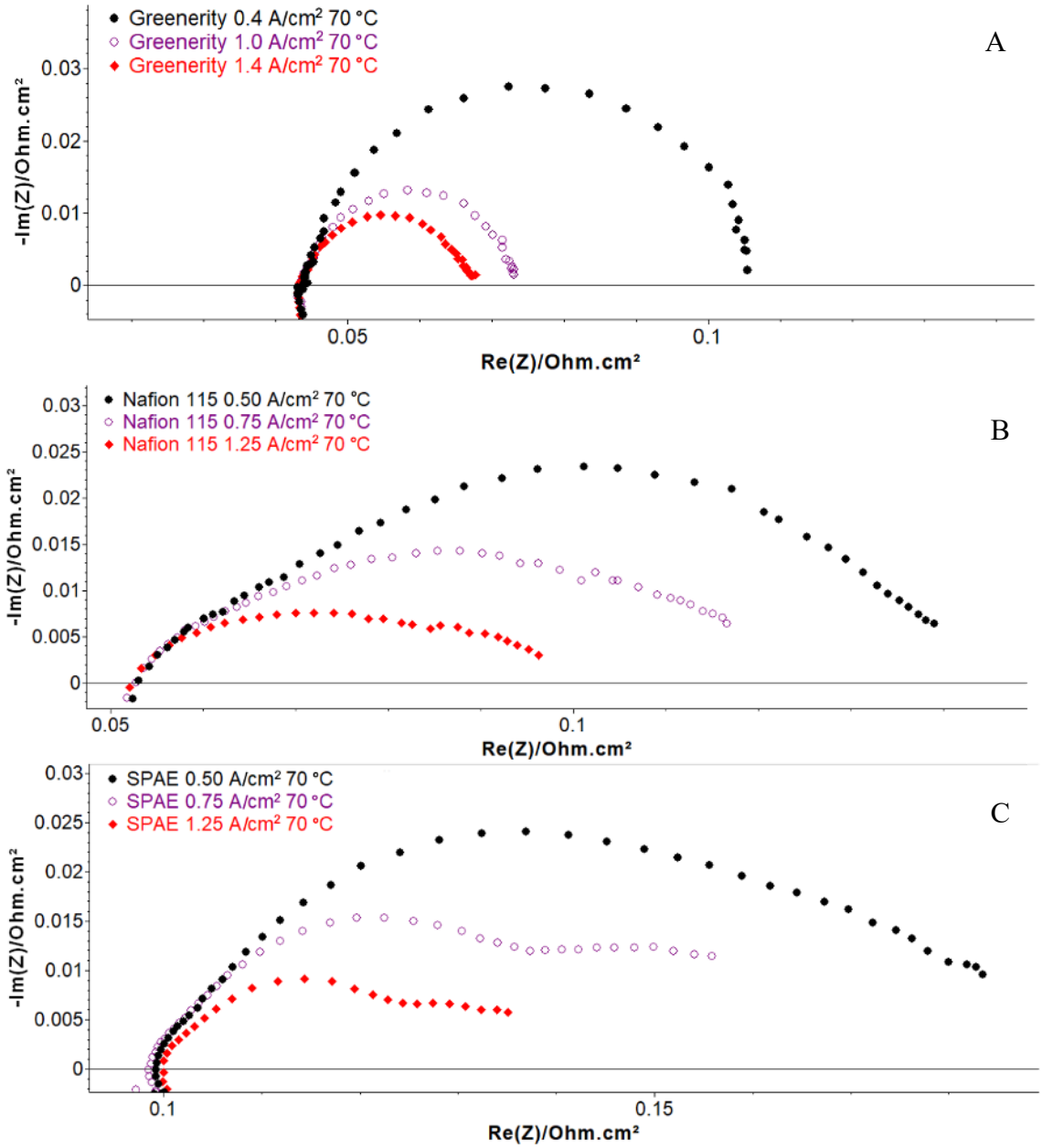

Figure 2.9 Nyquist plots comparing Greenerity®, sulfonated poly(arylene ether) (SPAE) and Nafion™ 115 at various DC current densities.

Conclusion

In an initial study of sulfonated poly(arylene ether) (SPAE) it is found that the membrane functions well in a water electrolyzer up to 80 °C, although performance is poorer than that of Nafion. Inconsistencies in hardware, catalyst loading, and membrane thickness limit the conclusions that can be drawn from this study. A high ohmic

resistance likely results from the hardware used for the SPAE cell highlighting the importance of engineering zero-gap water electrolysis cells and optimizing all components. In addition, it was found that a spray coated catalyst layer containing Nafion does not adhere well to the SPAE membrane causing irreversible losses at high current densities. To better understand how SPAE function in a water electrolyzer further studies utilizing SPAE as both the ionomer and membrane are necessary.

2.2. Anion Exchange Membrane Water Electrolysis with Poly(bis-arylimidazoliums)

2.2.1. Introduction

Anion exchange membranes (AEM) have been studied recently as an alternative to acidic proton exchange membranes. As solid electrolytes, these membranes have many of the same advantages as proton exchange membranes (PEM) but with reactions occurring in basic rather than acidic media. This allows for the use of abundant, inexpensive catalysts.[126] However, anion exchange materials have historically been plagued by instability and low ionic conductivity.[127] Because of this, continuing research has been necessary for commercialization of alkaline water electrolyzers and fuel cells.

Of the many organic cations studied, imidazoliums are particularly attractive because of their ease of synthesis and enhanced stabilization due to electron delocalization.[128] DFT studies have also suggested that imidazoliums are more stable than benzimdazoliums.[129] Imidazolium ions are prone to degradation in the presence of base, but these degradation pathways can be suppressed through selection of suitable substituents. Significant progress has been made studying poly(arylimidazoliums)

beginning with model compound studies of sterically protected imidazolium groups.[62] Through a combination of degradation studies and density functional theory (DFT) calculations, it was found that imidazolium groups protected by methyl substituents on an adjacent mesityl group showed the highest stability in alkaline conditions with degradation occurring predominately through demethylation of the imidazolium cation. It was reasoned that the methyl substituents provided adequate steric hindrance to protect the C2 position of the imidazole while increasing stabilization through electron donation. A polymer based on this model compound, HMT-PMPI, shown in figure 2.10 (A), was synthesized but it had low molecular weight (67 kDa) and was soluble in water at 80°C. This work was continued with the study of model compounds and polymers with longer alkyl chains attached to the N1/N3 positions of the imidazolium cation which has previously been shown to inhibit demethylation.[62,128] However, longer alkyl chains would increase the mass of each repeat unit, lowering the ion exchange capacity, and thus the polymers conductivity. To maintain high ion exchange capacity, bis-imidazolium model compounds and polymers, shown in figure 2.10 (B), were studied.[43]

Figure 2.11 shows conductivity and stability data for the polymers studied. Generally speaking, as alkyl chain length increases, stability increases and IEC decreases. The poly(bis-arylimidazolium) with methyl groups at both the N1 and N3 positions (PAImMM) exhibited the highest conductivity, a result of its high IEC, but very low stability with a calculated half-life of only 400 hours in 10 M KOH at 80 °C. DFT calculations of model compounds show that bis-imidazolium ions have a higher electrostatic potential than their single imidazolium counterparts, and thus more attraction between the cations and hydroxide anions exists leading to increased hydroxide attack.[43] The most stable polymer was PAImBB, which had butyl groups at both N1 and N3 positions, with a half-life of 8560 hours. Because of its impressive stability, PAImBB was characterized in a fuel cell obtaining a maximum power density of 250 mW cm^{-2} at 70°C. PAImBB was also characterized in water electrolysis cell run with 6 M KOH solution and compared to PAImEE, which has ethyl groups at both N1 and N3, under the same conditions.

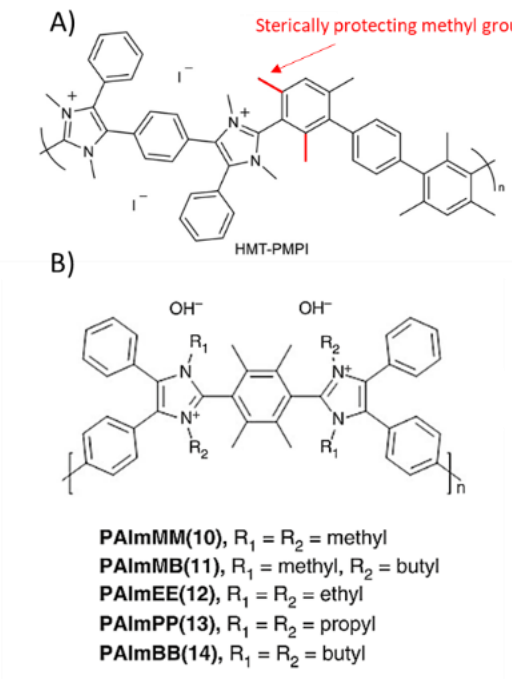

Figure 2.10 **Structures of (A) hexamethyl p-terphenyl poly(arylene-imidazolium) (HMT-PMPI) from Ref [61] highlighting the methyl groups sterically protecting the C2 position of the imidazolium ion and (B) poly(bis-arylimidazoliums) (PAImXY) where X and Y represent alkyl chains R1 and R2 from Ref [42].**

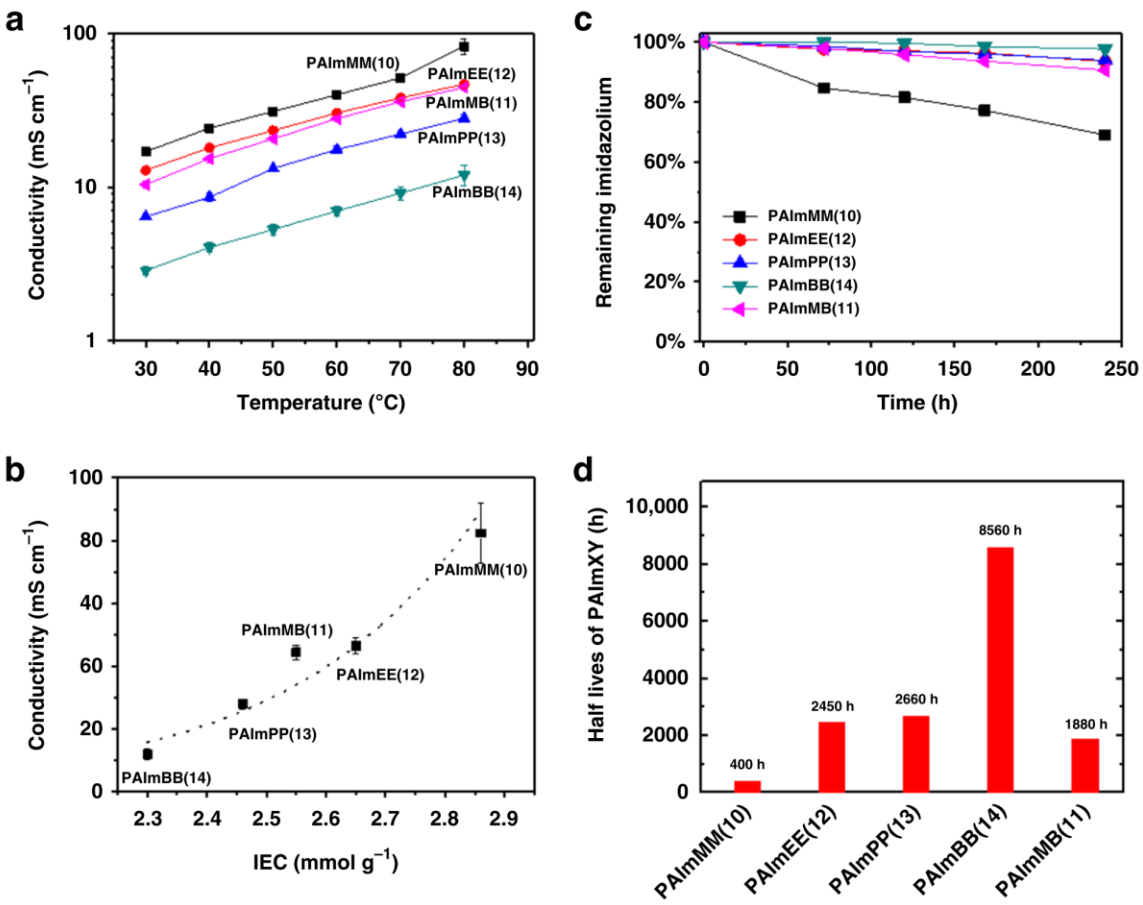

Figure 2.11 **Properties of poly(bis-arylimidazoliums) (PAImXY) where X and Y represent alkyl chains R1 and R2 at the N1 and N3 positions of the imidazolium. (a) Ionic conductivity in Cl^- form at various temperatures under 95% RH. (b) Ionic conductivity at 80 °C, 95 % RH vs. IEC. (c) Stability of PAImXY to caustic solution after immersion in 10M KOH at 80 °C for 240 h. (d) Calculated half-life. Figures prepared by Dr. Jiantao Fan.**[43]

2.2.2. Experimental

Catalyst-coated membranes were prepared using the poly(bis-arylimidazoliums) as the membrane and as ionomer in the catalyst layer. Platinum on carbon was used as the catalyst at both the anode and cathode (46.4% Pt, Tanaka). Catalyst layers consisted of 15–20% ionomer. Catalyst loadings were as follows: for PAImBB [20 μm], 0.96 and 0.66 mg Pt/cm^2 at the anode and cathode, respectively, for PAImEE, [25 μm] 0.65 and 0.62 mg Pt/cm^2 at the anode and cathode, respectively, and for PAImEE [13 μm], 0.66 and 0.5762 mg Pt/cm^2 at the anode and cathode, respectively. The electrolysis cell consisted

of a membrane-electrode assembly compressed between two titanium bipolar plates having serpentine flow fields. Titanium porous transport layers (Fuel Cell Store) separated the catalyst layers from the flow fields and provided electrical contact, and allowed transport of gasses and liquid. The bipolar plates were housed in titanium hardware equipped with gold current collectors. 6 M KOH was fed to the anode and cathode using peristaltic pumps at a rate of 10.0 mL min^{-1} and recirculated using liquid gas separators. Argon was bubbled through the KOH solution to limit carbonation from ambient air. Electrochemical characterization was performed using a Solartron 1287A potentiostat. Polarization curves were taking by ramping current density at a rate of 5 mA cm^{-2} from 0 to 400 mA cm^{-2}. All poly(bis-arylimidazoliums) were provided by Dr. Jiantao Fan. Conductivity and stability measurements were performed by Dr. Jiantao Fan. Ink preparation, MEA formation, and electrochemical measurements were done by Amelia Hohenadel.

2.2.3. Results and Discussion

In all polarization curves, voltages remained below 2.5 V for current densities up to 400 mA cm^{-2}. Comparison of PAImBB and PAImEE in Figure 2.12 (A) shows slightly higher performance of PAImEE, likely to due to its higher conductivity. Improved performance can be achieved by increasing the operating temperature. Figure 2.12 (B) shows a 0.2 V potential drop from 60 to 80 °C for PAImEE. Stable operation of membranes at temperatures up to 80 °C and under such caustic conditions demonstrates the stability of the poly(bis-imidazoliums).

A PAImEE, 25 μm-thick membrane cell was operated at 60 °C with 6M KOH under 400 mA cm^{-2} for 48 h, as shown in figure 2.12 (C). The break in the cell voltage at 24 hours represents a reconditioning protocol, as trace impurities have been shown to strongly affect the rate of hydrogen evolution[130,131]. After reconditioning, the potential was significantly lowered, followed by a gradual increase due to commencement of poisoning of the electrodes. It is also likely that the degassed KOH solution began to undergo carbonation as it was in contact with the air. Comparatively, commercial FAA run using the same setup under much milder caustic conditions (1 M KOH) and much

lower current density (20 mA cm^{-2}) failed after 9.5 h. The PAImEE cell was eventually shut down, not because of membrane degradation but due to increased resistance of the uncoated titanium bipolar plate, which had undergone severe corrosion under contact with hot caustic solution. Despite this, the potential remained less than 2.6 V after 48 h, showing promising chemical durability of the PAImEE membranes.

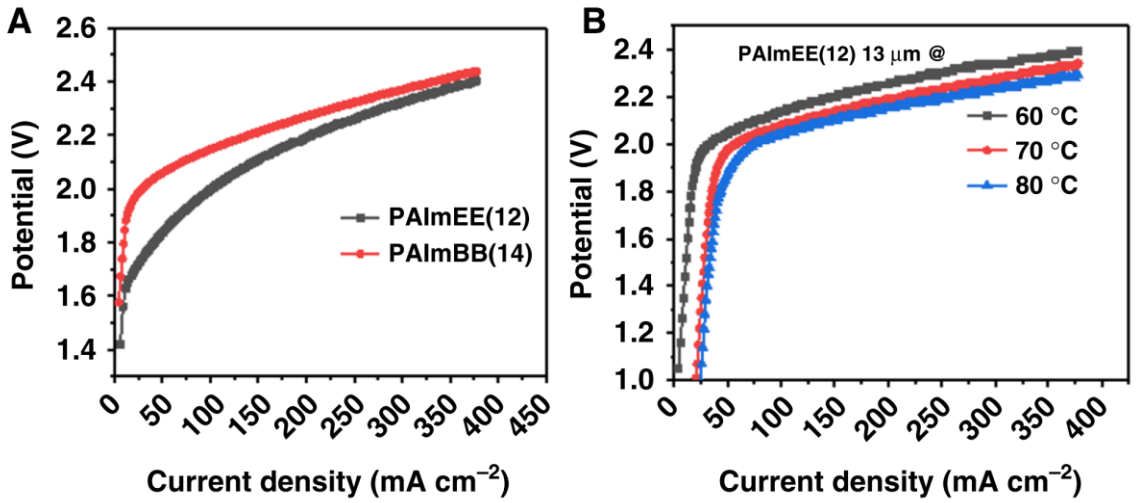

Figure 2.12 **(A) Polarization curves of poly(bis-arylimidazoliums) with ethyl groups at the N1/N3 positions (PAImEE) [25 µm thick] and butyl groups at the N1/N3 positions (PAImBB) [20 µm thick] AEM electrolyzer at 60 °C. (B) Polarization curves of PAImEE [13 µm thick] AEM electrolyzer at 60, 70 and 80 °C in 6M KOH. Figures prepared by Dr. Jiantao Fan.**

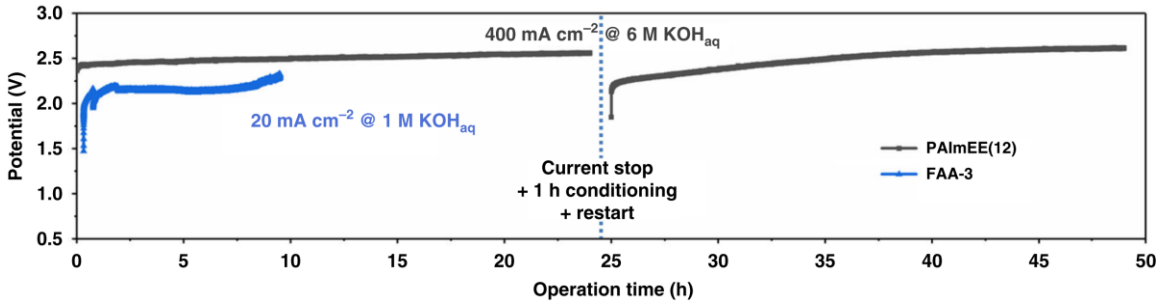

Figure 2.13 **Poly(bis-arylimidazolium) with ethyl groups at the N1/N3 positions (PAImEE) [25 µm] maintained at 400 mA cm^{-2}, and FAA-3 [25 µm] at 20 mA cm^{-2} at 60 °C. The difference in voltage between FAA-3 and PAImEE in can be attributed to the different current densities at which the cell was operated. Figures prepared by Dr. Jiantao Fan.**

2.2.4. Conclusion

Poly(bis-arylimidazoliums) with variable alkyl chain lengths at the N1 and N3 positions represent a class of anion exchange membranes with exceptional stability in base and reasonable conductivities. Such membranes function well in electrochemical devices, notably in water electrolyzers as both the ionomer in the catalyst layer and bulk membrane. These polymers function in devices run at elevated temperature, > 60 °C, and in highly caustic environments, 6 M KOH, for extended periods of time and at current densities of 400 mA cm^{-2}.

Chapter 3.

Electrochemical Characterization of Hydrocarbon Bipolar Membranes with Varying Junction Morphology

3.1. Introduction

Hydrogen gas is a flexible energy carrier with the ability to contribute to multiple sectors.[132] Electrochemical water splitting is a promising method for its production because it allows for the formation of very pure hydrogen gas without contributing to greenhouse gas emissions like other hydrogen production methods do, such as methane reformation.[133] Water electrolysis may be coupled with renewable sources of electricity such as wind and solar, providing fuel with a minimal carbon footprint. Current water electrolysis technologies face obstacles such as high cost, inefficiency, and safety concerns. The most mature electrolytic hydrogen technology uses a caustic electrolyte for ion conduction and the promotion of electrochemical reactions at relatively inexpensive nickel electrodes, where the electrodes are separated by a porous diaphragm.

Solid polymer electrolyte membranes are being investigated as a replacement for caustic solution/porous diaphragm separators as they have the potential to provide physical separation of the anode and cathode at shorter distances and, hence, a lower ionic resistance between the two electrodes.[12] This physical separation also limits mixing of the product gases. In this context, proton exchange membranes (PEM), such as perfluorosulfonic acid (PFSA) ionomer membranes, are being widely studied.[134,135] Although PFSAs are useful in water electrolysis because of their high mechanical strength and high chemical and thermal stability, two problems exist with these systems. First, PFSAs are considered to be expensive, relatively permeable to hydrogen and

oxygen, and their disposal poses potential environmental concerns.[136] Additionally, PEM electrolyzers are acidic in nature which necessitates the use of increasingly expensive, rare platinum-group metals to catalyze the oxygen and hydrogen evolution reactions. Moreover, while the hydrogen evolution reaction is facile in acidic media, the oxygen evolution reaction is relatively sluggish. In order to increase the rate of oxygen evolution, alkaline anion exchange membranes (AEM) are being investigated.[21] In addition to increased oxygen evolution reaction (OER) kinetics, OER can occur on inexpensive catalysts such as nickel in basic conditions. However, the hydrogen evolution reaction is relatively sluggish in caustic media compared to acidic media.[68]

Employment of a single acidic or alkaline membrane limits operation to either low or high pH, respectively, thus limiting the reaction kinetics and electrode materials. By using bipolar membranes (BPM), both AEM and PEM materials may be combined to allow half-cell reactions to take place in acidic and basic conditions. This results in an electrolytic cell that combines the fast kinetics of the hydrogen evolution reaction at low pH with the use of non-noble catalysts and fast kinetics of the oxygen evolution reaction in alkaline conditions.

Bipolar membranes are, in their simplest form, a lamination of an AEM and PEM. Water splitting occurs when the membrane operates under reverse-bias conditions as depicted in Figure 3.1. Under these conditions, a cathodic potential applied to the electrode on the acidic side reduces protons to hydrogen, while an anodic potential applied to the electrode on the alkaline side forms oxygen gas. To maintain electro-neutrality, water dissociates at the PEM|AEM interface, with the protons diffusing through the PEM to the cathode and the hydroxide ions diffusing through the AEM to the anode.[84] A combination of the second Wein effect and catalytic proton- accepting groups such as tertiary amines are reported to account for the fast rate of water dissociation at the interface, which is up to 10^7 times faster than normally associated with the rate of dissociation of bulk water into H^+ and OH^-.[77]

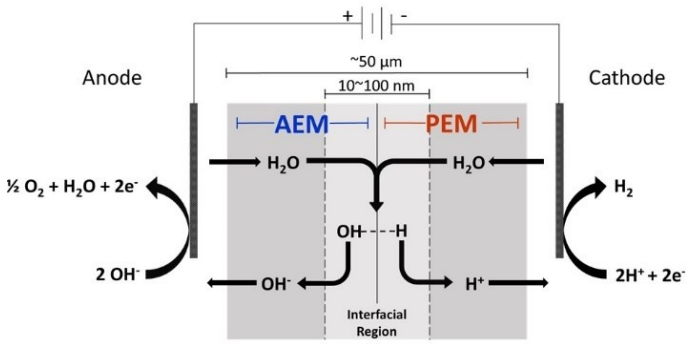

Figure 3.1. Depiction of reverse-bias operation for an electrolytic cell incorporating a bipolar membrane.

The PEM|AEM interface of the BPM is a critical feature of this technology as it is responsible for facilitating the splitting of water into protons and hydroxide ions. From what is known from the literature, the interface must be as thin as possible to maximize the electric field but possess a certain degree of interpenetration of the PEM and AEM polymers in order to necessitate sufficient adhesion between the two membranes.[79] Several studies have shown increased water dissociation efficiency when metal hydroxides, silicon groups, metal alkoxides, and graphene oxide are present at the interface of the PEM and AEM.[82,83,137,138] The increase in efficiency is explained by the ability of these catalysts to participate in protonation and deprotonation reactions and by their hydrophilicity, which increases ion conductivity within the membrane.[84,85]

To further investigate the role of the interfacial layer, four bipolar membranes were fabricated and compared with a commercial Fumasep BPM. Each of the four fabricated BPMs were based on the same bulk AEM and PEM polymer, i.e., hexamethyl-p-terphenyl poly(benzimidazole) (HMT-PMBI) and sulfonated phenylated polyphenylene(biphenyl) (SPPB), respectively.[139,140] BPM I and BPM II were fabricated with dual-fiber electrospun polymer mats using the method reported by Shen et al.[79] In this method, a junction consisting of interwoven fibers of AEM and PEM polymers is formed separate from the bulk regions. The fibers were coated with nanoparticulate $Al(OH)_3$ catalyst. This junction is then placed between precast AEM and PEM and hot-pressed to form a single BPM. This technique creates BPMs with much larger interfacial surface areas and superior adhesion than a simple two-dimensional junction comprised of an AEM and PEM. These two BPMs were compared to two BPMs prepared in the

absence of a dual-fiber electrospun polymer mat. For BPM III, $Al(OH)_3$ catalyst was incorporated at the AEM|PEM interface. BPM IV was simply comprised of an AEM and PEM and contained no $Al(OH)_3$ catalyst. Figure 3.2 shows the structures of the polymers used. A schematic of the four bipolar membranes is shown in Figure 3.3. Based on previous literature, it was found that BPMs comprising 3D dual-fiber electrospun junctions yield higher current densities than those prepared with a 2D junction.[79] This work studies whether this observation held with other membrane types, namely, highly arylated PEMs and AEMs, and whether the inclusion of aluminum hydroxide decrease the overpotentials for water dissociation. The results confirm these hypotheses and reveal an interesting dependence of the interfacial layer on co- ion leakage under open circuit conditions.

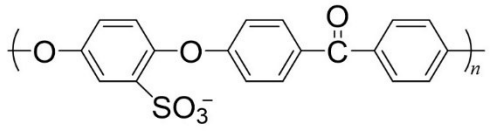

Sulfonated poly(ether ether ketone)
SPEEK

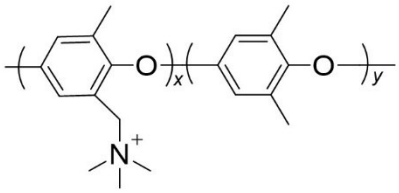

Quaternized poly(phenylene oxide)
QPPO

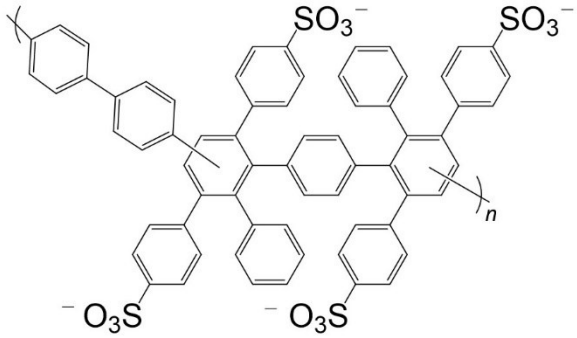

Sulfonated phenylated polyphenylene (biphenyl)
SPPB

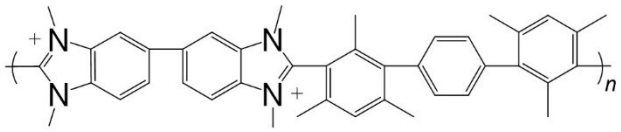

Hexamethyl-p-terphenyl poly(benzimidazole)
HMT-PMBI

Figure 3.2 Structures of PEMs, SPEEK and SPPB, and AEMS, QPPO and HMT-PMBI.

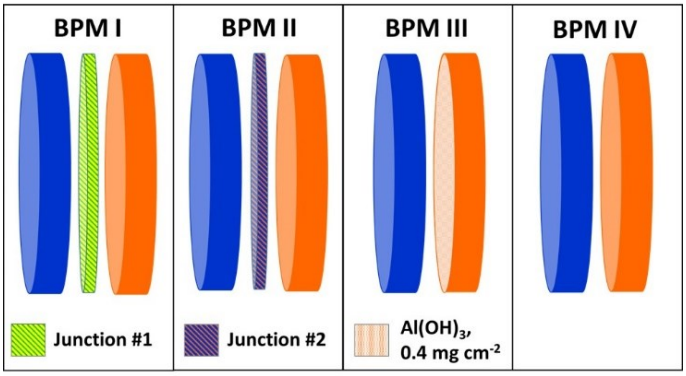

Figure 3.3 **Construction of BPMs I-IV with identical bulk regions and varying interfaces. Sulfonated phenylated polyphenylene(biphenyl) (SPPB) is shown in orange and hexamethyl-p-terphenyl poly(benzimidazole) (HMT-PMBI) in blue. Junction #1 consists of sulphonated poly(ether ether ketone) (SPEEK) and quaternary poly(phenylene oxide) (QPPO) and Junction #2 consisting of SPPB and HMT-PMBI.**

3.2. Experimental

3.2.1. Materials

Poly(ether ether ketone) (PEEK, Vestakeep 4000FP) was obtained from Evonik Corporation as a dry powder. Poly(2,6- dimethyl-1,4-phenylene oxide) (PPO), poly(acrylic acid) (PAA), and poly(4-vinylpyrrolidone) (PVP) were purchased from Sigma-Aldrich as dry powders. Dimethylacetamide (DMAc), dimethylformamide (DMF), dimethyl sulfoxide (DMSO), triethylamine (50% in water), trimethylamine (TMA) (33% in ethanol), chlorobenzene, methanol, and bromine were purchased from Sigma-Aldrich. The sulfuric acid (96 wt %) used for the sulfonation of PEEK was purchased from Fisher Scientific. The aluminum hydroxide used to form BPM junctions #1 and #2 was purchased from U.S. Research Nanomaterials, Inc. ($Al(OH)_3$,10 nm). The aluminum hydroxide used in BPM III ($Al(OH)_3$,30−100 nm) was purchased from SkySpring Nanomaterials, Inc. Sodium hydroxide was purchased from VWR Analytical. Sodium sulfate and sulfuric acid were purchased from Caledon Laboratory Chemicals. All chemicals were reagent grade. Solutions were prepared with 18.2 MΩ cm deionized water from a Milli-Q Gradient system. Spectrograde dimethyl sulfoxide purchased from ACP Chemicals was used for membrane casting. A commercially available Fumasep bipolar membrane (Fumatech BWT GmbH, Germany) was used for comparison with

fabricated BPMs. The electrochemical cell and all electrodes were purchased from Pine Research Inc.

3.2.2. Membrane Preparation

Sulfonated PEEK was prepared by exposing PEEK to sulfuric acid for several days at room temperature. After drying PEEK, the powder was mixed with sulfuric acid and vigorously mixed; the solution became transparent and was red/ brown in color. After 6 days, the solution was precipitated in DI water at 0 °C and dried in a fume hood. Quaternary PPO (QPPO) was prepared by bromination and subsequent amination of the polymer. After drying, PPO was dissolved in chlorobenzene. After the solution was warmed to 165 °C and the reaction vessel was purged with argon, bromine was added to the solution, which was mixed for 4.5 h under a reflux condenser. After completion of the reaction, brominated PPO (Br-PPO) was precipitated in methanol. The cleaned and dried Br-PPO was submerged into TMA in a mixture of ethanol and water for 7 days. The aminated polymer was then dissolved in methanol, dried at ambient conditions, and collected for later use. SPPB and HMT-PMBI were synthesized as previously reported by Adamski et al. and Wright et al., respectively.[139,140] Sulfonated poly(ether ether ketone) and quaternary poly(2,6- dimethyl-1,4-phenylene oxide) were prepared by Devon Powers and Ryszard Wycisk. Dr. Michael Adamski provided sulfonated phenylated polyphenylene(biphenyl). Hexamethyl-p-terphenyl poly(benzimidazole) was prepared by Dr. Andrew Wright.

3.2.3. Membrane Characterization

Ionic conductivity of the hydrated membranes was determined using an AC impedance method. SPEEK and QPPO membrane samples were loaded into a Bekk-Tech 4- electrode cell and submerged in deionized water at 23 °C. Degassed water was used to measure the hydroxide ion conductivity of QPPO. A Gamry Reference 3000 potentiostat was used to generate an impedance spectrum for the samples, and the membrane resistance, R_p, was determined as the intercept of the spectrum with the real-axis. Ionic conductivity was calculated using eq 11, where L is the distance between the electrodes

and A is the cross-sectional area of the membrane when dry. Ionic conductivity of SPPB was determined at 25 °C. Fully hydrated samples were secured in Teflon casing with two platinum electrodes. The casing was filled with deionized water and placed in a humidity chamber at 100% RH and 25 °C. The ionic conductivity was found with AC impedance spectroscopy using a Solartron 1260 frequency response analyzer. A DC voltage of 0 and AC amplitude of 100 mV was used over a frequency range of 10 MHz to 100 Hz. Data were fit to Randles circuit using Scribner ZPlot software, and the charge transfer resistance, R_p, was determined. Again, eq 11 was used to determine the membrane conductivity. Membranes were completely converted to the proton form prior to testing. The ionic conductivity of HMT-PMBI in the hydroxide form was taken from Wright et.al.[46] This was measured at ambient temperature (~22 °C) as a fully hydrated membrane using the same impedance method described above for SPPB.

$$(11) \quad \sigma\left(\frac{S}{cm}\right) = \frac{L\,(cm)}{R_p(\Omega)A(cm^2)}$$

The ion-exchange capacity (IEC) of SPEEK was determined using a standard acid−base titration technique. A SPEEK film of known dry mass in the proton form was soaked at 23 °C for 48 h in 2.0 M NaCl to convert it to the sodium form. The soaked solution was then titrated with 0.01 N NaOH to a neutral pH, and the IEC (mmol/g) of the film was determined using eq 12 where V_t (L) is the titrant volume required to neutralize the soak solution, N_t (mmol/L) is the normality of the titrant, and m_{dry} (g) is the mass of the dry film. The IEC of SPPB was taken from ref17 where it was determined through a similar titration method. The IEC of QPPO was determined using the Mohr titration method. A chloride-form QPPO film of known dry mass was soaked in two 20 mL batches of 0.2 M $NaNO_3$ to exchange Cl^- for NO_3^-.

The soak solutions were combined and were then titrated with 0.01 M $AgNO_3$ using K_2CrO_4 as the end point indicator. The IEC of the QPPO films was again determined using eq 12. The IEC of HMT- PMBI was taken from Wright et. al.[46] This value was determined from the degree of methylation of benzimidazole groups within the polymer.

$$(12) \quad IEC\left(\frac{mmol}{g}\right) = \frac{V_t(L) \times N_t\left(\frac{mmol}{L}\right)}{m_{dry}(g)}$$

Scanning electron microscopy (SEM) images were taken using an FEI Nova NanoSEM 430 system. Energy dispersive X-ray spectroscopy (EDX) was used in conjunction with the SEM to confirm the presence of $Al(OH)_3$ in the interfacial layer. Membrane samples were coated with iridium using a Leica EM ACE600 high-vacuum coating system before SEMs were taken.

Conductivity and IEC measurements were performed by Devon Powers. SEM images were taken by Amelia Hohenadel.

3.2.4. Junction Preparation

Dual electrospun junctions were prepared using a two-spinneret apparatus as described previously.[79,141] In this method, two solutions containing the PEM and AEM polymers are electrospun simultaneously onto a rotating and oscillating drum from two separate syringes. The flow rates were adjusted to compensate for any variation in ion exchange capacity, thus allowing the same approximate conductance across the junction. For example, a higher flow rate, and thus larger amount of polymer, would be used for the polymer with lower IEC to compensate for the slower movement of ions. A small amount of high molecular weight carrier polymer, either poly(acrylic acid) (PAA) or poly(4-vinylpyrrolidone) (PVP), was added to each solution to facilitate fiber formation. The electro- spinning was stopped periodically, and a dispersion of nanoscopic $Al(OH)_3$ catalyst in water was sprayed onto the drum using a hand- held spray gun. This ensured all fibers were coated in a thin layer of $Al(OH)_3$. Table 3-1 presents details of the two types of 3D junctions fabricated for this work. Electrospun junctions were prepared by Devon Powers.

Table 3-1 3D Electrospun junctions

	Junction 1		Junction 2	
	SPEEK (PEM)	QPPO (AEM)	SPPB (PEM)	HMT-PMBI (AEM)
IEC (mmol/g)	1.6	1.4	3.2[139]	2.5[46]
Ionic Conductivity (mS/cm)	37.4a	20.3b	154a	23b [46]
Carrier Polymer	4% PVP	2% PVP	4% PAA	4% PAA
Solvent	DMAc	DMF	16% MeOH 84% DMAc	16% MeOH 84% DMF
Voltage (kV)	15	15	13	11
Flow Rate (mL/hr)	0.15	0.25	0.20	0.51
Temperature (°C)	22		22.7	
Relative Humidity (%)	35		35	
Spinner to Collector Distance (cm)	10.5		10.5	
Al(OH)3 Loading (mg/cm2)	0.5		0.59	

[a] Conductivity of membrane in H^+ form
[b] Conductivity of membrane in OH^- form

3.2.5. Bipolar Membrane Preparation

Single HMT-PMBI and SPPB membranes were cast on glass plates from 10 and 7.5 wt % solutions in DMSO, respectively, using a doctor blade. Cast membranes were dried at 90 °C for >3 h. Membrane were ~30 μm thick. Precise thicknesses are provided in Table 3-2. Bipolar membranes were formed through a combination of solvent exposure and hot pressing of preformed membranes. For BPMs with an electrospun junction, first the precast SPPB membrane and the junction were exposed to MeOH vapors for 10 min before being pressed together by hand. Next, the conjoined SPPB/Junction and HMT-PMBI were exposed to MeOH vapors for 15 min before being pressed together and transferred immediately to a hot-press. The membranes were hot-pressed at 120 °C at 10000 lbs for 40 min. Membranes without a junction were exposed to solvent a total of 15 min before lamination and were hot-pressed under identical conditions. Aluminum hydroxide was added to BPM III by brushing nanoscopic aluminum hydroxide in acetone onto SPPB before solvent vapor exposure. The loading was determined by weight change after addition of the catalyst. After hot-pressing, BPMs were transferred to solutions of 0.5 M Na_2SO_4 for at least 12 h before electrochemical characterization. An overview of

the four BPMs fabricated is given in Table 3-2. The performance of a commercially available Fumasep bipolar membrane was also compared to these BPMs. BPM I was prepared by Devon Powers, Ryszard Wycisk and Amelia Hohenadel. BPMs II, III and IV were prepared by Amelia Hohenadel.

Table 3-2 Bipolar membranes fabricated for this work with thicknesses of bulk PEM and AEM materials.

	PEM	Junction	AEM
BPM 1	SPPB, 33 ± 1.5 µm	Junction # 1	HMT-PMBI, 31 ± 0.63 µm
BPM 2	SPPB 28 ± 1.0 µm	Junction # 2	HMT-PMBI, 28 ± 1.2 µm
BPM 3	SPPB 26 ± 0.75 µm	Al(OH)3, 0.4 mg/cm2	HMT-PMBI, 30 ± 0.63 µm
BPM 4	SPPB 30 ± 1.4 µm	None	HMT-PMBI, 29 ± 0.63 µm

3.2.6. Electrochemical Characterization.

Electrochemical characterization was performed using a 4-electrode glass H-cell with Pt wire as the working and counter electrodes and Ag/AgCl as the reference and sensor electrodes (Pine Research Inc.) as shown in Figure 3.4. A Solartron 1287 potentiostat/galvanostat was used to apply various current densities for 60 s, the last 10 s of which the voltage and current density were averaged and reported. Initial experiments were performed with 0.5 M Na_2SO_4 as the anolyte and catholyte followed by 1 M NaOH and 1 M H_2SO_4 as the anolyte and catholyte, respectively

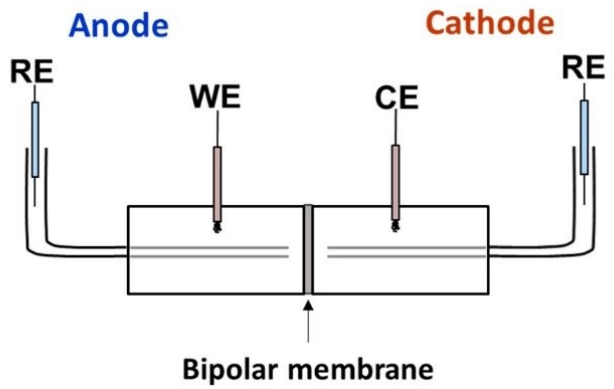

Figure 3.4 **4-electrode electrochemical cell used for bipolar membrane characterization. Ag/AgCl electrodes were used as reference electrodes with Pt wire as working and counter electrodes. Both compartments were filled with 0.5 M Na_2SO_4 for initial experiments at neutral pH. For experiments run with a pH gradient, 1 M NaOH was used as the anolyte and 1M H_2SO_4 as the catholyte.**

3.3. Results and Discussion

Polarization curves obtained in Na_2SO_4 and in acidic/basic media are shown in Figure 3.5, where the potential represents the measured voltage difference between the two reference electrodes, thus revealing current−potential curves that represent the efficacy of the BPMs, devoid of the effects of the electrochemical reaction kinetics at the corresponding working and counter electrodes. BPM performance was assessed quantitatively by comparing the measured potential to the equilibrium potential, E_0 = 0.83 V, for the dissociation of water, $H_2O \rightarrow H^+ + OH^-$. BPMs exhibiting higher overpotentials, i.e., larger differences between the theoretical water dissociation potential and observed potential, are considered to be poorer in performance. In Na_2SO_4, all BPMs are characterized by a low current density region in which voltage increases rapidly, as can be seen in Figure 3.5(a). The plateau that occurs upon drawing current is traditionally associated with the limiting current density regime, wherein current across the BPM is provided by "unwanted" co-ion leakage of anions from the catholyte to anolyte and cations from the anolyte to catholyte.[142] This plateau ends when a voltage capable of dissociating water at the interface is reached. For BPMs I to IV, the limiting current density plateaus all occur between ~4 and 10 mA cm^{-2}; however, the voltages at which water dissociation occur are different, indicating different performance. The commercial

Fumasep membrane exhibits a limiting current density between ~2 and 4 mA cm^{-2}. As the bulk PEM and AEM are the same materials in each of the BPMs, any differences in the polarization curves are the result of the effect of the interfacial region between the PEM and AEM. BPM I shows the best performance, with water dissociation seemingly occurring at ~0.7 V. The exact voltage at which dissociation occurs and extent of dissociation is unknown. Shen et al. attributed the increase in current density below 0.83 V to co-ion leakage through the membrane.[79] The pH of the anolyte and catholyte plays a large role in determining the voltage across the BPM.[143] It is possible that local pH gradients at the membrane surface account for the discrepancy between this value and reported thermodynamic voltage of 0.83 V. As current was increased, the voltage across BPM I remained lower than that of BPMs II to IV and the commercial Fumasep bipolar membrane, proving BPM I's superior performance. BPMs I and II, which comprise junctions 1 and 2, yield lower voltages than BPMs III and IV, which were prepared without the presence of interfacial ionomeric junction. Comparison of BPMs III and IV shows that the inclusion of $Al(OH)_3$ at the PEM|AEM interface reduced the voltage by 0.44 V in Na_2SO_4 at 100 mA cm^{-2}. The same general trend in performance is seen at high current densities when BPMs are run in acid and base, shown in Figure 3.5(b). Again, BPM I is the highest performing membrane and BPM IV exhibits the lowest performance. Addition of $Al(OH)_3$ reduces the potential by 1.09 V at 100 mA cm^{-2} as observed by comparing BPMs III and IV.

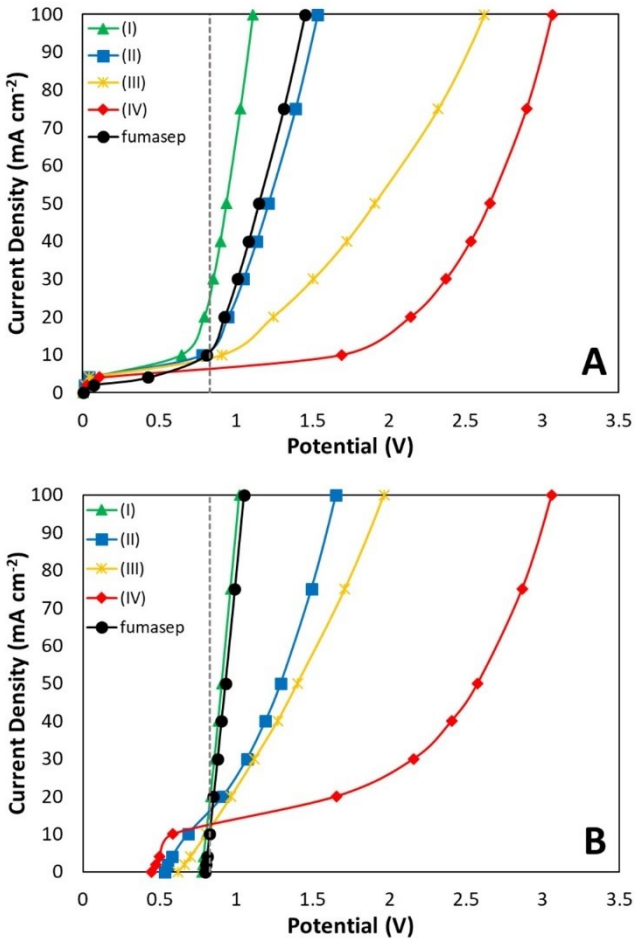

Figure 3.5 **Polarization curves of various BPMs in (A) 0.5 M Na_2SO_4 solution; (B) acidic catholyte, 1 M H_2SO_4, and basic anolyte, 1 M NaOH, at room temperature. The dotted line at 0.83 V represents the theoretical potential for dissociation of water at 25°C.**

However, the overall shape of these polarization curves is generally different than those observed in Na_2SO_4. Bipolar membranes run in acid and base exhibit higher open circuit potentials and more linear behavior. This is most clearly seen for BPMs I and III and for the Fumasep BPM. The polarization curve of BPM II slightly deviates from linearity. BPM IV, however, exhibits a curve similar to that seen in Na_2SO_4 solution with a clear limiting current density region between ~10−20 mA cm^{-2}. No trend is seen when comparing each membranes individual performance in Na_2SO_4 versus acid and base. The potential of the Fumasep membrane and BPM III decrease when run in acid and base, compared to Na_2SO_4, while the overpotentials for BPM I and IV stay approximately the same. The potential of BPM II increases in acid and base. The most noticeable difference

when carrying out experiments in neutral pH and in a cell with acid and base are observed at low current densities. This is apparent in Figure 3.6, which shows a magnified portion of polarization curves obtained in Na_2SO_4 solution (A) and in acid and base (B). At open circuit, when both the catholyte and anolyte contain a neutral salt, the measured voltage across the membrane is close to 0 V. This can be understood by realizing that the potential measured across the BPM is the sum of potentials across three interfaces, namely, the anolyte|AEM interface, the BPM junction, and the catholyte|PEM interface. This is shown in eqs 13 through 15, where R is the universal gas constant, T is the temperature, F is Faraday's constant, and z is the number of electrons transferred.[96] Mathematically, this reduces to a difference in ion concentration between the anolyte and catholyte. Therefore, when both compartments are at a pH of 7, the open circuit voltage, OCV, is 0 V.

$$\Delta\varphi_{total} = \Delta\varphi_{analyte/AEM} + \Delta\varphi_{AEM/PEM} + \Delta\varphi_{PEM/catholyte} \quad (13)$$

$$\Delta\varphi_{total} = \frac{RT}{zF}\log\frac{[H^+]_{AEM}}{[H^+]_{anolyte}} + \frac{RT}{zF}\log\frac{[H^+]_{PEM}}{[H^+]_{AEM}} + \frac{RT}{zF}\log\frac{[H^+]_{catholyte}}{[H^+]_{PEM}} \quad (14)$$

$$\Delta\varphi_{total} = \frac{RT}{zF}\log\frac{[H^+]_{catholyte}}{[H^+]_{anolyte}} \quad (15)$$

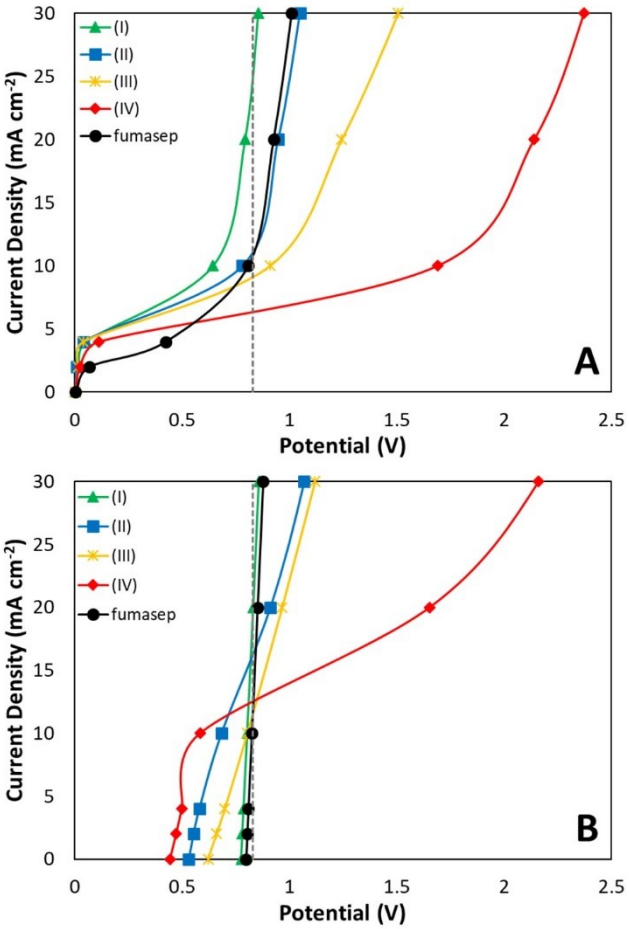

Figure 3.6 **Magnified regions of Figure 5 showing co-ion leakage currents of BPMs in (A) 0.5 M Na_2SO_4 solution; (B) acidic catholyte, 1 M H_2SO_4, and basic anolyte, 1 M NaOH at room temperature. The dotted line at 0.83 V represents the theoretical potential for dissociation of water at 25°C.**

When the catholyte and anolyte contain acid and base, respectively, the theoretical open circuit potential across the BPM is 0.83 V (ΔpH = 14, 25 °C). The observed open circuit potentials deviate from this, indicating that the pH difference is less than 14. Measured OCVs are 0.78 V for BPM I, 0.53 V for BPM II, 0.62 for BPM III, 0.45 V for BPM IV, and 0.80 V for Fumasep. These OCVs provide a measure of the co-ion leakage across the membrane and, hence, permselectivity. Literature commonly refers to co-ion leakage as being due to anions transported from anode to cathode and cations transported from cathode to anode through the BPM, as discussed above. In this case the driving force is neutralization of the pH cell, rather than reverse-bias current flow. This

co-ion leakage is due to protons that are transported from cathode to anode (impeded largely by the AEM) and/or hydroxide ions transported from anode to cathode (impeded largely by the PEM).

Several studies claim that this limiting current density depends on factors other than ion leakage, including the diffusional boundary layer at the electrolyte|membrane interfaces and that only 10−30% of the ionic current is due to co-ion leakage.[93,96,142] These results seem to support this claim. Figure 3.6(a) shows a similar limiting current density for BPMs I to IV, yet open circuit potentials indicate different rates of co- ion leakage through the BPMs. These results additionally show the importance of the interfacial region on permselectivity, as the PEM and AEM components are the same for BPMs I−IV, and thus should equally impede anion and cation transport, respectively, yet the differences in OCV between the BPMs are striking. The PEM|AEM interfacial region plays a critical role in co-ion transport across bipolar membranes. To look at the comparative integrity of the PEM|AEM interfaces for the various BPMs, the cell was run under forward bias, with 1 M H_2SO_4 on the side of the PEM and 1 M NaOH on the side of the AEM, by applying a reverse current. This causes not dissociation of water at the PEM|AEM interface but the formation of water at the interface. In order for the membrane not to rupture upon water generation, it must exhibit sufficient cohesion. The forward-bias experiment can be considered as an accelerated stress test as it mimics the type of physical degradation that may occur after extensive on−off cycling at high reverse-bias current densities. A sudden recombination of protons and hydroxide ions at the interface may create swelling that would damage the interfacial region and/or delaminate the polymers. The forward-bias and subsequent reverse-bias polarization curves are shown in Figure 3.7. Each BPM shows a slightly different behavior under the forward-bias conditions. As expected, there are deviations in the observed OCVs similar to those seen in the previous reverse-bias polarization curve (Figure 3.5(b) and Figure 3.6(b)). Again, it is assumed this is due to co-ion leakage as the pH cell attempts to reach neutrality. All BPMs display very different polarization curves under forward bias, as can be seen in Figure 3.7.

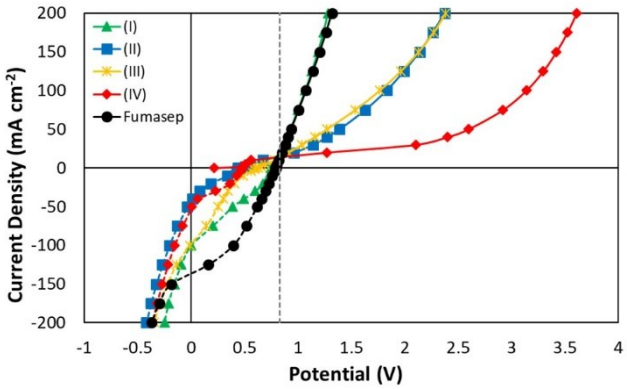

Figure 3.7 **Forward (dotted line) and reverse (solid line) bias experiment with an acidic catholyte, 1 M H_2SO_4, and basic anolyte, 1 M NaOH (B) at room temperature. The dotted line at 0.83 V represents the theoretical water dissociation potential at 25°C across a pH gradient of 14.**

Upon application of negative current, the Fumasep BPM exhibits low resistance followed by what appears to be a limiting current density regime around −100 to −150 mA cm^{-2}. In contrast, BPM II displays highly resistive behavior at low current densities before a more rapid increase in current density. Unfortunately, it is difficult to ascribe these polarization curves to specific BPM characteristics. The changes in slope during the forward-bias polarization results from multiple processes which include recombination of salt at the interface, formation of water at the interface, co-ion leakage, and eventual displacement of Na^+ and SO_4^{2-} ions in the PEM and AEM with H^+ and OH^- ions. These processes are depicted in Figure 3.8.

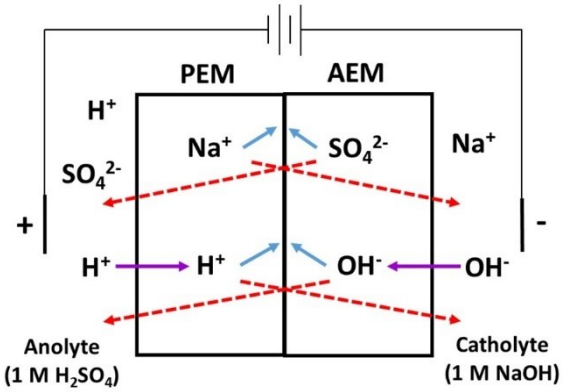

Figure 3.8 **Diagram of ion movement occurring when a bipolar membrane, equilibrated in Na_2SO_4, is operated under forward bias with an acidic anolyte, 1 M H_2SO_4, and basic catholyte, 1 M NaOH (B) at room temperature. Dashed red arrows show co-ion leakage, solid blue arrows show recombination of ions at the interface, and solid purple arrows show the movement of ions in catholyte and anolyte into the membrane.**

A thorough understanding of the behavior of these membranes under forward polarization is not explored in this paper. Rather, the purpose of this experiment is simply to promote the recombination of H^+ and OH^- ions needed to assess adhesion. Following capturing a polarization curve under forward bias, a reverse-bias polarization was taken by applying positive current, shown as the solid lines in Figure 3.7. The potentials reached during this reverse polarization were compared to those in Figure 3.5(b). Any increase in overpotential was attributed to delamination of the AEM and PEM at the interfacial region caused by water formation. The following membranes exhibited increased potentials at 100 mA cm^{-2} when compared to the first polarization curve taken in acid and base: Fumasep (26 mV), BPM I (50 mV), BPM IV (78 mV), and BPM II (180 mV). It is surprising that the overpotential of BPM II increased by more than double that of BPM IV and more than triple that of BPM I. The electrospun junctions present in BPMs I and II should create excellent adhesion between the PEM and AEM. While this seems to be the case for BPM I, BPM II is likely to have undergone severe delamination. To further understand the performance of the bipolar membranes fabricated with dual fiber electrospun junctions, scanning electron microscope (SEM) images were taken of the BPMs and unused electrospun mats. Figure 3.9 shows an aerial view of the two pristine electrospun junctions. Junction #1, prepared from SPEEK and QPPO, can be

viewed has being heterogeneous in nature with fibers <1 μm in diameter. Junction #2, prepared from SPPB and HMT-PMBI, reveals a large degree of heterogeneity. The image of Junction #2 shows a mixture of polymer fibers and solid polymer spheres resulting from evaporation of sprayed droplets. The fibers formed possess diameters of 1−10 μm. Cross-sectional SEM images of BPMs I, and II after the electrochemical characterization described previously are provided in Figures 3.10. BPM II shows considerably more delamination than BPM I.

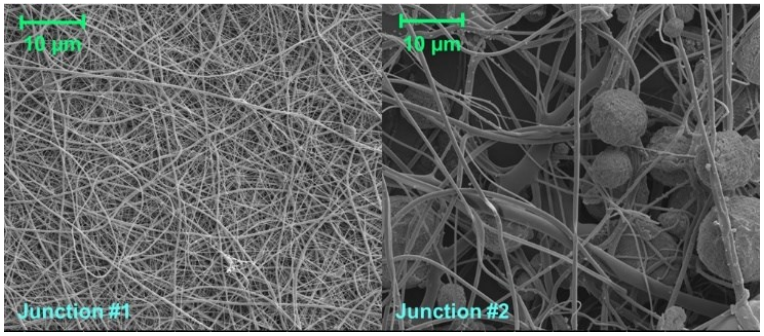

Figure 3.9 Top view SEM image of pristine Junction 1 and Junction 2.

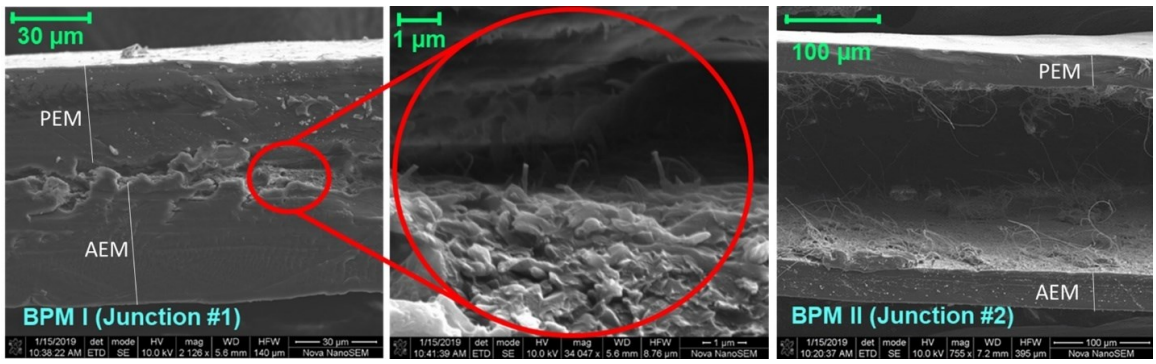

Figure 3.10 Cross-sectional SEM of BPM I and BPM II after electrochemical characterization showing extensive delamination of BPM II.

3.4. Conclusion

Though the bulk PEM and AEM regions did not change, significant variation in BPM performance is observed, thus affirming the importance of the interfacial region, not just for the efficiency of water dissociation but also for membrane selectivity. As expected, the inclusion of $Al(OH)_3$ catalyst lowers the overpotential for water dissociation. Of the four membranes, BPMs I and II were superior, indicating the

importance of high interfacial surface area. BPM II is characterized by poor adhesion, which is attributed to the morphology of junction and properties of the membranes used within the junction.

Chapter 4.

Spectroelectrochemical Detection of the Onset of Water Dissociation in Bipolar Membranes

Reprinted with permission from Amelia Hohenadel, Apurva Shantilal Gangrade, Steven Holdcroft, *ACS Applied Materials & Interfaces* **2021** *13* (38), 46125–46133. https://doi.org/10.1021/acsami.1c12544. [106]

4.1. Introduction

Bipolar membranes (BPM) have been used in electrodialysis and separation processes for decades.[87,88,144,145] Recently, BPMs have been explored as an alternative to mono-pH systems for water electrolysis and CO_2 reduction.[146–150] BPMs are unique in that they combine cation and anion exchange materials such that the anode and cathode electrodes may each be operated at a different pH. Such a system provides a much greater choice of electrode materials and reactions. An abrupt junction exists between the cation exchange membrane (CEM) and anion exchange membrane (AEM) forming an interface analogous to a p-n semiconductor junction. A space charge region exists at this junction under equilibrium as shown by Coster and Ramirez et al.[71–73] When the cell is operated under a significant reverse-bias polarization, in which the positive electrode is located on the side of the AEM and the negative electrode is on the side of the CEM, the width of the this space charge region increases and a strong electric field is formed at this interface.[70] Ionic current may flow either through co-ion leakage currents, or water dissociation.

Water dissociation provides a constant flux of protons and hydroxide ions to the cathode and anode, respectively, thereby maintain a pH difference across the cell. Upon sufficient reverse-bias polarization, the rate of water dissociation within the BPM was found to be 10^7 times greater than in solution and is believed to result from electric field-enhanced dissociation, known as the second Wien effect.[70,75] In addition to this electric field enhancement, the use of catalysts within the BPM junction have been proven to

promote water dissociation. Simons first discovered the catalytic role of weakly basic tertiary amino groups to facilitate water dissociation at the surface of an AEM.[77] Since then, significant experimental and modeling work has been carried out to understand the role of catalysts at the BPM interface.[81,151–153] Water dissociation has been found to increase upon addition of catalysts such graphene oxide, $Al(OH)_3$, and other metal oxides and hydroxides.[83,86,154–156]

Co-ion leakage results from anions in the catholyte migrating to the anode and cations in the anolyte migrating to the cathode. This leakage occurs because the membrane is not perfectly permselective and thus cations may travel through the AEM and anions through the CEM. Permselectivity of an ion exchange membrane (IEM) measures the ratio of flux of counter-ions to the total ionic flux through the membrane. It is generally thought that thinner membranes exhibit lower permselectivity, although in experiments using single ion exchange membranes, permselectivity has been shown to be constant once membranes have exceeded a threshold thickness.[157–160] The permselectivity of a bipolar membrane is further complicated by the gradients of H^+ and OH^- ions as they migrate through the CEM and AEM, respectively. The permselectivity of BPMs has been explored by Moussaoui et al. who studied the effect of external NaCl solution concentration on Na^+ leakage through a BPM.[161] In this work, an expression relating co-ion leakage to 1/thickness was derived. The permselectivity of an IEM can be described by equation 16:

$$\alpha = \frac{t_M^m - t_M^s}{t_X^s} \quad (16)$$

where t represents the transport number of counter-ion, M, or co-ion, X, through the membrane (M) and solution (S) phase. For a perfectly permselective membrane (α =1), t_M^m = 1 and the entire ion transport across the membrane occurs by means of counter-ions. Alternatively, when $t_M^m = t_M^s$, α=0 and ion transport in the membrane is equal to that in solution.

When a bipolar membrane is employed in water electrolysis, the oxygen evolution reaction (OER) is made to occur under alkaline conditions at the anode, while the hydrogen evolution reaction (HER) occurs under acidic conditions at the cathode. The gas evolving reactions, along with their standard electrochemical potentials at pH 14 and

0, respectively, are shown in equations 17 and 18. To reach the required standard electrochemical reduction potential for water dissociation under these conditions (E_0 = 1.23 V) an additional 0.83 V is necessary. This potential is defined, as defined by Oener et al.,[86] as the thermodynamic potential needed to generate 1M acid and 1M base from neutral solution and it is refered to as the 'standard water dissociation potential' throughout the text. This electric potential drop, shown in equation 19, occurs across the BPM interface and can be related to the difference in pH values between the AEM and CEM layers.

$$(17) \quad 4OH^- \rightarrow 2H_2O + O_2 + 4e^-, \quad E^0_{anode} = 0.40\ V$$

$$(18) \quad 4H^+ + 4e^- \rightarrow 2H_2, \quad E^0_{cathode} = 0.00\ V$$

$$(19) \quad H_2O \rightarrow H^+ + OH^-$$

$$E^0_{junction} = \frac{RT}{F}\ln\left(\frac{a^{H^+}_{CEM}}{a^{H^+}_{AEM}}\right) = 0.83\ V,\ pH_{AEM} - pH_{CEM} = 14$$

The most common method of electrochemical characterization of BPMs involves generation of current-voltage (I-V) polarization curves, which relate current density to the potential across the bipolar membrane, the latter being typically measured using a 4-electrode system in which two reference electrodes are placed on either side of the BPM, thus measuring the electric potential drop across the membrane, excluding polarization losses due to OER and HER reactions.

The water dissociation onset potential under standard conditions, assuming the activities of H^+ and OH^- are one in the CEM and AEM, respectively, is 0.83 V, as shown in equation 19. However, it must be recognized that the potential measured across the membrane is not just the potential drop across the interfacial layer or bipolar junction, V_j, but includes the two Donnan potentials, V_{Don}, at each membrane solution interface as illustrated in figure 4.1.[94,96]

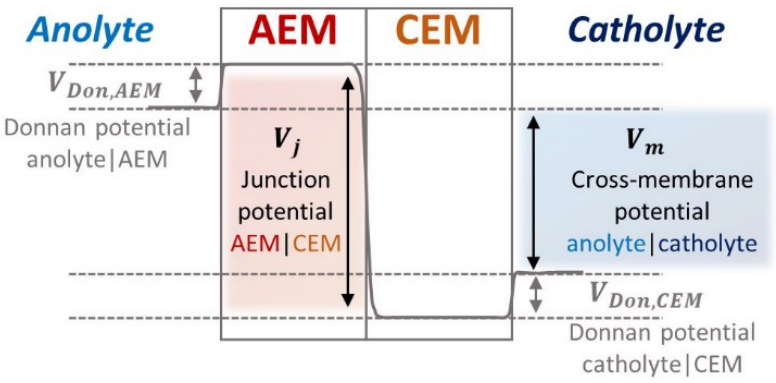

Figure 4.1 **Potential distribution across a BPM and surrounding solution showing the Donnan potentials that occur at each membrane|solution interface, V_{Don}, and the potential occurring at the AEM|CEM junction, V_j. The potential measured by reference electrodes on either side of the BPM in a typical 4-electrode cell is the sum of these three potentials and is represented by V_m.**

The total current under reverse-bias polarization is the sum of the ionic current resulting from water dissociation, and the ionic current resulting from co-ion leakage through the BPM. When operating a BPM, it is typically desirable to maximize the water dissociation current to maintain a pH difference between the electrodes. Under these circumstances, co-ion leakage is considered a loss in efficiency.

It has been postulated that the point on the polarization curve which exhibits the largest resistance, is the point at which the current is dominated by the transport of protons and hydroxide ions,[73] which typically occurs immediately after the first limiting current density, shown as point "B" in figure 4.2. Many reports have now shown evidence of co-ion leakage occurring at cross-membrane potentials below 0.83 V and within the limiting current density region. Sun et. al. used inductively coupled plasma mass spectrometry (ICP-MS) of the anolyte and catholyte solutions to measure co-ion leakage currents and reported that water dissociation accounts for the majority of charge carriers generated at current densities as low as 0.5 mA cm^{-2}, where the cross-membrane voltage was 0.75 V. This was rationalized by accounting for the difference in pH between the anolyte and catholyte solutions which was <14.[94] Bui et. al. modeled IV curves for a BPM in four different pH gradients.[105] In this work, the modeled polarization curves were deconvoluted to calculate the contribution of individual ionic species to the total ionic

current density. The data suggested that contribution of water dissociation becomes significant above 0.6 V and within the limiting current density region.

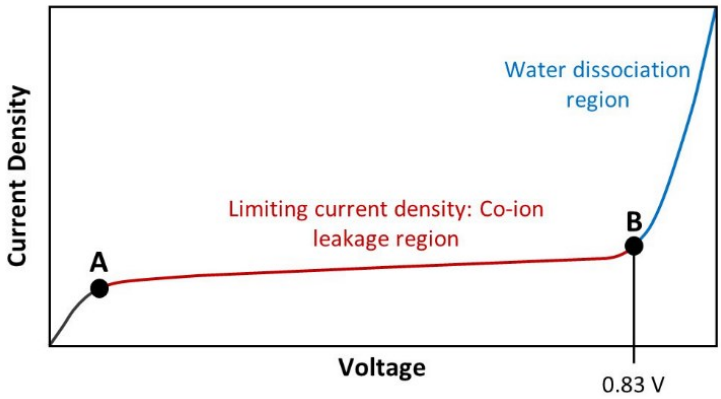

Figure 4.2 **Typical bipolar membrane polarization curve obtained from a four-electrode cell operated in a pH neutral electrolyte. Points A and B define the bounds of the limiting current density which has historically been attributed to co-ion leakage current. Point B shows the standard water dissociation potential assuming a pH difference of 14 across the interface, i.e., 0.83 V.**

Although researchers have utilized quantitative tools such as ICP-MS and pH monitoring of the electrolyte to measure co-ion leakage, these techniques lack the ability to report on water dissociation in real time. This means that measured co-ion leakage may be distorted by degradation of the BPM or changes in the BPM interface that may occur over the measurement time.

A method to confirm water dissociation over the course of seconds rather than hours would reduce the likelihood of membrane degradation and changes to electrolyte concentration. This requires a technique which can accurately assess the presence of either hydroxide ions or protons as they form at the BPM AEM|CEM junction, thus distinguishing currents originating from water dissociation from co-ion leakage. The detection of electrochemically-generated hydroxide ions within an anion exchange membrane has been demonstrated by Cao et. al. using a pH indicator incorporated within the membrane.[57] In that work, thymolphthalein was cast with hexamethyl-p-terphenyl poly(methylbenzamidazolium) (HMT-PMBI) to visualize the transformation of the AEM from bicarbonate to hydroxide form. The indicator-imbibed polymer membrane is a yellow-orange in color in solutions of low pH, where the counter ion is halide or sulfate

ions, for example, but dark blue when converted to the hydroxide form in high pH solutions. In the context of bipolar membranes, Yan et al. recently reported on a BPM for CO_2 electrolysis which utilized a ratiometric pH indicator covalently bonded to weakly acidic ion exchange layers deposited on the CEM side of the BPM. These layers allowed for monitoring of the cathode pH, which plays an important role in the faradaic efficiency of CO_2 reduction.[162]

The research described herein adopts the use of an indicator-imbibed polymer membrane to report on the change in pH that occurs in the membranes as hydroxide ions are produced by water dissociation. When a BPM based on a pH indicator/HMT-PMBI membrane is placed under a reverse bias potential, water dissociation occurs at the AEM|CEM junction. Due to the applied potential, OH^- produced at the AEM|CEM junction diffuses in the AEM portion of the BPM, where it deprotonates the pH indicator and produces a visible colour change. This is illustrated in Figure 4.3, which shows the absorbance spectrum of a BPM under 3 different current densities. As the current density is increased and water dissociation is initiated, a change in absorbance of the indicator related to the change in pH is observed. This colour change is detected using UV/Vis spectroscopy and allows for continuous measurements to be made on the timescale of milliseconds. In this research, polarization curves and UV/Vis spectra of the BPM are measured simultaneously. A previous reported polymer, sulfonated phenylated polyphenylene with a biphenyl linker unit (SPPB) is used as the CEM.[139] By using SPPB in conjunction with HMT-PMBI, a fully hydrocarbon BPM system is employed. Fully hydrocarbon polymers are an attractive alternative to the traditional perfluorosulfonic acid (PFSA) polymers typically used as CEMs for a variety of reasons. Among these reasons are their ease of synthesis, relative low cost, low gas crossover in electrochemical systems such as fuel cells, and fewer environmental concerns.[163]

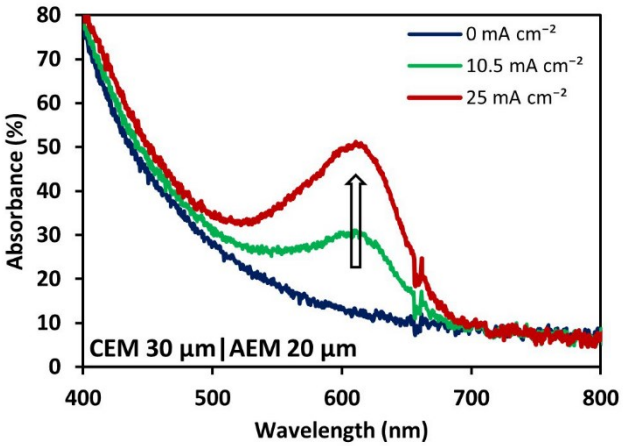

Figure 4.3 **UV-Vis spectra of BPM with thymolphthalein doped hexamethyl-p-terphenyl poly(methylbenzamidazolium) (HMT-PMBI) used as bulk AEM material under reverse polarization at 0, 10.5, and 25 mA cm^{-2}, and sulfonated phenylated polyphenylene with a biphenyl linker unit (SPPB) CEM. As OH^- ions are formed at the AEM|CEM interface and migrate through the AEM. Deprotonation of pH indicator, thymolphthalein, creates a visible colour change.**

The goal of this work is to determine the current density at which it is possible to detect the presence of hydroxide ions, i.e., field generated dissociation of water. This knowledge will strengthen our understanding and interpretation of IV curves obtained from four-electrode BPM systems. The topic of co-ion leakage is further explored by examining a series of bipolar membranes with varying thicknesses of the CEM and AEM components. Asymmetric bipolar membranes have been previously reported in the literature but the effect of decreasing either the AEM or CEM layer on overall BPM performance is variable and depends on the individual membrane properties.[100,101,105,164,165] To date, no such study has been performed using SPPB and HMT-PMBI. Co-ion leakage currents can be further understood by determining the permselectivity of the individual AEM and PEM. Electrochemical impedance spectroscopy (EIS) is also employed to provide additional insights into voltage dependent water dissociation vs. co-ion leakage.

4.2. Experimental

4.2.1. Materials

ACS grade Na_2SO_4, DMSO, and deuterated DMSO were purchased from Fisher Scientific. ACS grade Na_2CO_3, $NaHCO_3$, NaCl and NaOH were purchased from ACP chemicals. Thymolphthalein was purchased from Eastman Organic Chemicals. All solutions were made using 18.2 MΩ cm deionized water using a Millipore Synergy UV water purification system. Hexamethyl-p-terphenyl poly(methylbenzamidazolium), HMT-PMBI, was used as the anion exchange membrane in this work. HMT-PMBI was co-cast with 0.1 wt % thymolphthalein indicator as described by Cao et. al.[57] The cation exchange membrane used was sulfonated phenylated poly-phenylene with a biphenyl linker, SPPB. Structures of these polymers are shown in figure 4.4. SPPB was provided by Dr. Michael Adamski. HMT-PMBI was provided by Dr. Andrew Wright. Indicating HMT-PMBI was provided by Xinzhi Cao.

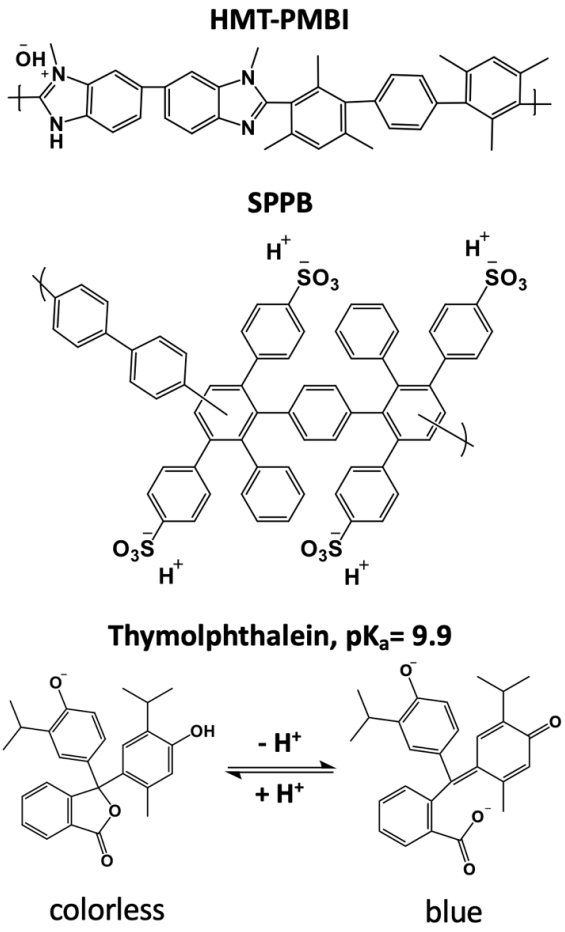

Figure 4.4 Chemical structures of the anion exchange membrane, hexamethyl-p-terphenyl poly(methylbenzamidazolium), HMT-PMBI, the cation exchange membrane sulphophenylated polyphenylene with a biphenyl linker, SPPB, and thymolphthalein indicator in its protonated and deprotonated form.

4.2.2. Physical Characterization

Thymolphthalein was uniformly incorporated into the HMT-PMBI membranes by stirring the indicator and polymer in DMSO before casting on a glass plate. Water uptake and volumetric swelling of the HMT-PMBI containing 0.1% thymolphthalein were found by recording the mass and dimensions of several membranes when fully hydrated and dry. Membranes were hydrated by soaking in DI water and patted dry before weighing. Membranes were dried under vacuum for 24 hours before dry measurements were made. Water uptake, W_u, and volumetric swelling, S_v, were found using equations 20 and 21 where W_w and W_d are the mass of wet and dry membranes, respectively, and V_w and V_d

are the wet and dry volumes of the membrane samples, respectively. Volumes are calculated and the product of membrane width, length, and thickness. Properties of the polymers are shown in table 4-1.

$$W_u(\%) = \frac{W_w - W_d}{W_d} \times 100 \quad (20)$$

$$S_v(\%) = \frac{V_w - V_d}{V_d} \times 100 \quad (21)$$

Table 4-1 Properties of the polymers used in this study.

	IEC (mmol g^{-1}) (Theoretical, OH- form)	σ (mS cm^{-1})	Volumetric Swelling (%)	Water Uptake (%)
HMT-PMBI containing 0.1% thymolphthalein	Series A-E: 2.27 Series F-H: 2.36	97.6[57] at 40°C and 90% RH (OH^- form)	59 ± 4 (Cl^- form)	48.0 ± 8.7 (Cl^- form)
SPPB (H^+ form)	3.46[139]	129[139] at 30°C and 95% RH	145.1 ± 0.5[139]	119.2 ± 1.8[139]

4.2.3. BPM Fabrication

BPMs were fabricated by hot-pressing pre-cast HMT-PMBI and SPPB membranes at 120°C under a pressure of 27 lbs. cm^{-2} for 10 minutes to form a uniform 2D interface. A water dissociation catalyst was not used in this work because its inclusion led to irreproducible I-V characteristics. Catalyst-free BPMs, while being more resistive to water dissociation provided reproducible I-V characteristics, allowing for a more meaningful spectroelectrochemical study. A complete list of the BPMs characterized is provided in table 4-2. The thickness of the SPPB CEM was varied in series A-E, while the thickness of the HMT-PMBI AEM was varied in series F-H. Series A-E used a different batch of HMT-PMBI than the series F-H. The two batches of polymer were compared using NMR and the ion exchange capacity of each batch was found using a previously reported method.[46] All BPMs were exchanged to their Na_2SO_4 form by solution exchange using three 24-hour exchanges in 0.5 M Na_2SO_4 solution before spectroelectrochemical measurements were made.

Table 4-2 **Complete list of BPMs used in this study with corresponding thicknesses of the AEM, hexamethyl-p-terphenyl poly(methylbenzamidazolium) (HMT-PMBI), and CEM, sulfonated phenylated polyphenylene with a biphenyl linker unit (SPPB)**

Series	CEM|AEM thickness (μm)	Individual Sample	CEM|AEM thickness (μm)
A	***42±1***|21±<1	A1	41±1|22±<1
		A2	41±1|21±<1
		A3	43±<1|21±<1
B	***33±1***|20±1	B1	34±1|19±<1
		B2	33±1|21±<1
		B3	33±<1|20±<1
C	***25±2***|21±1	C1	26±1|20±<1
		C2	25±<1|21±1
		C3	23±1|21±<1
D	***16±1***|20±<1	D1	19±<1|20±<1
		D2	17±1|20±<1
		D3	16±<1|19±1
E	***13±1***|20±<1	E1	12±<1|21±<1
		E2	12±<1|20±<1
		E3	13±1|20±<1
F	31±1|***21±1***	F1	31±1|21±1
		F2	30±<1|20±1
		F3	31±<1|21±1
G	30±<1|***31±1***	G1	30±<1|30±1
		G2	31±<1|30±1
		G3	30±<1|32±1
H	32±1|***40±2***	H1	31±<1|40±1
		H2	33±1|40±1
		H3	31±<1|38±2

4.2.4. Electrochemical Characterization

A four-electrode cell, shown in figure 4.5, was used for all measurements. During these measurements 0.5 M Na_2SO_4 solution was circulated through both compartments at a flow rate between 12-13 mL/min using INTLLAB dosing pumps, model DP385. Two

pumps provided a constant flow of solution below the membrane and reference electrodes. Another two pumps, situated next to the working and counter electrodes, pumped excess solution out of the cell. This ensured that there was no pH change in the bulk solution which would result from the oxygen and hydrogen evolution reactions at the working and counter electrodes, respectively. A Neware Battery Testing System, model CT-ZWJ-4'S-T-1U (China), was used as the galvanostat. Ag/AgCl reference electrodes (Pine Research) were used and Pt flag electrodes were used as the working and counter electrodes. Two types of steady state polarization curves were obtained for each BPM in series A - E. The first was a stepped protocol which the applied current density was incrementally increased from 0 to 30 mA cm^{-2} in 4-minute steps to BPMs with 1.5 cm^2 active area. The second was a square-wave protocol which alternated between the applied current density and 0 mA cm^{-2} for 4 and 2 minutes, respectively. The average voltage over the last 30 seconds of each applied current is reported. Only the stepped protocol was used to measure polarization behaviour of series F – H. Both the cross-membrane voltage measured between the sense and reference electrodes and the visible absorbance were recorded continuously during polarization curves. Electrochemical impedance spectroscopy was performed at room temperature (approx. 22 ºC) using the 4-electrode H-cell previously described with Na_2SO_4 solution flowing through both compartments 13-15 mL min^{-1}. A Gamry Interface 5000 Potentiostat/Galvanostat/FRA was used. Several experiments were performed on each BPM to obtain data at various current densities. The applied direct current density (DC) ranged from 0 mA cm^{-2} to 20 mA cm^{-2} with an alternating current (AC) half the applied direct current. For the experiments carried out in the absence of an applied direct current, an alternating current of 2 mA cm^{-2} was used. The frequency range of the alternating current was 10 kHz to 10 mHz.

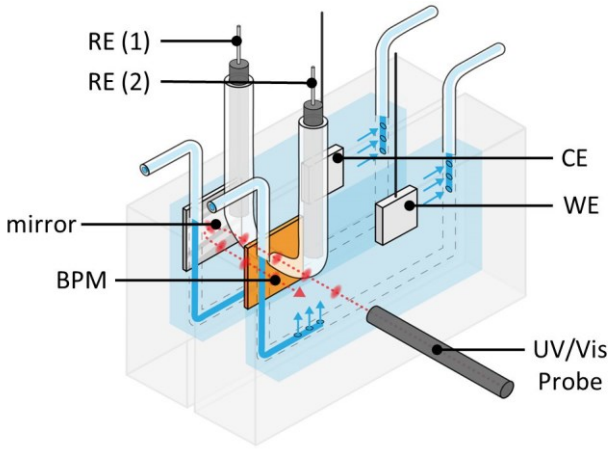

Figure 4.5 **4-Electrode quartz H-cell used for spectroelectrochemical measurements. Two compartments containing 0.5 M Na_2SO_4 solution are separated by the bipolar membrane (BPM). Ag/AgCl reference electrodes (RE) monitor the voltage across the BPM while Pt flag electrodes served as the working electrode (WE) and counter electrode (CE). A UV/Vis reflectance probe was used to simultaneously measure the absorbance of the BPM. Light emitted from this probe passed through the quartz cell, and mirror placed behind the quartz cell reflects it back through the BPM, creating a stronger absorbance signal and improving the signal to noise ratio. Figure prepared by Celeste Jhala.**

4.2.5. UV/Vis Spectroscopy

An Ocean Optics Flame Miniature Spectrometer, model S-XR1-ES, was used in conjunction with a reflectance probe as the UV/Vis Spectrometer. An Ocean Optics DH-2000-FHS dual halogen/deuterium lamp was used as the beam source. The UV/Vis was calibrated to 0% and 100% absorbance using the H-cell containing Na_2SO_4 solution, but no BPM, in the absence and presence of the deuterium/halogen light source, respectively. The average absorbance between 609-618 nm was used to confirm the presence of hydroxide ions. The absorbance from 785-815 nm was subtracted from each point to reduce spectral noise and points were background-corrected by subtracting the average absorbance at 0 mA cm^{-2} (0 V) from each point in polarization curve. Absorbance spectra were taken every 33 ms.

The relationship between absorbance and soaking solution pH was explored by exchanging indicating HMT-PMBI in CO_3^{2-}/HCO_3^- buffer solutions. After 24 hours the polymers were placed in the electrochemical cell and the absorbance was measured. The

solution pH was measured using an Metrohm 848 Titrino Plus with a Metrohm pH electrode. 1 M NaOH made from argon bubbled MilliQ ultra-pure water was used as the pH 14 soaking solution. The pH of this solution could not be accurately measured on with the Titrino Plus and pH was assumed to be 14. The ionic strength of the NaOH solution used at pH was 1. The ionic strengths of the buffer solution varied from 0.5 – 0.75 as the proportion of carbonate to bicarbonate varied.

4.2.6. Permselectivity Measurements

A static approach which ignores the effects of boundary layers and solution-membrane interfaces was used to measure the apparent permselectivity of the individual membranes in the BPM. When an AEM or CEM is positioned in a two-compartment cell with different electrolyte concentrations, a concentration gradient develops across the membrane causing ion transfer from a solution with a high concentration to low concentration. Ion transfer establishes an electric potential difference across the membrane, (E_m). E_m can be used to determine the apparent counter-ion transport number (t_M^m) and the apparent permselectivity (α) in the membrane phase using the following equations:[116,166,167]

For a 1:1 electrolyte:

$$E_m = (2t_M^m - 1)\frac{RT}{F}\ln\frac{a_{\pm}^H}{a_{\pm}^L} \quad (22)$$

$$t_M^m = \frac{E_m \Big/ \left(\frac{RT}{F}\ln\frac{a_{\pm}^H}{a_{\pm}^L}\right) + 1}{2} \quad (23)$$

$$\alpha = \frac{E_m \Big/ \left(\frac{RT}{F}\ln\frac{a_{\pm}^H}{a_{\pm}^L}\right) + 1 - 2t_M^s}{2t_X^s} \quad (24)$$

where, R is the ideal gas constant (8.314 J $mol^{-1}K^{-1}$), T is the absolute temperature (K), F is Faraday's constant (96485 C mol^{-1}), z is the charge on the counter-ion, $\alpha_{\pm}^H$ ($\alpha_{\pm}^H = \sqrt{\alpha_+^H \alpha_-^H}$) and $\alpha_{\pm}^L$ ($\alpha_{\pm}^L = \sqrt{\alpha_+^L \alpha_-^L}$) are the mean activity's of high and low concentration

salt solutions, (t_M^s) and (t_X^s) are the transport number of counter-ions and co-ions in the solution phase, respectively. The membrane potential is negative for CEMs and positive for AEMs as the sign depends on the charge on the respective counter-ions.

An acrylic cell (H-type) was used to measure the membrane potential across the IEM. The two 15 mL compartments were separated by samples of HMT-PMBI or SPPB of different thicknesses. Ag/AgCl wire electrodes, placed 3 mm from the membrane, were used as reference electrodes.[168]. 0.5M and 0.1M NaCl solutions were pumped into the compartments at a 23 mL/ min using a double channel peristaltic pump (BT100-1L-B, DG-2-B, Langer Instruments Corp., USA), Magnetic stirrers were placed in each solution compartment to avoid concentration boundary layer errors in the measurements. All experiments were conducted at 20±0.3°C. The potential difference (E_x) between reference electrodes was measured using a multimeter. All experiments were run for at least 60 minutes, and the membrane potential (E_x) values were taken using the last 30 minutes of each 60-minute experiment. The offset potential between the pair of reference electrodes was determined by immersing both electrodes in 0.5M and 0.1M NaCl solutions and averaging the two potentials, equation (24). The offset potential (E_{offset}) and ideal potential difference of Ag/AgCl wire electrodes in 0.5M and 0.1M NaCl solution at 20 °C ($E_{ideal,20\,°C} = -37.24\ mV$) was subtracted from E_x to obtain the effective membrane potential (E_m) for respective IEMs.[168] Using the effective membrane potential E_m ($E_m = E_x - E_{offset} - E_{ideal}$) and the equations (22) and (23), the transport numbers (t_M^m) and permselectivity values (α) of counter-ions were calculated.

$$E_{offset} = \frac{\Delta E_{0.5M} + \Delta E_{0.1M}}{2} \quad (24)$$

Permselectivity measurements were provided by Apurva Shantilal Gangrade.

4.3. Results and Discussion

4.3.1. IV Curve Analysis

By relating the applied current, cross-membrane voltage, and the change in absorbance of the reporting pH indicator incorporated in the BPM, it is possible to determine the cross-membrane potentials at which water dissociation occurs and where these potentials lie on the IV curves for samples with a variety of bulk AEM and CEM thicknesses. The polarization curves in figure 4.6 reveal typical IV behaviour of a BPM. A sharp increase in current is followed by a limiting current density region where there is a very small increase in current density over a wide range of voltages. The end of the limiting current density region is characterized by a sharp increase in current density. Figure 4.6 (a) indicates there is an increase in the limiting current density between approximately 0.1 V – 1.5 V, determined by the CEM thickness, which varies from 42 μm to 13 μm. A decrease in potential at higher current densities with decreasing CEM thickness is observed. When the thickness of the AEM is varied and the CEM thickness held constant, there are no significant changes to the polarization curve, as shown in figure 4.6 (b). It is apparent that varying the SPPB layer thickness has a much larger effect on current-voltage characteristics than varying the HMT-PMBI layer thickness.

Both BPMs use identical SPPB polymer as the CEM, but the HMT-PMBI polymer, used as the AEM, has different ion exchange capacities in series B and F, as reported in table 4-1. From figure 4.7 it is clear that that series B, with an IEC of 2.27, exhibits a higher limiting current density and higher voltages at current densities above 15 mA cm^{-2} than series F, with an IEC of 2.36. The IEC of the AEM contributes to BPM performance in many ways. As IEC increases, the ionic conductivity of the bulk AEM will increase explaining the differences at higher current densities. The limiting current density seems to indicate that less co-ion leakage occurs in series F. It likely that the higher IEC and greater density of fixed charges creates a stronger space-charge region under reverse polarization, allowing for increased water dissociation. The same trend was observed by Kang et. al. who, using commercial membranes of different ion-exchange capacities, reported improved water splitting capabilities for membranes with higher fixed charge densities.[137] Bui et, al. modeled the effects of changing of BPM ion-

exchange capacity and showed a decrease in the potentials at which the first limiting current density ended suggesting an improvement in water spitting capability. However, an increase in co-ion leakage with increasing ion-exchange capacity was also observed and attributed to a change in water uptake and thus permselectivity.[105]

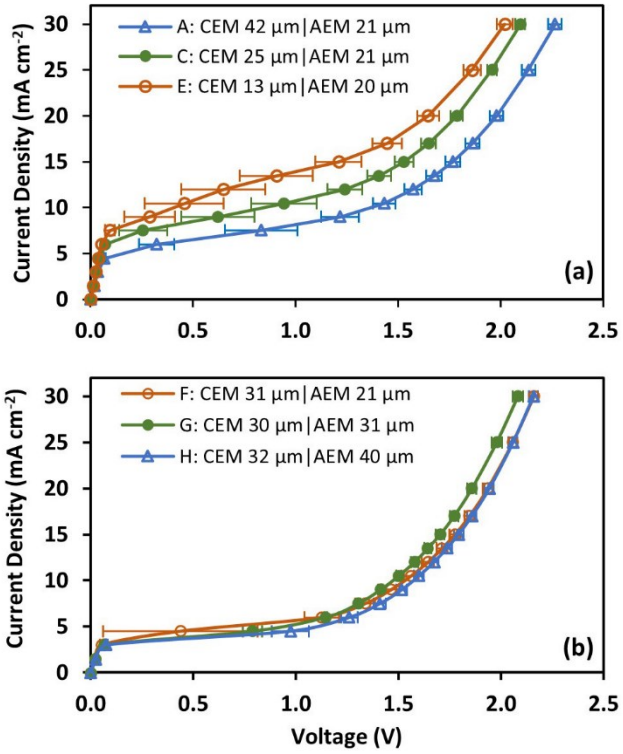

Figure 4.6 **(a) Polarization curves of BPM series A (CEM 42 µm| AEM 21 µm), C (CEM 25 µm| AEM 21 µm), and E (CEM 13 µm| AEM 20 µm), and (b) polarization curves of BPM series F (CEM 31 µm| AEM 21 µm), G (CEM 30 µm| AEM 31 µm), and H (CEM 32 µm| AEM 40 µm) obtained using a 4-electrode cell flowing 12-13 mL/min Na_2SO_4 solution at room temperature. Each point represents the mean value of the final potentials with error bars at one standard error of the mean.**

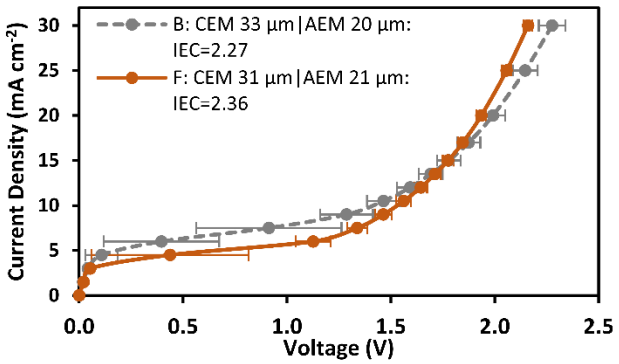

Figure 4.7 **Comparison of polarization data from series B (CEM 33±1 µm| AEM 20±1 µm) and series F (CEM 31±1 µm| AEM 21±1 µm) under identical conditions. The sulfonated phenylated polyphenylene with a biphenyl linker unit (SPPB) polymer, used as the CEM, was identical for these two series, but the hexamethyl-p-terphenyl poly(methylbenzamidazolium) (HMT-PMBI) polymer, used as the AEM, had different ion exchange capacities of 2.27 and 2.36 mmol g^{-1} in the OH^- form for series B and F, respectively.**

4.3.2. Permselectivity

If the limiting current density region is in fact dependent on co-ion leakage, then these results suggest that the permselectivity of SPPB is more dependent on thickness than that of HMT-PMBI. In other words, decreasing SPPB thickness from 42 µm to 25 µm may create a significant increase in the rate of co-ions, SO_4^{2-} , migrating through the BPM. In contrast, decreasing the HMT-PMBI thickness by a similar amount, 40 µm to 21 µm does not appear to increase the rate of migration of Na^+ through the BPM. This hypothesis is supported by measuring the apparent permselectivity of the individual membranes, plotted in figure 4.8. It should be noted that the apparent permselectivity presented in this work neglects boundary effects and the effects of water transport through the membranes. The permselectivity of SPPB reduces from 0.841 to 0.681 as the thickness is reduced from 50 to 15 µm, as shown in figure 4.8 (a). This corresponds to a large permselectivity decrease of 0.160 over a 35 µm decrease in thickness. By comparison, the permselectivity of HMT-PMBI decreases from 0.944 to 0.914 between 52 and 12 µm, corresponding to a decrease of just 0.040 over 40 µm, as shown in figure 4.8 (b). Not only does the permselectivity of SPPB vary widely over this thickness range,

its magnitude is significantly lower than that of HMT-PMBI. This indicates SPPB is relatively leaky to co-ions and that co-ion leakage can be reduced by increasing its thickness. HMT-PMBI is much more permselective against co-ions and consequently relatively less affected by changes in thickness. It should also be noted that the values reported in figure 4.8 were determined experimentally in NaCl electrolyte, not Na_2SO_4 as used for IV studies, but it is reasonably expected that the same general trends would exist with permselectivity increasing with membrane thickness.

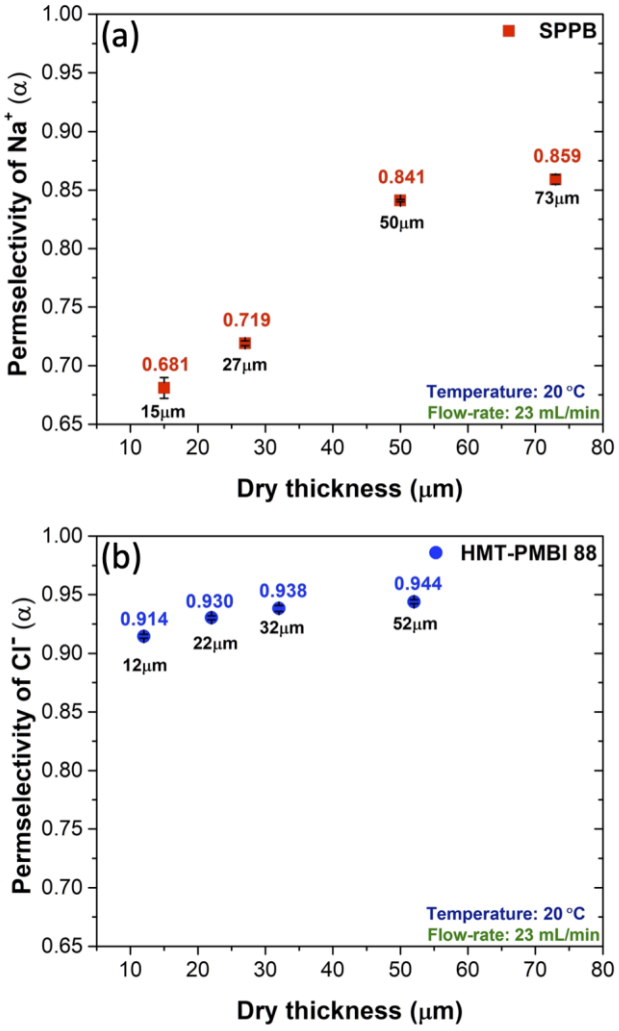

Figure 4.8 **Permselectivity values for the membranes used in this study obtained using the static method in a concentration gradient cell with 0.5 M and 0.1 M NaCl solutions at room temperature. (a) Permselectivity of Na^+ through sulfonated phenylated polyphenylene with a biphenyl linker unit (SPPB) as function of membrane thickness. (b) Permselectivity of Cl^- through hexamethyl-p-terphenyl poly(methylbenzamidazolium) (HMT-PMBI) as a function of membrane thickness.**

4.3.3. Spectroelectrochemical Analysis

The polarization curves and permselectivity data presented above suggest that the limiting current density is a direct indicator of co-ion leakage currents. However, the spectroscopic data presented below will prove that water dissociation is occurring throughout the limiting current density region.

The voltages obtained from each individual polarization curve were plotted against the absorbance of the BPM in figure 4.9. The dashed lines at 0.83 V in these figures represents the standard water dissociation potential derived from the Nernst equation (equation 19). The increase in absorbance seen between 609-618 nm results from deprotonation of the thymolphthalein indicator which turns blue in solutions ranging from pH 9.3 – 10.5. This color change is a direct result of the hydroxide ions resulting from water dissociation in the interfacial region of the BPM. From these results, the generation of hydroxide ions in sufficient amount to deprotonate thymolphthalein is confirmed at potentials as low as 0.4 V in the case of series A – E (varied CEM thickness), and as low as 0.3 V in the case of series F – H (varied AEM thickness).

The absorbance of indicating HMT-PMBI was related to soaking solution pH by soaking polymers in 0.5M $NaHCO_3/Na_2CO_3$ buffer solutions of varying pH shown in figure 4.10. These values are compared to the minimum and maximum experimental values (before zeroing data with 0 mA cm^{-2} absorbance). Although thymolphthalein has a pKa of 9.9 and typically undergoes a color change between pHs of 9.3 and 10.5, these membranes begin absorbing light in the 609-618 nm range at a pH of 8.9 and do not reach their maximum absorbance until after a pH of 10.9. It has been shown that pH-responsive dyes and indicators incorporated into ion exchange membranes behave differently than the same indicators in solution. Though not clearly understood, it is

postulated that a combination of ionic interactions between the polymer and indicator, and possible aggregation of the indicator molecules account for this discrepancy.[169,170] Although the hydroxide concentration within HMT-PMBI is not quantified using the absorbance of thymolphthalein, it can be seen from figure 4.10 that once the membrane is equilibrated in a solution above pH 9.3 there is an appreciable increase in absorbance. This data proves that while the degree of co-ion leakage through the BPM does impact the limiting current density, water dissociation is also occurring throughout this region. From figure 4.9 (a) there does not appear to be a trend between the CEM layer thickness and the voltages at which absorbance increases. This indicates water dissociation is dependent on the cross-membrane potential, not the thickness of the CEM, and that the greater current densities observed in figure 4.6 (a) result from the greater contribution of co-ion leakage to the overall current. Figure 4.11 shows the relationship between absorbance vs. potential, and current density. An increase in absorbance is attributed to the water dissociation reaction occurring at the bipolar membrane interface. There is no discernible relationship between potential and the water dissociation as shown in figure S3 (a) suggesting that water dissociation, while dependent on cross-membrane potential, is independent of SPPB thickness. However, figure S3 (b) shows a clear relationship between the current density at which water dissociation occurs and CEM (SPPB) layer thickness. A students t-test (one-tailed distribution, heteroscedastic, p=0.05) was performed which confirms that the absorbances of BPMs A (thickest SPPB layer) and E (thinnest SPPB layer) are significantly different between current densities of 4.5 – 12.0 mA cm^{-2}. This shows that a greater proportion of the current passed is due to co-ion leakage when using a thinner SPPB layer. In figure 4.9 (b) it is apparent that absorbances of the BPMs in series F are lower than those of series G and H. This is attributed to the decrease in the AEM layer which contains the pH indicator.

Figure 4.12 shows the response time of the spectroelectrochemical method. The measured potential and absorbance are shown upon reverse-bias at a specific current density, shown in green. At 9 mA cm^{-2} water dissociation is occurring at an extent sufficient to produce a visible colour change. Immediately after the applied current is removed the absorbance decreases to near 0%.

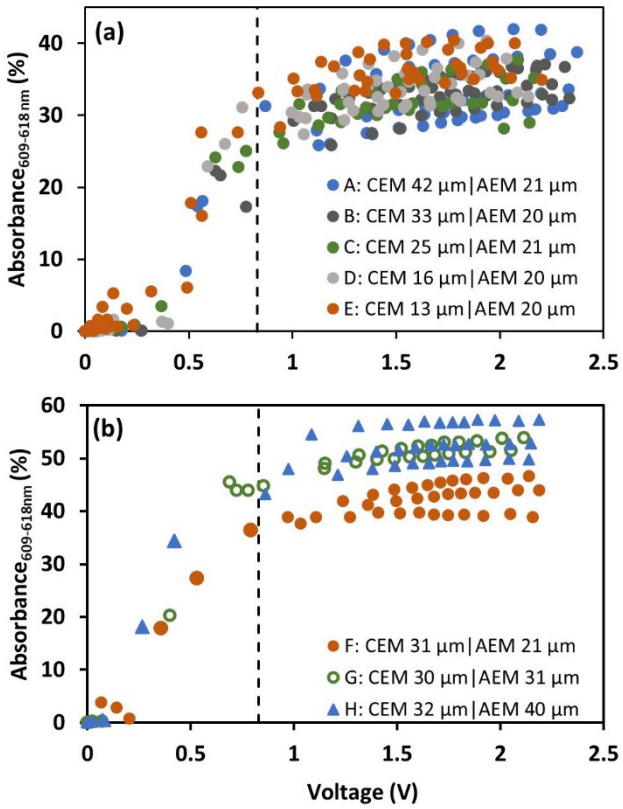

Figure 4.9 **Mean values of potential across various BPM plotted vs. values of absorbance for a single BPM sample in (a) series A - E and (b) series F – H when held at a current density during cell polarization. The dotted lines are at 0.83 V for reference.**

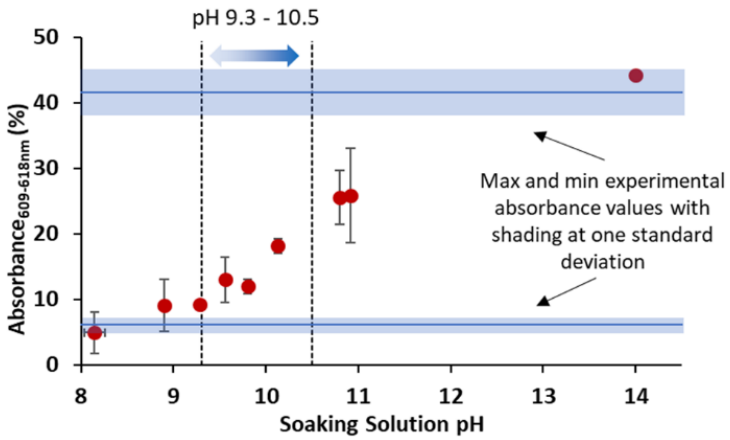

Figure 4.10 **(Red points) The absorbance of pH-indicating hexamethyl-p-terphenyl poly(methylbenzamidazolium) (HMT-PMBI) membranes from batch #1 after soaking in $NaHCO_3/Na_2CO_3$ buffer solutions. The point at pH 14 used a 1 M NaOH soaking solution. Absorbance was measured at room temperature after the polymer had soaked in each solution at least 24 hours. The average maximum and minimum values obtained experimentally from series A – E, at 0 and 30 mA cm^{-2}, respectively, are shown at solid lines with shaded error bars at one standard deviation. Note that thymolphthalein typically changes color between pH 9.3 – 10.5. Membranes used range in thickness from 19 – 24 µm.**

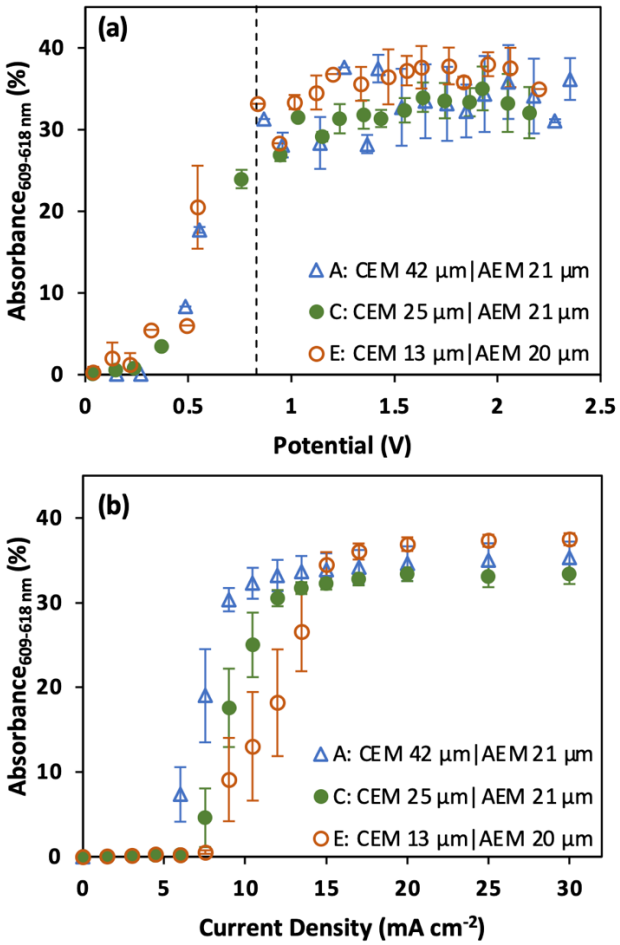

Figure 4.9 **(a) Average absorbance vs potential for BPMs in series A, C, and E. Individual absorbance measurements are plotted in figure 8. Absorbances shown are averages of 0.1 V increments with error bars at one standard deviation. (b) Average absorbance vs current density for BPMs in series A, C, and E with error bars are at one standard error.**

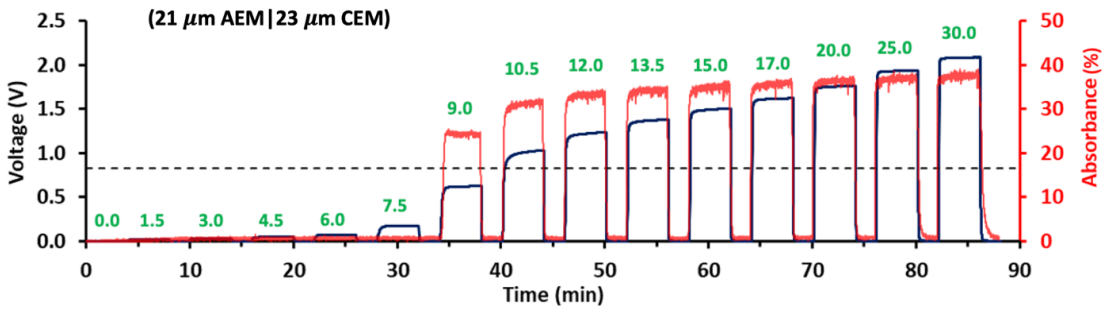

Figure 4.10 **The voltage (dark blue) across the membrane and absorbance (red) of BPM C3 consisting of 21 µm hexamethyl-p-terphenyl poly(methylbenzamidazolium) (HMT-PMBI) and 23 µm sulfonated phenylated polyphenylene with a biphenyl linker unit (SPPB) vs. time, as a function of current density. The numbers in green above each voltage step show the current density in mA cm^{-2} which was applied across the BPM. Between each current density hold the current was dropped to 0 mA cm^{-2} for two minutes. The horizontal dotted line across the graph is at 0.83 V.**

From these studies I conclude, the theoretical standard water dissociation potential of 0.83 V has limited meaning when interpreting four-electrode BPM polarization curves, as this potential is derived from the Nernst equation (equation 4) and describes only the potential drop across the junction for standard state conditions. The discrepancy between the theoretical dissociation potential and the onset potential for water dissociation (as revealed by the pH indicator) likely occurs for two reasons. This first is that the junction potential cannot be separated from contributions of the Donnan potentials at each solution|membrane interface as illustrated in figure 1. When the anolyte and catholyte in contact with the reference electrode consist of the same solution the potential drop across the membrane is equal to zero. This is the case at open circuit potential. Once water dissociation occurs within the interface of the BPM, H^+ and OH^- generated migrate to the catholyte and anolyte, respectively, thereby changing the pH of the solutions close to the membrane|solution interface and thus, the cross-membrane potential. Secondly, the rate of water dissociation is dependent on the strong electric field formed at the interface of the AEM and CEM. Similar to the electric field formed in a parallel plate capacitor, the strength of this field is dependent on the magnitude of the positive and negative charge. In the case of an ion exchange membrane, this charge originates from the positive and negative fixed charge groups of the AEM and CEM, in

this case, quaternary amine and sulfonic acid sites. The contribution of water dissociation to the total current increases as the BPM interfacial electric field strength increases, thus increasing the rate of water dissociation. Therefore, the contribution of water dissociation depends on the number of fixed charge groups at the interface. The theoretical water dissociation potential assumes standard state conditions and a proton and hydroxide activity of unity within the CEM and AEM respectively. When using membranes which differ in structure and/or ion exchange capacities, this assumption is no longer valid.[171,172]

4.3.4. Electrochemical Impedance Spectroscopy

EIS was also used to probe simultaneous water dissociation and co-ion leakage currents occurring in BPMs at different current densities and with varying CEM and AEM thickness, corresponding Bode plots are shown in figure 4.13. These plots exhibit a low and high frequency feature at approximately 10 mHz and 1000 Hz, respectively. These results are in good agreement with the reports by Blommaert et. al. who, using a similar experimental set-up, collected EIS data of BPMs (albeit based on different ion exchange membranes) in the presence and absence of co-ions.[173] The authors were able to convincingly attribute the low and high frequency feature to co-ion leakage and water dissociation reaction, respectively.

A representative Bode plot is shown in figure 4.13 (a) and reveals a transition from co-ion leakage (low frequency) to water dissociation (high frequency) which is dependent on the thickness of the CEM. At an applied current of 12 mA cm^{-2}, the BPM with the thinnest CEM layer shows no high frequency feature indicating that the current is passed is largely due to co-ion leakage. As the CEM thickness is increased, a greater percentage of the current passed is due to water dissociation. By contrast, the Bode plots in figure 4.13 (b) reveal little variation as AEM thickness is increased. This provides further evidence that the contribution of co-ion leakage to the overall current density depends on the relationship between permselectivity and thickness of the AEM and CEM. Bode and Nyquist plots for BPMs studied in this work, at several different current

densities, are provided in figures S14-S7. Tables 4-3 and 4-4 provide an analysis of the high frequency features present in the Bode plots.

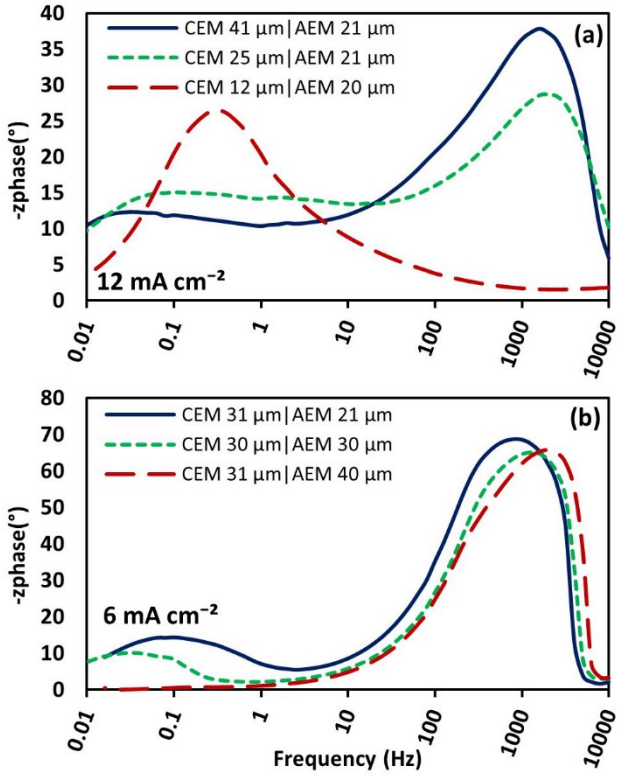

Figure 4.11 **Bode plots comparing, (a) BPMs of varying CEM thickness when a direct current of 12 mA cm^{-2} is drawn, and (b) BPMs of varying AEM thickness when a direct current of 6 mA cm^{-2} is drawn. For details, see the experimental section.**

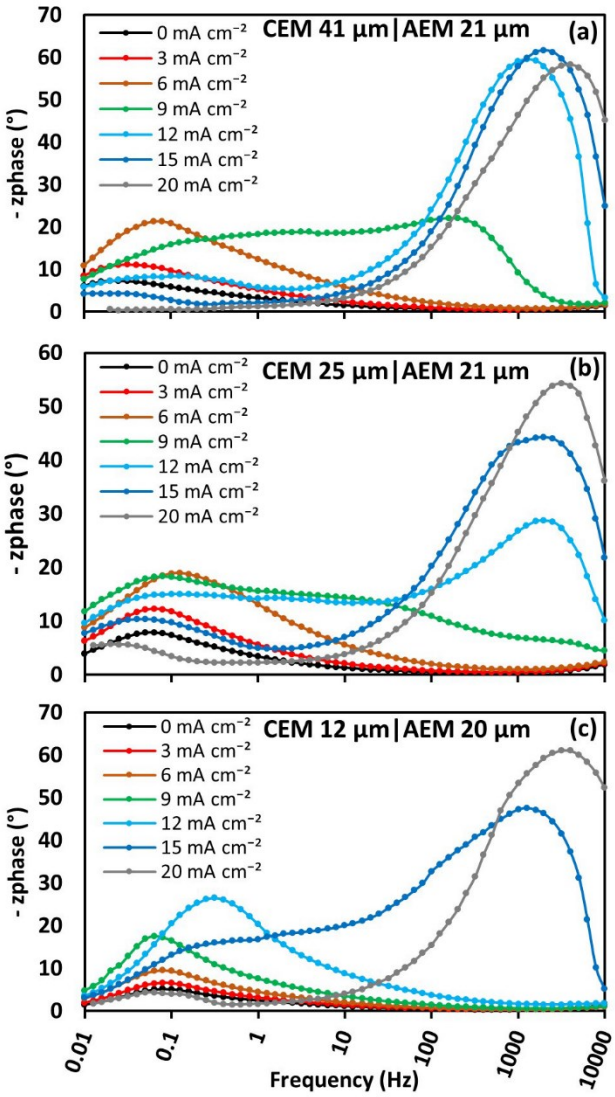

Figure 4.12 **Z-phase component of Bode plots obtained from EIS measurements for BPMs in series A (b), C (b), and E (c) at different applied direct currents. The applied alternating current was half of the direct current. The alternating current applied at 0 mA cm^{-2} was 2 mA cm^{-2}. EIS was performed at room temperature in a 4-electrode cell with 0.5 M Na_2SO_4 circulating through the both compartments.**

Table 4-3 **Analysis of the high-frequency features for samples A2, C2, and F2. The applied direct current is shown with the -z phase maximum, the frequency at which the maximum occurs, and the DC voltage component of the measured voltage at the frequency shown.**

Sample	j DC (mA cm^{-2})	High-frequency -z phase maximum (°)	Frequency (Hz)	Voltage (V)
A2 CEM 41 µm | AEM 21 µm	9	22.1	158	0.22
	12	59.5	1258	0.66
	15	61.7	1979	1.12
	20	58.3	4002	1.68
C2 CEM 25 µm | AEM 21 µm	12	28.7	1979	0.28
	15	44.3	1979	0.58
	20	54.3	3164	1.40
E2 CEM 12 µm | AEM 20 µm	15	47.6	1258	0.46
	20	61.1	2507	1.63

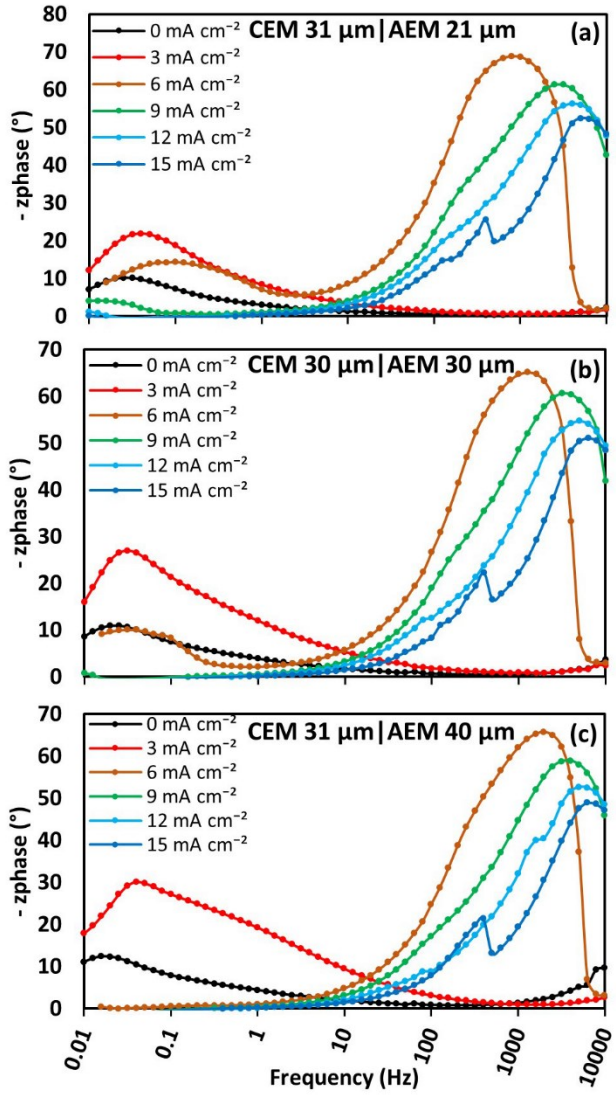

Figure 4.13 **Z-phase component of Bode plots obtained from EIS measurements for BPMs in series F (b), G (b), and H (c) at different applied direct currents. The applied alternating current was half of the direct current. The alternating current applied at 0 mA cm^{-2} was 2 mA cm^{-2}. EIS was performed at room temperature in a 4-electrode cell with 0.5 M Na_2SO_4 circulating through the both compartments.**

Table 4-4 **Analysis of the high-frequency features for samples F1, G1, and H1. The applied direct current is shown with the -z phase maximum, the frequency at which the maximum occurs, and the DC voltage component of the measured voltage at the frequency shown.**

Sample	j DC (mA cm^{-2})	High-frequency -z phase maximum (°)	Frequency (Hz)	Voltage (V)
F1 CEM 31 µm | AEM 21 µm	6	68.8	800	0.65
	9	61.3	3164	1.48
	12	56.3	4002	1.74
	15	52.4	5039	1.91
G1 CEM 30 µm | AEM 30 µm	6	65.2	1258	0.71
	9	60.6	3164	1.42
	12	54.7	5039	1.71
	15	51.0	6288	1.87
H1 CEM 31 µm | AEM 40 µm	6	65.7	1979	0.94
	9	58.9	4002	1.48
	12	52.6	5039	1.78
	15	48.9	6288	1.93

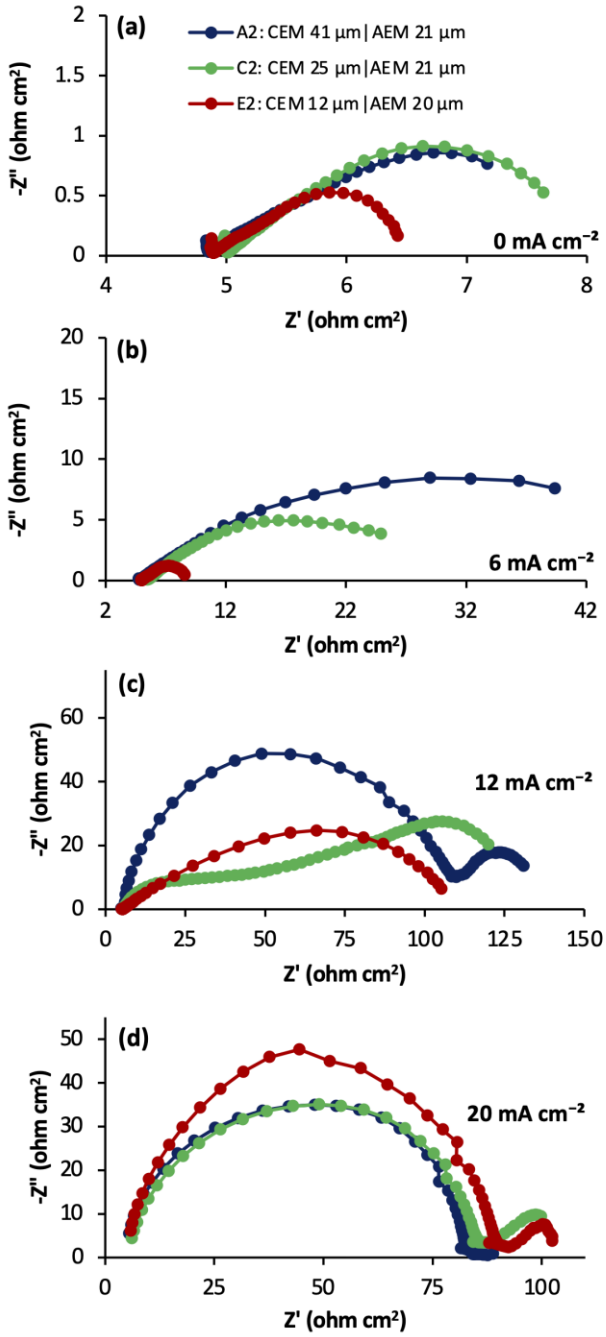

Figure 4.14 **Nyquist plots for BPM samples A2, C2, and E2 at 0, 6, 12, and 20 mA cm^{-2} applied direct current. The applied alternating current was half of the direct current. The alternating current applied at 0 mA cm^{-2} was 2 mA cm^{-2}. EIS was performed at room temperature in a 4-electrode cell with 0.5 M Na_2SO_4 circulating through the both compartments.**

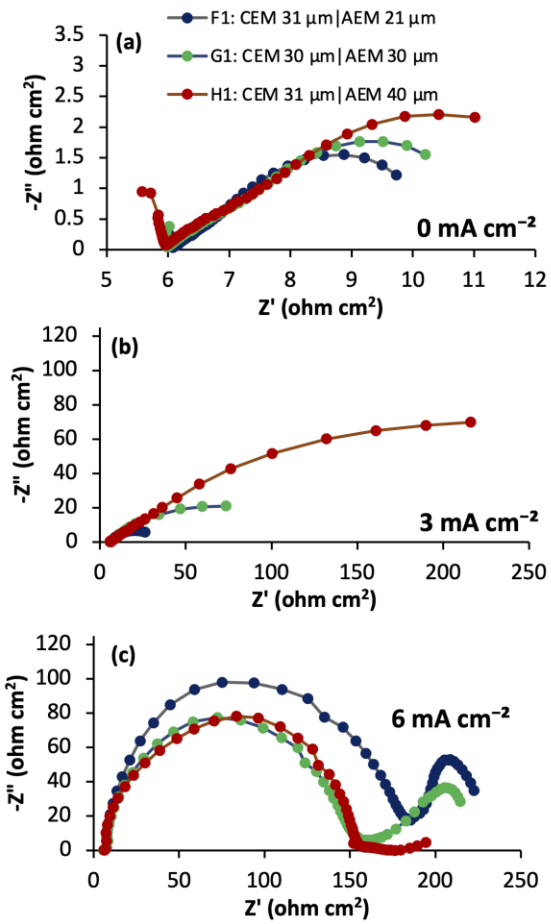

Figure 4.15 Nyquist plots for BPM samples F1, G1, and H1 at 0, 3, and 6 mA cm^{-2} applied direct current. The applied alternating current was half of the direct current. The alternating current applied at 0 mA cm^{-2} was 2 mA cm^{-2}. EIS was performed at room temperature in a 4-electrode cell with 0.5 M Na_2SO_4 circulating through the both compartments.

4.4. Conclusion

This work confirms that water dissociation occurs at relatively low cross-membrane potentials, below 0.5 V, in bipolar membranes, even in the absence of a water dissociation catalyst. This is proven using a novel spectroelectrochemical method which allows for membrane potential and absorbance to be measured simultaneously. Previous experiments have utilized ICP-MS to analyze anolyte and catholyte solutions and quantify co-ion leakage currents. If the co-ion leakage is known over a certain period of time and at fixed current density, the rate of water dissociation is implied. The spectroelectrochemical method employed in this work provides direct evidence of the

water dissociation reaction and is immediately responsive to changes in voltage or potential. Additionally, this method is not dependent on changes to the electrolyte solution.

Two fully-hydrocarbon ion exchange membranes were used in this study. By characterizing samples with AEM and CEM layers of varying thickness, it was found that the thickness of the SPPB (CEM) layer played a greater role in determine the current-voltage characteristics and co-ion leakage currents. This is due to the low permselectivity of SPPB, due to its high-water volume content, which is more highly dependent on thickness than that of HMT-PMBI. EIS analysis confirms water dissociation at relatively low current densities. By comparing samples with different bulk thicknesses of the AEM and CEM layers, it was observed that the co-ion leakage currents are dependent on the thickness of the SPPB but not HMT-PMBI bulk layers.

Chapter 5.

Conclusions and Future Directions

5.1. Conclusions

5.1.1. Mono-pH Water Electrolysis

Chapter 2 of this thesis examined water electrolysis occurring in mono-pH systems utilizing either a proton exchange membrane (PEM) or an anion exchange membrane (AEM) for acidic or basic systems, respectively. This work investigated two novel hydrocarbon ion exchange materials in water electrolysis devices as a proof of concept.

In section 2.1, a PEM, sulfonated poly(arylene ether) (SPAE), is used as the bulk membrane material in a water electrolysis cell. The SPAE membrane functioned in a water electrolyzer, but at voltages much higher than a similar cell utilizing a commercially available Nafion membrane. Much of the poor performance is attributed to highly resistive titanium cell hardware which lead to a high ohmic resistance. This high resistance was confirmed by electrochemical impedance spectroscopy (EIS). Post-mortem analysis of the cell revealed delamination of the catalyst layers from the SPAE membrane due to incompatibility of the Nafion ionomer and hydrocarbon material. This work made evident both the engineering challenges that exist when constructing such electrochemical devices, and the importance of good adhesion between the catalyst layer and membrane in the membrane-electrode assembly.

In section 2.2, two poly(bis-arylimidazolium) polymers were used as both the ionomer in the catalyst layer, and the bulk membrane in water electrolysis cells. The excellent stabilities of both polymers were demonstrated by operation with 6 M KOH electrolyte fed to both the anode and cathode. Notably, PAImEE shows excellent stability when run in an electrolyzer at 400 mA cm^{-2} for 48 hours in 6 M KOH.

5.1.2. Bipolar Membrane Water Electrolysis

In this thesis, bipolar membranes were fabricated from two hydrocarbon polymers, sulfonated phenylated polyphenylene(biphenyl) (SPPB), and hexamethyl-p-terphenyl poly(benzimidazole) (HMT-PMBI).

In Chapter 3, the role of the interfacial layer was explored through the fabrication of four BPMs with identical AEM and CEM bulk layers, but different interfaces. Results confirmed the better performance of a high surface area 3D junction vs. a 2D junction, and the advantage of incorporating $Al(OH)_3$ as a water dissociation catalyst. Variation in the measured open circuit potential suggested a certain dependence of co-ion leakage on both interfacial morphology and the inclusion of a water dissociation catalyst.

Throughout this work, BPMs which contained $Al(OH)_3$ between bulk SPPB and HMT-PMBI layers routinely delaminated while those with no catalyst did not. Without a water dissociation catalyst, it seemed sufficient electrostatic interaction existed to prevent the delamination of SPPB and HMT-PMBI. It was postulated that this poor adhesion resulted from the high glass transition temperature of both HMT-PMBI and SPPB which inhibited proper coalescence of the two polymers during fabrication by hot-pressing.

In Chapter 4 the role of bulk layer thickness on the performance of BPMs was explored. Polarization curves showed that the co-ion leakage current was dependent on the thickness of the CEM, which was varied from 13 μm to 42 μm, but not dependent on AEM thickness, which was varied from 21 μm to 40 μm. This is because the permselectivity of SPPB is more thickness dependent than HMT-PMBI as shown by measurements of the apparent permselectivity.

Water dissociation at potentials below 0.5 V was confirmed using a novel spectroelectrochemical approach. HMT-PMBI was co-cast with a pH indicator, thymolphthalein. Electrochemical measurements were performed in a quartz cell while the visible color change associated with the pH indicator was measured simultaneously. In this way it was possible to visually confirm the water dissociation reaction as the indicator changed color when the hydroxide ions formed at the interface migrate into the AEM.

5.2. Future Directions

5.2.1. Water Electrolysis

The viability of water electrolysis depends heavily on the ability to use abundant, low-cost catalyst materials in conjunction with robust hydrocarbon membranes. PEM water electrolysis solves many of the problems associated with traditional alkaline electrolyzers by replacing the liquid electrolyte with a solid polymer electrolyte. However, operation under acidic conditions requires platinum group metals to catalyze the hydrogen and oxygen evolution reactions. Progress has been made in exploring non-precious metals for the oxygen and hydrogen evolution reactions but Pt and Ir remain the most active catalysts.[174] Further computational and experimental studies are needed to continue to improve catalyst activity.

Another issue with current PEM water electrolysis is the use of fluorinated membranes and ionomer. This makes hydrocarbon membranes vital for further commercializing PEM water electrolyzers. Recent reports show hydrocarbon membranes with superior performance to Nafion. However, durability data is rarely presented.[175] Excellent membrane durability is crucial for PEM WE operation. Because of the time necessary to complete galvanostatic durability studies, a standard accelerated stress test must be developed. Several protocols have been put forward but no standard protocol has been adopted.[176,177] In addition to standardizing AST procedures, it has been argued that testing hardware must also be standardized.[176] Chapter 2.1 of this thesis supports this claim, as it shows the large impact poor hardware has on cell performance. While the work presented in chapter 2.1 is a good starting point for understanding how sulfonated poly(arylene ether) behaves in a water electrolyzer, characterization of an MEA utilizing the polymer in the ionomer is necessary, as well as performing durability and accelerated stress testing. Additionally, hydrogen crossover data should be reported.

Using AEMs for water electrolysis allows for use of non-precious metal catalysts while retaining most of the desirable properties of PEM water electrolyzers such as fast load cycling and operation at differential pressures. Many of the obstacles facing AEM and PEM WE are similar, however, AEM WE technology is less established than PEM

WE. The largest obstacle to the widespread adoption of AEM water electrolyzers has been the chemical stability of the membranes and ionomer in base as previously discussed in this thesis. Though significant progress has been made in developing stable polymers, further improvements in stability, conductivity, and mechanical stability are needed. Further development of catalysts is also needed. Despite touting the ability to use non-noble catalysts, many studies still chose to use noble metal, particularly for the cathode as the HER is more sluggish in base than acid.

Similar to PEM WE, a standard accelerated stress test for AEM WE should be developed. Potential cycling between 1.0 V and 1.8 V was used by Zignani et al. as an AST to characterize a Sustanion membrane with a NiFeO anode and Pt/C cathode.[178] A standardized testing procedure and standardized hardware is necessary for proper comparison of new and commercially available membranes. In a review of commercially available AEMs for water electrolysis by Henkensmeier et al., the authors note the difficulty in drawing conclusions from currently available work which uses a multitude of different catalysts, hardware, liquid electrolytes, temperatures, and testing procedures.[179]

The work presented in chapter 2.2 of this thesis demonstrates the excellent chemical stability of poly(bis-arylimidazolium) with ethyl and butyl groups at the N1/N3 positions by operating the cells in 6 M KOH. Future work should include operation of the cells in conditions more typical for AEM WE such as circulation of 0.1 M and 1.0 M KOH. Accelerated stress testing and hydrogen gas crossover experiments should also be performed.

5.2.2. Bipolar Membranes

In regard to improving bipolar membrane performance, I will discuss recommended future directions from three perspectives: (1) the AEM and CEM (or PEM) polymers with regard to bulk conductivity, water permeability, and ion crossover, (2) the optimization of the interfacial layer, and (3) fabrication methods.

There is a strong interplay between many the physical characteristics of ion exchange polymers. The ideal membranes for use in a BPM would require an almost conflicting set of properties. Membranes should have high ion conductivities and high

water permeability, yet remain insoluble in aqueous solution and highly permselective for cation or anions. These requirements are similar to the desirable properties for polymers in mono-pH water electrolysis described above. However, BPMs require better water transport to supply the reactant water to the interfacial layer. High permselectivity is also needed to prevent co-ion leakage as explored in chapter 4. Further polymer development is needed for both AEMs and CEMs with these requirements in mind.

Optimization of the interfacial layer is needed to increase the efficiency of the water dissociation reaction. This can be achieved by altering the geometry of the interface and through the addition of water dissociation catalysts. Increasing the interfacial layer surface area has been explored through the use of electrospinning as shown in previous literature and chapter 3 of this thesis.[79,180] The addition of a water dissociation catalyst dramatically improves the water dissociation efficiency at the interfacial layer.[86,180,181] Oener et al. developed a high performance BPM by creating a catalyst bilayer with two catalysts designed specifically for the pH gradient across the interfacial layer.[86] In this work Oener also finds that the overpotential of water dissociation reaction is decreased by the addition of electrically conducting, semiconducting and insulating metal oxides suggesting that water dissociation is more greatly influenced by the presence of a catalyst material than the electric field enhancement. Thus, future work optimizing the interfacial layer should focus more on catalysis rather than increasing surface area.

The fabrication of bipolar membranes is important as it may determine the properties of the interfacial layer. In chapter 3 of this thesis, it is discovered that hot-pressing does not adequately adhere the sulfonated phenylated polyphenylene (biphenyl) (SPPB) and hexamethyl-p-terphenyl poly(benzimidazole) (HMT-PMBI) polymers causing delamination of the layers. It is likely that the high glass transition temperatures of these polymers prevent proper coalescence. Because of this, the BPMs in chapter 4 are prepared without a water dissociation catalyst. Other fabrication methods for BPMs utilizing SPPB and HMT-PMBI have been attempted with limited success. These include casting or spray coating successive layers. However, the polymers show similar solubility in common solvents which leads to mixing of the AEM and CEM layers. It may also be possible to construct zero-gap type cells in which the AEM and CEM layers are forced into contact by external hardware. While this suffices for lab scale experiments, proper

adhesion seems necessary for a commercially available BPM. Given the importance of a water dissociation catalyst in the interfacial layer and good adhesion between the layers, it is necessary to develop a method for fabricating a BPM when both polymers exhibit a high glass transition temperature and similar solubility is common solvents.

References

(1) Ansari, D.; Holz, F.; Al-Kuhlani, H. *Energy, Climate, and Policy towards 2055: An Interdisciplinary Energy Outlook (DIW-REM Outlook)*; Berlin, 2019.

(2) IEA. *Net Zero by 2050*; Paris, 2021.

(3) Dodds, P. E.; Garvey, S. D. The Role of Energy Storage in Low-Carbon Energy Systems. In *Storing Energy with Special Reference to Renewable Energy Sources*; Letcher, T. M., Ed.; Elsevier Inc.: Cambridge, 2016; pp 4–6.

(4) Abe, J. O.; Popoola, A. P. I.; Ajenifuja, E.; Popoola, O. M. Hydrogen Energy, Economy and Storage: Review and Recommendation. *Int. J. Hydrogen Energy* **2019**, *44* (29), 15072–15086. https://doi.org/10.1016/j.ijhydene.2019.04.068.

(5) Tichler, R.; Bauer, S. Power-to-Gas. In *Storing Energy with Special Reference to Renewable Energy Sources*; Letcher, T. M., Ed.; Elsevier Inc.: Cambridge, 2016.

(6) Andrews, J.; Shabani, B. Re-Envisioning the Role of Hydrogen in a Sustainable Energy Economy. *Int. J. Hydrogen Energy* **2012**, *37* (2), 1184–1203. https://doi.org/10.1016/j.ijhydene.2011.09.137.

(7) Cano, Z. P.; Banham, D.; Ye, S.; Hintennach, A.; Lu, J.; Fowler, M.; Chen, Z. Batteries and Fuel Cells for Emerging Electric Vehicle Markets. *Nat. Energy* **2018**, *3* (4), 279–289. https://doi.org/10.1038/s41560-018-0108-1.

(8) Cullen, D. A.; Neyerlin, K. C.; Ahluwalia, R. K.; Mukundan, R.; More, K. L.; Borup, R. L.; Weber, A. Z.; Myers, D. J.; Kusoglu, A. New Roads and Challenges for Fuel Cells in Heavy-Duty Transportation. *Nat. Energy* **2021**, *6* (5), 462–474. https://doi.org/10.1038/s41560-021-00775-z.

(9) Hwang, H. T.; Varma, A. Hydrogen Storage for Fuel Cell Vehicles. *Curr. Opin. Chem. Eng.* **2014**, *5*, 42–48. https://doi.org/10.1016/j.coche.2014.04.004.

(10) IEA. *The Future of Hydrogen*; Paris, 2019. https://doi.org/10.1787/1e0514c4-en.

(11) Cheng, X.; Shi, Z.; Glass, N.; Zhang, L.; Zhang, J.; Song, D.; Liu, Z. S.; Wang, H.; Shen, J. A Review of PEM Hydrogen Fuel Cell Contamination: Impacts, Mechanisms, and Mitigation. *J. Power Sources* **2007**, *165* (2), 739–756. https://doi.org/10.1016/j.jpowsour.2006.12.012.

(12) *PEM Electrolysis for Hydrogen Production*, 1st ed.; Bessarabov, D., Wang, H., Li, H., Zhao, N., Eds.; CRC Press: Boca Raton, 2016.

(13) Li, C.; Baek, J. B. The Promise of Hydrogen Production from Alkaline Anion Exchange Membrane Electrolyzers. *Nano Energy* **2021**, *87* (February), 106162. https://doi.org/10.1016/j.nanoen.2021.106162.

(14) Cheng, H.; Scott, K.; Ramshaw, C. Intensification of Water Electrolysis in a Centrifugal Field. *J. Electrochem. Soc.* **2002**, *149* (11), D172. https://doi.org/10.1149/1.1512916.

(15) Carmo, M.; Fritz, D. L.; Mergel, J.; Stolten, D. A Comprehensive Review on PEM Water Electrolysis. *Int. J. Hydrogen Energy* **2013**, *38*, 4901–4934. https://doi.org/10.1016/j.ijhydene.2013.01.151.

(16) Miller, H. A.; Bouzek, K.; Hnat, J.; Loos, S.; Bernäcker, C. I.; Weißgärber, T.; Röntzsch, L.; Meier-Haack, J. Green Hydrogen from Anion Exchange Membrane Water Electrolysis: A Review of Recent Developments in Critical Materials and Operating Conditions. *Sustain. Energy Fuels* **2020**, *4* (5), 2114–2133. https://doi.org/10.1039/c9se01240k.

(17) Keçebaş, A.; Kayfeci, M.; Bayat, M. Electrochemical Hydrogen Generation. In *Solar Hydrogen Production: Processes, Systems and Technologies*; Elsevier Science & Technology: San Diego, 2019; pp 299–317. https://doi.org/10.1016/B978-0-12-814853-2.00009-6.

(18) Jensen, J. O.; Bandur, V.; Bjerrum, N. J.; Jensen, S. H.; Ebbesen, S.; Mogensen, M.; Tophøj, N.; Yde, L. *Pre-Investigation of Water Electrolysis*; 2006.

(19) Alkaline Water Electrolysis https://denora.com/products/applications/energy-storage/alkaline-water-electrolysis.html (accessed Sep 15, 2021).

(20) Bensmann, B.; Hanke-Rauschenbach, R.; Peña Arias, I. K.; Sundmacher, K. Energetic Evaluation of High Pressure PEM Electrolyzer Systems for Intermediate Storage of Renewable Energies. *Electrochim. Acta* **2013**, *110*, 570–580. https://doi.org/10.1016/j.electacta.2013.05.102.

(21) Vincent, I.; Bessarabov, D. Low Cost Hydrogen Production by Anion Exchange Membrane Electrolysis: A Review. *Renew. Sustain. Energy Rev.* **2018**, *81* (August 2016), 1690–1704. https://doi.org/10.1016/j.rser.2017.05.258.

(22) Varcoe, J. R.; Atanassov, P.; Dekel, D. R.; Herring, A. M.; Hickner, M. A.; Kohl, P. A.; Kucernak, A. R.; Mustain, W. E.; Nijmeijer, K.; Scott, K.; Xu, T.; Zhuang, L. Anion-Exchange Membranes in Electrochemical Energy Systems. *Energy Environ. Sci.* **2014**, *7* (10), 3135–3191. https://doi.org/10.1039/c4ee01303d.

(23) Xu, J.; Sheng, G. P.; Luo, H. W.; Li, W. W.; Wang, L. F.; Yu, H. Q. Fouling of Proton Exchange Membrane (PEM) Deteriorates the Performance of Microbial Fuel Cell. *Water Res.* **2012**, *46* (6), 1817–1824.

https://doi.org/10.1016/j.watres.2011.12.060.

(24) Sata, T. *Ion Exchange Membranes: Preparation, Characterization, Modification and Application*; The Royal Society of Chemistry: Cambridge, 2004.

(25) Tanaka, Y. *Ion Exchange Membranes: Fundamentals and Applications*, Second Edi.; Elsevier B.V: Amsterdam, 2015.

(26) Peighambardoust, S. J.; Rowshanzamir, S.; Amjadi, M. *Review of the Proton Exchange Membranes for Fuel Cell Applications*; Elsevier Ltd, 2010; Vol. 35. https://doi.org/10.1016/j.ijhydene.2010.05.017.

(27) Rikukawa, M.; Sanui, K. Proton-Conducting Polymer Electrolyte Membranes Based on Hydrocarbon Polymers. *Prog. Polym. Sci.* **2000**, *25* (10), 1463–1502. https://doi.org/10.1016/S0079-6700(00)00032-0.

(28) Gebel, G. Structural Evolution of Water Swollen Perfluorosulfonated Ionomers from Dry Membrane to Solution. *Polymer (Guildf).* **2000**, *41* (15), 5829–5838. https://doi.org/10.1016/S0032-3861(99)00770-3.

(29) Sone, Y.; Ekdung, P.; Simonsson, D. Proton Conductivity of Nafion 117 as Measured by a Four-Electrode AC Impedance Method. *J. Electrochem. Soc.* **1996**, *143* (4), 1254. https://doi.org/10.1149/1.1836625.

(30) Osborn, S. J.; Hassan, M. K.; Divoux, G. M.; Rhoades, D. W.; Mauritz, K. A.; Moore, R. B. Glass Transition Temperature of Perfluorosulfonic Acid Ionomers. *Macromolecules* **2007**, *40* (10), 3886–3890. https://doi.org/10.1021/ma062029e.

(31) Chen, S. L.; Krishnan, L.; Srinivasan, S.; Benziger, J.; Bocarsly, A. B. Ion Exchange Resin/Polystyrene Sulfonate Composite Membranes for PEM Fuel Cells. *J. Memb. Sci.* **2004**, *243* (1–2), 327–333. https://doi.org/10.1016/j.memsci.2004.06.037.

(32) Wei, G.; Xu, L.; Huang, C.; Wang, Y. SPE Water Electrolysis with SPEEK/PES Blend Membrane. *Int. J. Hydrogen Energy* **2010**. https://doi.org/10.1016/j.ijhydene.2010.05.041.

(33) Kaliaguine, S.; Mikhailenko, S. D.; Wang, K. P.; Xing, P.; Robertson, G.; Guiver, M. Properties of SPEEK Based PEMs for Fuel Cell Application. *Catal. Today* **2003**, *82* (1–4), 213–222. https://doi.org/10.1016/S0920-5861(03)00235-9.

(34) Marangio, F.; Pagani, M.; Santarelli, M.; Calì, M. Concept of a High Pressure PEM Electrolyser Prototype. *Int. J. Hydrogen Energy* **2011**, *36* (13), 7807–7815. https://doi.org/10.1016/j.ijhydene.2011.01.091.

(35) Asensio, J. A.; Sánchez, E. M.; Romero, P. G. Proton-Conducting Membranes Based on Benzimidazole Polymers for High-Temperature PEM Fuel Cells. A Chemical Quest. *Chem. Soc. Rev.* **2010**, *39* (8), 3210–3239. https://doi.org/10.1039/b922650h.

(36) Kostalik, H. A.; Clark, T. J.; Robertson, N. J.; Mutolo, P. F.; Longo, J. M.; Abruña, H. D.; Coates, G. W. Solvent Processable Tetraalkylammonium-Functionalized Polyethylene for Use as an Alkaline Anion Exchange Membrane. *Macromolecules* **2010**, *43* (17), 7147–7150. https://doi.org/10.1021/ma101172a.

(37) Zhang, M.; Kim, H. K.; Chalkova, E.; Mark, F.; Lvov, S. N.; Chung, T. C. M. New Polyethylene Based Anion Exchange Membranes (PE-AEMs) with High Ionic Conductivity. *Macromolecules* **2011**, *44* (15), 5937–5946. https://doi.org/10.1021/ma200836d.

(38) Hickner, M. A.; Herring, A. M.; Coughlin, E. B. Anion Exchange Membranes: Current Status and Moving Forward. *J. Polym. Sci. Part B Polym. Phys.* **2013**, *51* (24), 1727–1735. https://doi.org/10.1002/polb.23395.

(39) Ko, B. S.; Sohn, J. Y.; Shin, J. Radiation-Induced Synthesis of Solid Alkaline Exchange Membranes with Quaternized 1,4-Diazabicyclo[2,2,2] Octane Pendant Groups for Fuel Cell Application. *Polymer (Guildf).* **2012**, *53* (21), 4652–4661. https://doi.org/10.1016/j.polymer.2012.08.002.

(40) Qaisrani, N. A.; Ma, L.; Hussain, M.; Liu, J.; Li, L.; Zhou, R.; Jia, Y.; Zhang, F.; He, G. Hydrophilic Flexible Ether Containing, Cross-Linked Anion-Exchange Membrane Quaternized with DABCO. *ACS Appl. Mater. Interfaces* **2020**, *12* (3), 3510–3521. https://doi.org/10.1021/acsami.9b15435.

(41) Chen, D.; Hickner, M. A. Degradation of Imidazolium- and Quaternary Ammonium-Functionalized Poly(Fluorenyl Ether Ketone Sulfone) Anion Exchange Membranes. *ACS Appl. Mater. Interfaces* **2012**, *4* (11), 5775–5781. https://doi.org/10.1021/am301557w.

(42) Deavin, O. I.; Murphy, S.; Ong, A. L.; Poynton, S. D.; Zeng, R.; Herman, H.; Varcoe, J. R. Anion-Exchange Membranes for Alkaline Polymer Electrolyte Fuel Cells: Comparison of Pendent Benzyltrimethylammonium- and Benzylmethylimidazolium-Head- Groups. *Energy Environ. Sci.* **2012**, *5* (9), 8584–8597. https://doi.org/10.1039/c2ee22466f.

(43) Fan, J.; Willdorf-cohen, S.; Schibli, E. M.; Paula, Z.; Li, W.; Skalski, T. J. G.; Sergeenko, A. T.; Hohenadel, A.; Frisken, B. J.; Magliocca, E.; Mustain, W. E.; Diesendruck, C. E.; Dekel, D. R.; Holdcroft, S. Poly(Bis-Arylimidazoliums) Possessing High Hydroxide Ion Exchange Capacity and High Alkaline Stability. *Nat. Commun.* **2019**, *10* (1), 2306. https://doi.org/10.1038/s41467-019-10292-z.

(44) Lin, X.; Liang, X.; Poynton, S. D.; Varcoe, J. R.; Ong, A. L.; Ran, J.; Li, Y.; Li, Q.; Xu, T. Novel Alkaline Anion Exchange Membranes Containing Pendant Benzimidazolium Groups for Alkaline Fuel Cells. *J. Memb. Sci.* **2013**, *443*, 193–200. https://doi.org/10.1016/j.memsci.2013.04.059.

(45) Pérez-Prior, M. T.; Várez, A.; Levenfeld, B. Synthesis and Characterization of Benzimidazolium-Functionalized Polysulfones as Anion-Exchange Membranes. *J. Polym. Sci. Part A Polym. Chem.* **2015**, *53* (20), 2363–2373. https://doi.org/10.1002/pola.27692.

(46) Wright, A. G.; Fan, J.; Britton, B.; Weissbach, T.; Lee, H.-F.; Kitching, E. A.; Peckham, T. J.; Holdcroft, S. Hexamethyl-p-Terphenyl Poly(Benzimidazolium): A Universal Hydroxide-Conducting Polymer for Energy Conversion Devices. *Energy Environ. Sci.* **2016**, *9* (6), 2130–2142. https://doi.org/10.1039/C6EE00656F.

(47) Wang, J.; Li, S.; Zhang, S. Novel Hydroxide-Conducting Polyelectrolyte Composed of an Poly(Arylene Ether Sulfone) Containing Pendant Quaternary Guanidinium Groups for Alkaline Fuel Cell Applications. *Macromolecules* **2010**, *43* (8), 3890–3896. https://doi.org/10.1021/ma100260a.

(48) Kim, D. S.; Fujimoto, C. H.; Hibbs, M. R.; Labouriau, A.; Choe, Y. K.; Kim, Y. S. Resonance Stabilized Perfluorinated Ionomers for Alkaline Membrane Fuel Cells. *Macromolecules* **2013**, *46* (19), 7826–7833. https://doi.org/10.1021/ma401568f.

(49) Yan, X.; Gu, S.; He, G.; Wu, X.; Zheng, W.; Ruan, X. Quaternary Phosphonium-Functionalized Poly(Ether Ether Ketone) as Highly Conductive and Alkali-Stable Hydroxide Exchange Membrane for Fuel Cells. *J. Memb. Sci.* **2014**, *466*, 220–228. https://doi.org/10.1016/j.memsci.2014.04.056.

(50) Gu, S.; Skovgard, J.; Yan, Y. S. Engineering the van Der Waals Interaction in Cross-Linking-Free Hydroxide Exchange Membranes for Low Swelling and High Conductivity. *ChemSusChem* **2012**, *5* (5), 843–848. https://doi.org/10.1002/cssc.201200057.

(51) Marx, D.; Chandra, A.; Tuckerman, M. E. Aqueous Basic Solutions: Hydroxide Solvation, Structural Diffusion, and Comparison to the Hydrated Proton. *Chem. Rev.* **2010**, *110* (4), 2174–2216. https://doi.org/10.1021/cr900233f.

(52) Inaba, M.; Matsui, Y.; Saito, M.; Tasaka, A.; Fukuta, K.; Watanabe, S.; Yanagi, H. Effects of Carbon Dioxide on the Performance of Anion-Exchange Membrane Fuel Cells. *Electrochem. commun.* **2011**, *5*, 322–325.

(53) Hibbs, M. R.; Hickner, M. A.; Alam, T. M.; McIntyre, S. K.; Fujimoto, C. H.; Cornelius, C. J. Transport Properties of Hydroxide and Proton Conducting

Membranes. *Chem. Mater.* **2008**, *20* (7), 2566–2573. https://doi.org/10.1021/cm703263n.

(54) Hagesteijn, K. F. L.; Jiang, S.; Ladewig, B. P. A Review of the Synthesis and Characterization of Anion Exchange Membranes. *J. Mater. Sci.* **2018**, *53* (16), 11131–11150. https://doi.org/10.1007/s10853-018-2409-y.

(55) Peckham, T. J.; Yang, Y.; Holdcroft, S. Proton Exchange Membranes. In *Proton Exchange Membrane Fuel Cells: Materials Properties and Performance*; Wilkinson, D. P., Zhang, J., Hui, R., Fergus, J., Li, X., Eds.; CRC Press: Boca Raton, 2010; pp 107–190.

(56) Ziv, N.; Dekel, D. R. A Practical Method for Measuring the True Hydroxide Conductivity of Anion Exchange Membranes. *Electrochem. commun.* **2018**, *88* (February), 109–113. https://doi.org/10.1016/j.elecom.2018.01.021.

(57) Cao, X.; Novitski, D.; Holdcroft, S. Visualization of Hydroxide Ion Formation upon Electrolytic Water Splitting in an Anion Exchange Membrane. *ACS Mater. Lett.* **2019**, *1* (3), 362–366. https://doi.org/10.1021/acsmaterialslett.9b00195.

(58) Duan, Q.; Ge, S.; Wang, C. Y. Water Uptake, Ionic Conductivity and Swelling Properties of Anion-Exchange Membrane. *J. Power Sources* **2013**, *243*, 773–778. https://doi.org/10.1016/j.jpowsour.2013.06.095.

(59) Luo, X.; Wright, A.; Weissbach, T.; Holdcroft, S. Water Permeation through Anion Exchange Membranes. *J. Power Sources* **2018**, *375*, 442–451. https://doi.org/10.1016/j.jpowsour.2017.05.030.

(60) *Macromolecules: An Introduction to Polymer Science*; Bovey, F. A., Winslow, F. H., Eds.; Academic Press: London, 1979.

(61) Wright, A. G.; Holdcroft, S. Hydroxide-Stable Ionenes. *ACS Macro Lett.* **2014**, *3* (5), 444–447. https://doi.org/10.1021/mz500168d.

(62) Fan, J.; Wright, A. G.; Britton, B.; Weissbach, T.; Skalski, T. J. G.; Ward, J.; Peckham, T. J.; Holdcroft, S. Cationic Polyelectrolytes, Stable in 10 M KOHaq at 100 °c. *ACS Macro Lett.* **2017**, *6* (10), 1089–1093. https://doi.org/10.1021/acsmacrolett.7b00679.

(63) H., L.; F.D., C.; J., Z.; H.A., G.; A.B., L. Chemical Degradation: Correlations Between Electrolyzer and Fuel Cell Findings. In *Polymer Electrolyte Fuel Cell Durability*; F.N., B., M., I., T.J., S., Eds.; Springer: New York, 2009. https://doi.org/https://doi-org.proxy.lib.sfu.ca/10.1007/978-0-387-85536-3_5.

(64) Gubler, L.; Dockheer, S. M.; Koppenol, W. H. Radical (HO●, H● and HOO●) Formation and Ionomer Degradation in Polymer Electrolyte Fuel Cells. *J.*

Electrochem. Soc. **2011**, *158* (7), B755. https://doi.org/10.1149/1.3581040.

(65) Grigoriev, S. A.; Dzhus, K. A.; Bessarabov, D. G.; Millet, P. Failure of PEM Water Electrolysis Cells: Case Study Involving Anode Dissolution and Membrane Thinning. *Int. J. Hydrogen Energy* **2014**, *39* (35), 20440–20446. https://doi.org/10.1016/j.ijhydene.2014.05.043.

(66) Siracusano, S.; Van Dijk, N.; Backhouse, R.; Merlo, L.; Baglio, V.; Aricò, A. S. Degradation Issues of PEM Electrolysis MEAs. *Renew. Energy* **2018**, *123*, 52–57. https://doi.org/10.1016/j.renene.2018.02.024.

(67) Zhang, S.; Yuan, X.; Wang, H.; Mérida, W.; Zhu, H.; Shen, J.; Wu, S.; Zhang, J. A Review of Accelerated Stress Tests of MEA Durability in PEM Fuel Cells. *Int. J. Hydrogen Energy* **2009**, *34* (1), 388–404. https://doi.org/10.1016/j.ijhydene.2008.10.012.

(68) Gong, M.; Wang, D. Y.; Chen, C. C.; Hwang, B. J.; Dai, H. A Mini Review on Nickel-Based Electrocatalysts for Alkaline Hydrogen Evolution Reaction. *Nano Res.* **2016**, *9* (1), 28–46. https://doi.org/10.1007/s12274-015-0965-x.

(69) Pärnamäe, R.; Mareev, S.; Nikonenko, V.; Melnikov, S.; Sheldeshov, N.; Zabolotskii, V.; Hamelers, H. V. M.; Tedesco, M. Bipolar Membranes: A Review on Principles, Latest Developments, and Applications. *J. Memb. Sci.* **2021**, *617*. https://doi.org/10.1016/j.memsci.2020.118538.

(70) Simons, R.; Khanarian, G. Water Dissociation in Bipolar Membranes: Experiments and Theory. *J. Membr. Biol.* **1978**, *38*, 11–30. https://doi.org/10.1007/BF01875160.

(71) Coster, H. G. L. A Quantitative Analysis of the Voltage-Current Relationships of Fixed Charge Membranes and the Associated Property of "Punch-Through." *Biophys. J.* **1965**, *5* (5), 669–686. https://doi.org/10.1016/S0006-3495(65)86745-5.

(72) Ramírez, P.; Rapp, H. J.; Mafé, S.; Bauer, B. Bipolar Membranes under Forward and Reverse Bias Conditions. Theory vs. Experiment. *J. Electroanal. Chem.* **1994**, *375* (1–2), 101–108. https://doi.org/10.1016/0022-0728(94)03379-X.

(73) Ramírez, P.; Rapp, H. J.; Reichle, S.; Strathmann, H.; Mafé, S. Current-Voltage Curves of Bipolar Membranes. *J. Appl. Phys.* **1992**, *72* (1), 259–264. https://doi.org/10.1063/1.352124.

(74) Grew, K. N.; McClure, J. P.; Chu, D.; Kohl, P. A.; Ahlfield, J. M. Understanding Transport at the Acid-Alkaline Interface of Bipolar Membranes. *J. Electrochem. Soc.* **2016**. https://doi.org/10.1149/2.0941614jes.

(75) Lovreček, B.; Kunst, B. Electrochemical Properties of the Ion-Exchange Membranes Junction. I. *Croat. Chem. Acta* **1962**, *34* (4), 219–229.

(76) Mafe, S.; Ramırez, P.; Alcaraz, A. Electric Field-Assisted Proton Transfer and Water Dissociation at the Junction of a Fixed-Charge Bipolar Membrane. *Chem. Phys. Lett.* **1998**, *294*, 406–412.

(77) Simons, R. Strong Electric Field Effects on Proton Transfer between Membrane-Bound Amines and Water. *Nature* **1979**, *280* (5725), 824–826. https://doi.org/10.1038/280824a0.

(78) Frilette, V. J. Preparation and Characterization of Bipolar Ion-Exchange Membranes. *J. Phys. Chem.* **1956**, *60* (4), 435–439. https://doi.org/10.1021/j150538a013.

(79) Shen, C.; Wycisk, R.; Pintauro, P. N. High Performance Electrospun Bipolar Membrane with a 3D Junction. *Energy Environ. Sci.* **2017**, *10*, 1435–1442. https://doi.org/10.1039/C7EE00345E.

(80) Simons, R. The Origin and Elimination of Water Splitting in Ion Exchange Membranes during Water Demineralisation by Electrodialysis. *Desalination* **1979**, *28* (1), 41–42. https://doi.org/10.1016/S0011-9164(00)88125-4.

(81) Simons, R. Electric Field Effects on Proton Transfer between Ionizable Groups and Water in Ion Exchange Membranes. *Electrochim. Acta* **1984**, *29* (2), 151–158.

(82) Kang, M. S.; Choi, Y. J.; Moon, S. H. Effects of Inorganic Substances on Water Splitting in Ion-Exchange Membranes: II. Optimal Contents of Inorganic Substances in Preparing Bipolar Membranes. *J. Colloid Interface Sci.* **2004**, *273* (2), 533–539. https://doi.org/10.1016/j.jcis.2004.01.051.

(83) McDonald, M. B.; Freund, M. S. Graphene Oxide as a Water Dissociation Catalyst in the Bipolar Membrane Interfacial Layer. *ACS Appl. Mater. Interfaces* **2014**, *6* (16), 13790–13797. https://doi.org/10.1021/am503242v.

(84) Simons, R. Water Splitting in Ion Exchange Membranes. *Electrochim. Acta* **1985**, *30* (3), 275–282. https://doi.org/10.1016/0013-4686(85)80184-5.

(85) Simons, R. Preparation of a High Performance Bipolar Membrane. *J. Memb. Sci.* **1993**, *78* (1–2), 13–23. https://doi.org/10.1016/0376-7388(93)85243-P.

(86) Oener, S. Z.; Foster, M. J.; Boettcher, S. W. Accelerating Water Dissociation in Bipolar Membranes and for Electrocatalysis. *Science (80-.).* **2020**, *369* (6507), 1099–1103. https://doi.org/10.1126/science.aaz1487.

(87) Nagasubramanian, K.; Chlanda, F. P.; Liu, K.-J. Use of Bipolar Membranes for Generation of Acid and Base - an Engineering and Economic Analysis. *J. Memb. Sci.* **1977**, *2*, 109–124. https://doi.org/10.1016/S0376-7388(00)83237-8.

(88) Strathmann, H. Electrodialysis, a Mature Technology with a Multitude of New Applications. *Desalination* **2010**, *264* (3), 268–288. https://doi.org/10.1016/j.desal.2010.04.069.

(89) Vargas-Barbosa, N. M.; Geise, G. M.; Hickner, M. A.; Mallouk, T. E. Assessing the Utility of Bipolar Membranes for Use in Photoelectrochemical Water-Splitting Cells. *ChemSusChem* **2014**, *7* (11), 3017–3020. https://doi.org/10.1002/cssc.201402535.

(90) McDonald, M. B.; Ardo, S.; Lewis, N. S.; Freund, M. S. Use of Bipolar Membranes for Maintaining Steady-State PH Gradients in Membrane-Supported, Solar-Driven Water Splitting. *ChemSusChem* **2014**, *7* (11), 3021–3027. https://doi.org/10.1002/cssc.201402288.

(91) Vermaas, D. A.; Sassenburg, M.; Smith, W. A. Photo-Assisted Water Splitting with Bipolar Membrane Induced PH Gradients for Practical Solar Fuel Devices. *J. Mater. Chem. A* **2015**, *3* (38), 19556–19562. https://doi.org/10.1039/C5TA06315A.

(92) Liu, X.; Yang, H.; Dai, H.; Mao, X.; Liang, Z. A Novel Photoelectrocatalytic Approach for Water Splitting by an I-BiOCl/Bipolar Membrane Sandwich Structure. *Green Chem.* **2015**, *17* (1), 199–203. https://doi.org/10.1039/c4gc01610f.

(93) Luo, J.; Vermaas, D. A.; Bi, D.; Hagfeldt, A.; Smith, W. A.; Grätzel, M. Bipolar Membrane-Assisted Solar Water Splitting in Optimal PH. *Adv. Energy Mater.* **2016**, *6* (13), 1–7. https://doi.org/10.1002/aenm.201600100.

(94) Sun, K.; Liu, R.; Chen, Y.; Verlage, E.; Lewis, N. S.; Xiang, C. A Stabilized, Intrinsically Safe, 10% Efficient, Solar-Driven Water-Splitting Cell Incorporating Earth-Abundant Electrocatalysts with Steady-State PH Gradients and Product Separation Enabled by a Bipolar Membrane. *Adv. Energy Mater.* **2016**, *6*, 1600379. https://doi.org/10.1002/aenm.201670077.

(95) Chabi, S.; Wright, A. G.; Holdcroft, S.; Freund, M. S. Transparent Bipolar Membrane for Water Splitting Applications. *ACS Appl. Mater. Interfaces* **2017**, acsami.7b04402. https://doi.org/10.1021/acsami.7b04402.

(96) Vermaas, D. A.; Wiegman, S.; Nagaki, T.; Smith, W. A. Ion Transport Mechanisms in Bipolar Membranes for (Photo)Electrochemical Water Splitting. *Sustain. Energy Fuels* **2018**, *2* (9), 2006–2015. https://doi.org/10.1039/c8se00118a.

(97) Zhang, H.; Wang, H.; Jiao, K.; Xuan, J. PH-Differential Design and Operation of Electrochemical and Photoelectrochemical Systems with Bipolar Membrane. *Appl. Energy* **2020**, *268* (April), 115053. https://doi.org/10.1016/j.apenergy.2020.115053.

(98) Yan, Z.; Mallouk, T. E. Bipolar Membranes for Ion Management in (Photo)Electrochemical Energy Conversion. *Accounts Mater. Res.* **2021**, *2* (12), 1156–1166. https://doi.org/10.1021/accountsmr.1c00113.

(99) Giesbrecht, P. K.; Müller, A. M.; Read, C. G.; Holdcroft, S.; Lewis, N. S.; Freund, M. S. Vapor-Fed Electrolysis of Water Using Earth-Abundant Catalysts in Nafion or in Bipolar Nafion/Poly(Benzimidazolium) Membranes. *Sustain. Energy Fuels* **2019**, *3* (12), 3611–3626. https://doi.org/10.1039/c9se00672a.

(100) Mayerhöfer, B.; McLaughlin, D.; Böhm, T.; Hegelheimer, M.; Seeberger, D.; Thiele, S. Bipolar Membrane Electrode Assemblies for Water Electrolysis. *ACS Appl. Energy Mater.* **2020**, *3* (10), 9635–9644. https://doi.org/10.1021/acsaem.0c01127.

(101) Oener, S. Z.; Twight, L. P.; Lindquist, G. A.; Boettcher, S. W. Thin Cation-Exchange Layers Enable High-Current-Density Bipolar Membrane Electrolyzers via Improved Water Transport. *ACS Energy Lett.* **2021**, *6* (1), 1–8. https://doi.org/10.1021/acsenergylett.0c02078.

(102) Lee, L.; Kim, D. Poly(Arylene Ether Ketone)-Based Bipolar Membranes for Acid-Alkaline Water Electrolysis Applications. *J. Mater. Chem. A* **2021**, *9* (9), 5485–5496. https://doi.org/10.1039/d0ta09398j.

(103) Wendt, H.; Hofmann, H. Ceramic Diaphragms for Advanced Alkaline Water Electrolysis. *J. Appl. Electrochem.* **1989**, *19* (4), 605–610. https://doi.org/10.1007/BF01022121.

(104) Reier, T.; Nong, H. N.; Teschner, D.; Schlögl, R.; Strasser, P. Electrocatalytic Oxygen Evolution Reaction in Acidic Environments – Reaction Mechanisms and Catalysts. *Adv. Energy Mater.* **2017**, *7* (1). https://doi.org/10.1002/aenm.201601275.

(105) Bui, J. C.; Ibadillah, D.; Xiang, C.; Bell, A. T.; Weber, A. Z. Understanding Multi-Ion Transport Mechanisms in Bipolar Membranes. *ACS Appl. Mater. Interfaces* **2020**, *12* (47), 52509–52526. https://doi.org/10.1021/acsami.0c12686.

(106) Hohenadel, A.; Gangrade, A. S.; Holdcroft, S. Spectroelectrochemical Detection of Water Dissociation in Bipolar Membranes. *ACS Appl. Mater. Interfaces* **2021**, *13* (38), 46125–46133. https://doi.org/10.1021/acsami.1c12544.

(107) Brug, G. J.; van den Eeden, A. L. G.; Sluyters-Rehbach, M.; Sluyters, J. H. The

Analysis of Electrode Impedances Complicated by the Presence of a Constant Phase Element. *J. Electroanal. Chem.* **1984**, *176* (1–2), 275–295. https://doi.org/10.1016/S0022-0728(84)80324-1.

(108) Malkow, T.; Pilenga, A.; Tsotridis, G. *EU Harmonised Test Procedure: Electrochemical Impedance Spectroscopy for Water Electrolysis Cells*; Luxembourg, 2018. https://doi.org/10.2760/8984.

(109) Rozain, C.; Millet, P. Electrochimica Acta Electrochemical Characterization of Polymer Electrolyte Membrane Water Electrolysis Cells. *Electrochim. Acta* **2014**, *131*, 160–167. https://doi.org/10.1016/j.electacta.2014.01.099.

(110) Chilcott, T. C.; Coster, H. G. L.; George, E. P. AC Impedance of the Bipolar Membrane at Low and High Frequencies. *J. Memb. Sci.* **1995**, *100* (2), 77–86. https://doi.org/10.1016/0376-7388(94)00245-T.

(111) Alcaraz, A.; Ramírez, P.; Mafé, S.; Holdik, H. A Simple Model for Ac Impedance Spectra in Bipolar Membranes. *J. Phys. Chem.* **1996**, *100* (38), 15555–15561. https://doi.org/10.1021/jp961187c.

(112) Alcaraz, A.; Holdik, H.; Ruffing, T.; Ramírez, P.; Mafé, S. AC Impedance Spectra of Bipolar Membranes: An Experimental Study. *J. Memb. Sci.* **1998**, *150* (1), 43–56. https://doi.org/10.1016/S0376-7388(98)00201-4.

(113) Holdik, H.; Alcaraz, a; Ramírez, P.; Mafé, S. Electric Field Enhanced Water Dissociation at the Bipolar Membrane Junction from Ac Impedance Spectra Measurements. *J. Electroanal. Chem.* **1998**, *442* (1–2), 13–18. https://doi.org/10.1016/S0022-0728(97)00506-8.

(114) Yan, Z.; Zhu, L.; Li, Y. C.; Wycisk, R. J.; Pintauro, P. N.; Hickner, M. A.; Mallouk, T. E. The Balance of Electric Field and Interfacial Catalysis in Promoting Water Dissociation in Bipolar Membranes. *Energy Environ. Sci.* **2018**, 2235–2245. https://doi.org/10.1039/C8EE01192C.

(115) Blommaert, M. A.; Vermaas, D. A.; Izelaar, B.; in ’t Veen, B.; Smith, W. A. Electrochemical Impedance Spectroscopy as a Performance Indicator of Water Dissociation in Bipolar Membranes. **2019**, 1–20. https://doi.org/10.26434/chemrxiv.8068238.

(116) Luo, T.; Abdu, S.; Wessling, M. Selectivity of Ion Exchange Membranes: A Review. *J. Memb. Sci.* **2018**, *555* (March), 429–454. https://doi.org/10.1016/j.memsci.2018.03.051.

(117) Donnan, F. G. The Theory of Membrane Equilibria. *Chem. Rev.* **1924**, *1* (1), 73–90. https://doi.org/10.1021/cr60001a003.

(118) Giorno, L.; Drioli, E.; Strathmann, H. Permselectivity of Ion-Exchange Membranes. In *Encyclopedia of Membranes*; Springer: Berlin, Heidelberg, 2016.

(119) Jung, M. S.; Kim, T.-H.; Yoon, Y. J.; Kang, C. G.; Yu, D. M.; Lee, J. Y.; Kim, H.-J.; Hong, Y. T. Sulfonated Poly(Arylene Sulfone) Multiblock Copolymers for Proton Exchange Membrane Fuel Cells. *J. Memb. Sci.* **2014**, *459*, 72–85. https://doi.org/10.1016/j.memsci.2014.01.072.

(120) Mohanty, A. K.; Mistri, E. A.; Ghosh, A.; Banerjee, S. Synthesis and Characterization of Novel Fluorinated Poly(Arylene Ether Sulfone)s Containing Pendant Sulfonic Acid Groups for Proton Exchange Membrane Materials. *J. Memb. Sci.* **2012**, *409–410*, 145–155. https://doi.org/10.1016/j.memsci.2012.03.048.

(121) Wang, C.; Shin, D. W.; Lee, S. Y.; Kang, N. R.; Lee, Y. M.; Guiver, M. D. Poly(Arylene Ether Sulfone) Proton Exchange Membranes with Flexible Acid Side Chains. *J. Memb. Sci.* **2012**, *405–406*, 68–78. https://doi.org/10.1016/j.memsci.2012.02.045.

(122) Lee, H.-F. Preparation and Evaluation of Polymer Electrolytes for Fuel Cells, National Sun Yat-sen University, 2015.

(123) Lee, H. F.; Wang, P. H.; Huang, Y. C.; Su, W. H.; Gopal, R.; Lee, C. C.; Holdcroft, S.; Huang, W. Y. Synthesis and Proton Conductivity of Sulfonated, Multi-Phenylated Poly(Arylene Ether)S. *J. Polym. Sci. Part A Polym. Chem.* **2014**, *52* (18), 2579–2587. https://doi.org/10.1002/pola.27273.

(124) Lee, H. F.; Huang, Y. C.; Wang, P. H.; Lee, C. C.; Hung, Y. S.; Gopal, R.; Holdcroft, S.; Huang, W. Y. Synthesis of Highly Sulfonated Polyarylene Ethers Containing Alternating Aromatic Units. *Mater. Today Commun.* **2015**, *3*, 114–121. https://doi.org/10.1016/j.mtcomm.2015.01.006.

(125) Liu, C.; Carmo, M.; Bender, G.; Everwand, A.; Lickert, T.; Young, J. L.; Smolinka, T.; Stolten, D.; Lehnert, W. Performance Enhancement of PEM Electrolyzers through Iridium-Coated Titanium Porous Transport Layers. *Electrochem. commun.* **2018**, *97* (October), 96–99. https://doi.org/10.1016/j.elecom.2018.10.021.

(126) Pavel, C. C.; Cecconi, F.; Emiliani, C.; Santiccioli, S.; Scaffidi, A.; Catanorchi, S.; Comotti, M. Highly Efficient Platinum Group Metal Free Based Membrane-Electrode Assembly for Anion Exchange Membrane Water Electrolysis. *Angew. Chemie* **2014**, *126* (5), 1402–1405. https://doi.org/10.1002/ange.201308099.

(127) Dekel, D. R. Review of Cell Performance in Anion Exchange Membrane Fuel Cells. *J. Power Sources* **2018**, *375*, 158–169. https://doi.org/10.1016/j.jpowsour.2017.07.117.

(128) Hugar, K. M.; Kostalik, H. A.; Coates, G. W. Imidazolium Cations with Exceptional Alkaline Stability: A Systematic Study of Structure-Stability Relationships. *J. Am. Chem. Soc.* **2015**, *137* (27), 8730–8737. https://doi.org/10.1021/jacs.5b02879.

(129) Long, H.; Pivovar, B. Hydroxide Degradation Pathways for Imidazolium Cations: A DFT Study. *J. Phys. Chem. C* **2014**, *118* (19), 9880–9888. https://doi.org/10.1021/jp501362y.

(130) Strmcnik, D.; Li, D.; Lopes, P. P.; Tripkovic, D.; Kodama, K.; Stamenkovic, V. R.; Markovic, N. M. When Small Is Big: The Role of Impurities in Electrocatalysis. *Top. Catal.* **2015**, *58* (18–20), 1174–1180. https://doi.org/10.1007/s11244-015-0492-8.

(131) Su, H.; Bladergroen, B. J.; Linkov, V.; Pasupathi, S.; Ji, S. Study of Catalyst Sprayed Membrane under Irradiation Method to Prepare High Performance Membrane Electrode Assemblies for Solid Polymer Electrolyte Water Electrolysis. *Int. J. Hydrogen Energy* **2011**, *36* (23), 15081–15088. https://doi.org/10.1016/j.ijhydene.2011.08.057.

(132) Walker, S. B.; Mukherjee, U.; Fowler, M.; Elkamel, A. Benchmarking and Selection of Power-to-Gas Utilizing Electrolytic Hydrogen as an Energy Storage Alternative. *Int. J. Hydrogen Energy* **2016**, *41* (19), 7717–7731. https://doi.org/10.1016/j.ijhydene.2015.09.008.

(133) Holladay, J. D.; Hu, J.; King, D. L.; Wang, Y. An Overview of Hydrogen Production Technologies. *Catal. Today* **2009**, *139* (4), 244–260. https://doi.org/10.1016/j.cattod.2008.08.039.

(134) Ito, H.; Maeda, T.; Nakano, A.; Takenaka, H. Properties of Nafion Membranes under PEM Water Electrolysis Conditions. *Int. J. Hydrogen Energy* **2011**, *36*, 10527–10540. https://doi.org/10.1016/j.ijhydene.2011.05.127.

(135) Siracusano, S.; Baglio, V.; Stassi, A.; Merlo, L.; Moukheiber, E.; Arico', A. S. Performance Analysis of Short-Side-Chain Aquivion®perfluorosulfonic Acid Polymer for Proton Exchange Membrane Water Electrolysis. *J. Memb. Sci.* **2014**, *466*, 1–7. https://doi.org/10.1016/j.memsci.2014.04.030.

(136) Aricò, A. S.; Siracusano, S.; Briguglio, N.; Baglio, V.; Di Blasi, A.; Antonucci, V. Polymer Electrolyte Membrane Water Electrolysis: Status of Technologies and Potential Applications in Combination with Renewable Power Sources. *J. Appl. Electrochem.* **2013**, *43* (2), 107–118. https://doi.org/10.1007/s10800-012-0490-5.

(137) Kang, M. S.; Choi, Y. J.; Kim, S. H.; Moon, S. H. Enhancement of Water Splitting in Bipolar Membranes by Optimized Composite Anion-Exchange Layer and Alkali-Treated Polyacrylonitrile Catalytic Junction. *J. Memb. Sci.* **2004**, *229*

(1–2), 137–146. https://doi.org/10.1016/j.memsci.2003.10.021.

(138) Rajesh, A. M.; Chakrabarty, T.; Prakash, S.; Shahi, V. K. Effects of Metal Alkoxides on Electro-Assisted Water Dissociation across Bipolar Membranes. *Electrochim. Acta* **2012**, *66*, 325–331. https://doi.org/10.1016/j.electacta.2012.01.102.

(139) Adamski, M.; Skalski, T. J. G.; Britton, B.; Peckham, T. J.; Metzler, L.; Holdcroft, S. Highly Stable, Low Gas Crossover, Proton-Conducting Phenylated Polyphenylenes. *Angew. Chemie - Int. Ed.* **2017**, *56* (31), 9058–9061. https://doi.org/10.1002/anie.201703916.

(140) Wright, A. G.; Fan, J.; Britton, B.; Weissbach, T.; Lee, H.; Kitching, E. A.; Peckham, T. J.; Holdcroft, S. Hexamethyl-p-Terphenyl Poly(Benzimidazolium): A Universal Hydroxide-Conducting Polymer for Energy Conversion Devices. *Energy Environ. Sci.* **2016**, *9*, 2130–2142. https://doi.org/10.1039/C6EE00656F.

(141) Ballengee, J. B.; Pintauro, P. N. Composite Fuel Cell Membranes from Dual-Nanofiber Electrospun Mats. *Macromolecules* **2011**, *44* (18), 7307–7314. https://doi.org/10.1021/ma201684j.

(142) Balster, J.; Srinkantharajah, S.; Sumbharaju, R.; Pünt, I.; Lammertink, R. G. H.; Stamatialis, D. F.; Wessling, M. Tailoring the Interface Layer of the Bipolar Membrane. *J. Memb. Sci.* **2010**, *365*, 389–398. https://doi.org/10.1016/j.memsci.2010.09.034.

(143) Vermaas, D. A.; Smith, W. A. Synergistic Electrochemical CO2 Reduction and Water Oxidation with a Bipolar Membrane. *ACS Energy Lett.* **2016**, *1* (6), 1143–1148. https://doi.org/10.1021/acsenergylett.6b00557.

(144) Bauer, B.; Gerner, F. J.; Strathmann, H. Development of Bipolar Membranes. *Desalination* **1988**, *68*, 279–292. https://doi.org/10.1016/0011-9164(88)80061-4.

(145) Lu, H.; Wang, L.; Wycisk, R.; Pintauro, P. N.; Lin, S. Quantifying the Kinetics-Energetics Performance Tradeoff in Bipolar Membrane Electrodialysis. *J. Memb. Sci.* **2020**, *612*, 118279. https://doi.org/10.1016/j.memsci.2020.118279.

(146) Lei, Q.; Wang, B.; Wang, P.; Liu, S. Hydrogen Generation with Acid/Alkaline Amphoteric Water Electrolysis. *J. Energy Chem.* **2019**, *38*, 162–169. https://doi.org/10.1016/j.jechem.2018.12.022.

(147) Mayerhöfer, B.; McLaughlin, D.; Böhm, T.; Hegelheimer, M.; Seeberger, D.; Thiele, S. Bipolar Membrane Electrode Assemblies for Water Electrolysis. *ACS Appl. Energy Mater.* **2020**, *3*, 9635–9644. https://doi.org/10.1021/acsaem.0c01127.

(148) Yuzer, B.; Selcuk, H.; Chehade, G.; Demir, M. E.; Dincer, I. Evaluation of Hydrogen Production via Electrolysis with Ion Exchange Membranes. *Energy* **2020**, *190*, 116420. https://doi.org/10.1016/j.energy.2019.116420.

(149) Li, Y. C.; Zhou, D.; Yan, Z.; Gonçalves, R. H.; Salvatore, D. A.; Berlinguette, C. P.; Mallouk, T. E. Electrolysis of CO2 to Syngas in Bipolar Membrane-Based Electrochemical Cells. *ACS Energy Lett.* **2016**, *1* (6), 1149–1153. https://doi.org/10.1021/acsenergylett.6b00475.

(150) Salvatore, D. A.; Weekes, D. M.; He, J.; Dettelbach, K. E.; Li, Y. C.; Mallouk, T. E.; Berlinguette, C. P. Electrolysis of Gaseous CO2 to CO in a Flow Cell with a Bipolar Membrane. *ACS Energy Lett.* **2018**, *3* (1), 149–154. https://doi.org/10.1021/acsenergylett.7b01017.

(151) Mareev, S. A.; Evdochenko, E.; Wessling, M.; Kozaderova, O. A.; Niftaliev, S. I.; Pismenskaya, N. D.; Nikonenko, V. V. A Comprehensive Mathematical Model of Water Splitting in Bipolar Membranes: Impact of the Spatial Distribution of Fixed Charges and Catalyst at Bipolar Junction. *J. Memb. Sci.* **2020**, *603* (December 2019), 118010. https://doi.org/10.1016/j.memsci.2020.118010.

(152) Wrubel, J.; Chen, Y.; Ma, Z.; Deutsch, T. G. Modeling Water Electrolysis in Bipolar Membranes. *J. Electrochem. Soc.* **2020**, *167* (11), 114502. https://doi.org/10.1149/1945-7111/ab9ccb.

(153) Shel'deshov, N. V.; Krupenko, O. N.; Shadrina, M. V.; Zabolotskii, V. I. Electrochemical Parameters of Heterogeneous Bipolar Membranes: Dependence on the Structure and Nature of Monopolar Layers. *Russ. J. Electrochem.* **2002**, *38* (8), 884–887. https://doi.org/10.1023/A:1016817929491.

(154) Yan, Z.; Zhu, L.; Li, Y. C.; Wycisk, R. J.; Pintauro, P. N.; Hickner, M. A.; Mallouk, T. E. The Balance of Electric Field and Interfacial Catalysis in Promoting Water Dissociation in Bipolar Membranes. *Energy Environ. Sci.* **2018**, *11* (8), 2235–2245. https://doi.org/10.1039/c8ee01192c.

(155) Kang, M. S.; Choi, Y. J.; Lee, H. J.; Moon, S. H. Effects of Inorganic Substances on Water Splitting in Ion-Exchange Membranes: I. Electrochemical Characteristics of Ion-Exchange Membranes Coated with Iron Hydroxide/Oxide and Silica Sol. *J. Colloid Interface Sci.* **2004**, *273* (2), 523–532. https://doi.org/10.1016/j.jcis.2004.01.050.

(156) Mel'nikov, S. S.; Shapovalova, O. V.; Shel'deshov, N. V.; Zabolotskii, V. I. Effect of D-Metal Hydroxides on Water Dissociation in Bipolar Membranes. *Pet. Chem.* **2011**, *51* (7), 577–584. https://doi.org/10.1134/s0965544111070097.

(157) Zhang, B.; Gao, H.; Xiao, C.; Tong, X.; Chen, Y. The Trade-off between Membrane Permselectivity and Conductivity: A Percolation Simulation of Mass

Transport. *J. Memb. Sci.* **2020**, *597*, 117751. https://doi.org/10.1016/j.memsci.2019.117751.

(158) Fan, H.; Yip, N. Y. Elucidating Conductivity-Permselectivity Tradeoffs in Electrodialysis and Reverse Electrodialysis by Structure-Property Analysis of Ion-Exchange Membranes. *J. Memb. Sci.* **2019**, *573*, 668–681. https://doi.org/10.1016/j.memsci.2018.11.045.

(159) Guler, E.; Zhang, Y.; Saakes, M.; Nijmeijer, K. Tailor-Made Anion-Exchange Membranes for Salinity Gradient Power Generation Using Reverse Electrodialysis. *ChemSusChem* **2012**, *5* (11), 2262–2270. https://doi.org/10.1002/cssc.201200298.

(160) Jiang, J.; Tang, J.; Al-Anzi, B.; Han, J.; Li, Z. On the Validity of Ion Selective Membrane Simplification in Concentration Polarization. *AIP Adv.* **2021**, *11* (3), 1–10. https://doi.org/10.1063/5.0037961.

(161) Moussaoui, R. El; Pourcelly, G.; Maeck, M.; Hurwitz, H. D.; Gavach, C. Co-Ion Leakage through Bipolar Membranes Influence on I-V Responses and Water-Splitting Efficiency. *J. Memb. Sci.* **1994**, *90* (3), 283–292. https://doi.org/10.1016/0376-7388(94)80078-2.

(162) Yan, Z.; Hitt, J. L.; Zeng, Z.; Hickner, M. A.; Mallouk, T. E. Improving the Efficiency of CO2 Electrolysis by Using a Bipolar Membrane with a Weak-Acid Cation Exchange Layer. *Nat. Chem.* **2021**, *13* (1), 33–40. https://doi.org/10.1038/s41557-020-00602-0.

(163) Adhikari, S.; Pagels, M. K.; Jeon, J. Y.; Bae, C. Ionomers for Electrochemical Energy Conversion & Storage Technologies. *Polymer (Guildf).* **2020**, *211*, 123080. https://doi.org/10.1016/j.polymer.2020.123080.

(164) Zabolotskii, V.; Sheldeshov, N.; Melnikov, S. Effect of Cation-Exchange Layer Thickness on Electrochemical and Transport Characteristics of Bipolar Membranes. *J. Appl. Electrochem.* **2013**, *43* (11), 1117–1129. https://doi.org/10.1007/s10800-013-0560-3.

(165) Balster, J.; Sumbharaju, R.; Srikantharajah, S.; Pünt, I.; Stamatialis, D. F.; Jordan, V.; Wessling, M. Asymmetric Bipolar Membrane: A Tool to Improve Product Purity. *J. Memb. Sci.* **2007**, *287* (2), 246–256. https://doi.org/10.1016/j.memsci.2006.10.042.

(166) Geise, G. M.; Cassady, H. J.; Paul, D. R.; Logan, B. E.; Hickner, M. A. Specific Ion Effects on Membrane Potential and the Permselectivity of Ion Exchange Membranes. *Phys. Chem. Chem. Phys.* **2014**, *16* (39), 21673–21681. https://doi.org/10.1039/c4cp03076a.

(167) Ji, Y.; Geise, G. M. The Role of Experimental Factors in Membrane Permselectivity Measurements. *Ind. Eng. Chem. Res.* **2017**, *56* (26), 7559–7566. https://doi.org/10.1021/acs.iecr.7b01512.

(168) Kingsbury, R. S.; Flotron, S.; Zhu, S.; Call, D. F.; Coronell, O. Junction Potentials Bias Measurements of Ion Exchange Membrane Permselectivity. *Environ. Sci. Technol.* **2018**, *52* (8), 4929–4936. https://doi.org/10.1021/acs.est.7b05317.

(169) Guo, J.; Qiu, L.; Deng, Z.; Yan, F. Plastic Reusable PH Indicator Strips: Preparation via Anion-Exchange of Poly(Ionic Liquids) with Anionic Dyes. *Polym. Chem.* **2013**, *4* (5), 1309–1312. https://doi.org/10.1039/c2py21076b.

(170) Safavi, A.; Maleki, N.; Bagheri, M. Modification of Chemical Performance of Dopants in Xerogel Films with Entrapped Ionic Liquid. *J. Mater. Chem.* **2007**, *17* (17), 1674–1681. https://doi.org/10.1039/b613288j.

(171) Brightman, E.; Pasquier, D. Measurement and Adjustment of Proton Activity in Solid Polymer Electrolytes. *Electrochem. commun.* **2017**, *82*, 145–149. https://doi.org/10.1016/j.elecom.2017.08.005.

(172) Umeda, M.; Sayama, K.; Maruta, T.; Inoue, M. Proton Activity of Nafion 117 Membrane Measured from Potential Difference of Hydrogen Electrodes. *Ionics (Kiel).* **2013**, *19* (4), 623–627. https://doi.org/10.1007/s11581-012-0791-z.

(173) Blommaert, M. A.; Vermaas, D. A.; Izelaar, B.; In'T Veen, B.; Smith, W. A. Electrochemical Impedance Spectroscopy as a Performance Indicator of Water Dissociation in Bipolar Membranes. *J. Mater. Chem. A* **2019**, *7* (32), 19060–19069. https://doi.org/10.1039/c9ta04592a.

(174) Wang, T.; Cao, X.; Jiao, L. PEM Water Electrolysis for Hydrogen Production: Fundamentals, Advances, and Prospects. *Carbon Neutrality* **2022**, *1* (1), 1–19. https://doi.org/10.1007/s43979-022-00022-8.

(175) Park, J. E.; Kim, J.; Han, J.; Kim, K.; Park, S. Bin; Kim, S.; Park, H. S.; Cho, Y. H.; Lee, J. C.; Sung, Y. E. High-Performance Proton-Exchange Membrane Water Electrolysis Using a Sulfonated Poly(Arylene Ether Sulfone) Membrane and Ionomer. *J. Memb. Sci.* **2021**, *620* (October 2020), 118871. https://doi.org/10.1016/j.memsci.2020.118871.

(176) Aßmann, P.; Gago, A. S.; Gazdzicki, P.; Friedrich, K. A.; Wark, M. Toward Developing Accelerated Stress Tests for Proton Exchange Membrane Electrolyzers. *Curr. Opin. Electrochem.* **2020**, *21* (March), 225–233. https://doi.org/10.1016/j.coelec.2020.02.024.

(177) Weiß, A.; Siebel, A.; Bernt, M.; Shen, T.-H.; Tileli, V.; Gasteiger, H. A. Impact of Intermittent Operation on Lifetime and Performance of a PEM Water

Electrolyzer. *J. Electrochem. Soc.* **2019**, *166* (8), F487–F497. https://doi.org/10.1149/2.0421908jes.

(178) Zignani, S. C.; Faro, M. Lo; Trocino, S.; Aricò, A. S. Investigation of NiFe-Based Catalysts for Oxygen Evolution in Anion-Exchange Membrane Electrolysis. *Energies* **2020**, *13* (7). https://doi.org/10.3390/en13071720.

(179) Henkensmeier, D.; Najibah, M.; Harms, C.; Žitka, J.; Hnát, J.; Bouzek, K. Overview: State-of-the Art Commercial Membranes for Anion Exchange Membrane Water Electrolysis. *J. Electrochem. Energy Convers. Storage* **2021**, *18* (2). https://doi.org/10.1115/1.4047963.

(180) Hohenadel, A.; Powers, D.; Wycisk, R.; Adamski, M.; Pintauro, P.; Holdcroft, S. Electrochemical Characterization of Hydrocarbon Bipolar Membranes with Varying Junction Morphology. *ACS Appl. Energy Mater.* **2019**, *2* (9), 6817–6824. https://doi.org/10.1021/acsaem.9b01257.

(181) Chen, Y.; Martínez, R. J.; Gervasio, D.; Baygents, J. C.; Farrell, J. Water Splitting Promoted by Electronically Conducting Interlayer Material in Bipolar Membranes. *J. Appl. Electrochem.* **2020**, *50* (1), 33–40. https://doi.org/10.1007/s10800-019-01365-4.